Doctor Thesis

Microscopic Study of Organic Superconductors near Antiferromagnetic Insulating Phase by ^{13}C NMR Spectroscopy

(^{13}C NMR法による反強磁性絶縁相に隣接した有機超伝導体の微視的な研究)

Takuya Kobayashi

Low Temperature Physics Group,
Department of Condensed Matter Physics,
Graduate School of Science, Hokkaido University

March 2018

Contents

Chapter 1

General introduction

1.1 Organic superconductors

In the conventional BCS superconductors such as mercury and niobium-titanium alloys, the pairing of superconducting electrons is mediated by phonons [1]. On the other hand, in cuprates, iron-base superconductors, and organic superconductors, the electronic correlation plays a crucial role in the emerging of the superconductivity [2]. For example, electronic state changes from antiferromagnetic to superconducting state by changing the oxygen concentration in $YBa_2Cu_3O_{6+x}$. The spin fluctuation originated from antiferromagnetism is the possible origin of superconductivity.

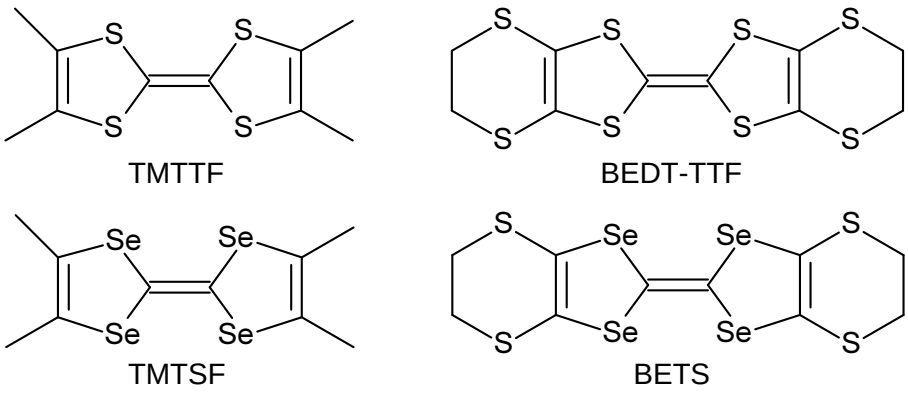

Figure 1.1: Molecules used for developing the organic superconductors.

To examine the relation between electronic correlation and superconductivity, organic superconductors are one of the most suitable field, because the physical properties can be easily controlled by the physical pressure or chemical pressure. The superconductivity in organic materials was first reported in $(TMTSF)_2PF_6$ [TMTSF denotes tetramethyltetraselenafulvalene (Fig. 1.1)] under

pressure [3]. By further investigation, it has been revealed that the system of (TMTCF)$_2X$ (C = S and Se, X = Br, AsF_6, PF_6, ClO_4 and so on) shows a wide variety of electronic states such as spin Peierls, charge order, antiferromagnetic, spin-density-wave and superconducting states and can be considered by the pressure-temperature phase diagram [4]. The superconducting transition temperature T_c is approximately 1 K. These findings facilitate the exploring of superconductors in organic systems. Among them, T_c was enhanced up to $\sim$ 10 K using BEDT-TTF [BEDT-TTF: bis(ethylenedithio)tetrathiafulvalene (Fig. 1.1)] molecules [5, 6, 7, 8]. Until now, more than 50 kinds of superconductors based on BEDT-TTF molecules were developed [9], in which conducting BEDT-TTF layers and insulating anion layers are alternately stacked and quasi-two-dimensional structure is formed. An interesting feature of BEDT-TTF salts is that there are various arrangements in BEDT-TTF layers. The packing arrangement of BEDT-TTF molecules are labeled by Greek letters such as α, β, κ, λ and so on as shown in Fig. 1.2. Since each arrangement provides the different electronic system, mechanism of superconductivity can be studied from a variety of perspectives.

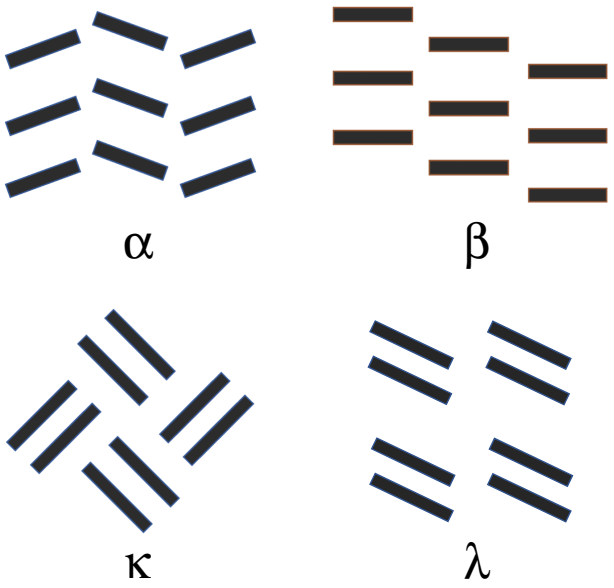

Figure 1.2: Packing arrangement of BEDT-TTF molecules in conducting layers.

1.2 Scope of the thesis

In this study, we focused on the κ-type salts which have the highest T_c among the organic superconductors at ambient pressure. The electronic properties of this system can be tuned from antiferromagnetic Mott insulating to superconducting state by applying pressure and substituting

the anion. Particularly, we targeted κ-(BEDT-TTF)$_2$Cu[N(CN)$_2$]Br salt, the superconducting state of which is adjacent to the antiferromagnetic phase, and investigated the unconventional superconducting properties in terms of superconducting fluctuation and impurity effect using ^{13}C NMR spectroscopy.

Next target material is λ-(BETS)$_2$GaCl$_4$ [BETS: bis(ethylenedithio)tetraselenafulvalene (Fig. 1.1)] salt. Noteworthy, superconducting phase of this salt is next to the antiferromagnetic insulating and nonmagnetic insulating phases by molecular replacement. The effect of their insulating phases on λ-(BETS)$_2$GaCl$_4$ salt is interesting but the electronic properties have been poorly investigated due to the small size of the samples and the lack of appropriate probe. In this study, we synthesized the ^{13}C enriched BETS molecules and performed the ^{13}C NMR measurement to study the electronic properties of λ-(BETS)$_2$GaCl$_4$ salt.

Chapter 2

Nuclear Magnetic resonance (NMR)

Nuclear magnetic resonance (NMR) spectroscopy microscopically probes the electronic states around nuclei through the hyperfine field between nuclei and electrons. Since NMR shift detects the local spin susceptibility and spin-lattice relaxation time T_1 measurement detects the magnetic fluctuation, NMR spectroscopy is a powerful tool to study the electronic state of strongly correlated electron systems.

2.1 NMR shift

From the NMR shift measurements, static susceptibility can be examined. In general, NMR shift δ is written as the sum of Knight shift K and chemical shift σ, that is,

$$\delta = K + \sigma. \tag{2.1}$$

Knight shift represents the contribution from the electronic spins, and chemical shift represents the contribution from the orbital current of electrons. Knight shift is written by the product of hyperfine coupling constant A and bulk susceptibility χ,

$$K = A\chi. \tag{2.2}$$

A and σ is changed by the orientation of the external magnetic field because of their anisotropy. Therefore, temperature dependence of spin susceptibility can be measured by fixing the direction of magnetic field.

2.2 Spin-lattice relaxation time T_1

The exchange of energy between a nuclear spin system under magnetic field, and the heat reservoir consisting of the other degrees of freedom (the lattice), brings the magnetization into a

condition of thermal equilibrium. The time required to relax nuclear spins into thermal equilibrium state is called nuclear spin-lattice relaxation time T_1.

When the magnetic relaxation is mainly from the electrons, by fluctuation-dissipation theorem, $1/T_1T$ can be described in terms of dynamic susceptibility $\chi''(\boldsymbol{q},\omega)$ as

$$\frac{1}{T_1T} = \frac{2\gamma_n^2 k_B}{(\gamma_e\hbar)^2}\sum_q A_q A_{-q}\frac{\chi''(\boldsymbol{q},\omega)}{\omega}, \tag{2.3}$$

where k_B is the Boltzmann constant, $\hbar$ is the Planck constant, γ_n and γ_e are the nuclear and electronic gyromagnetic moments, respectively, and ω is Larmor frequency [10]. The T_1 reflects the dynamic susceptibility, and the dynamic susceptibility involves the effects of the electron correlation. This equation is applied regardless of metal or nonmetal. Therefore, dynamic susceptibility can be examined by T_1 measurement.

Fermi liquid state

When a system is in a Fermi liquid state, $1/T_1T$ is proportional to the square of the density of states at the Fermi energy $N(E_F)$,

$$\frac{1}{T_1T} = \frac{\pi k_B}{\hbar}A_{\rm hf}^2 N^2(E_F). \tag{2.4}$$

Therefore, $1/T_1T$ is not depend on the temperature. Typical example of $1/T_1$ measurement in the Fermi liquid state are shown in Fig. 2.1. This figure shows the temperature dependence of $1/T_1T$ in organic superconductor κ-(BEDT-TTF)$_2$Cu(NCS)$_2$ salt (T_c = 10.4 K [5]) under several pressures. Because the magnetic field of 9.4 T was applied perpendicular to the conduction plane, superconductivity is completely suppressed and $1/T_1T$ shows constant from $\sim$ 20 K down to the lowest temperature at ambient pressure, which suggests the Fermi liquid state. Applying pressure stabilize the Fermi liquid state and constant $1/T_1T$ was observed from higher temperatures.

Magnetic fluctuation

Temperature-dependent $1/T_1T$ is induced by the magnetic fluctuation which is enhanced near the magnetic transition. For example, when a system has a two-dimensional antiferromagnetic fluctuation in the vicinity of antiferromagnetic phase transition, $1/T_1T$ can be written as,

$$\frac{1}{T_1T} = \frac{C}{T+\Theta}, \tag{2.5}$$

where C and Θ are the Curie constant and Weiss temperature. Figure 2.2 shows an example of antiferromagnetic transition in κ-(BEDT-TTF)$_2$Cu[N(CN)$_2$]Cl salt which is a dimer Mott insulator and shows a antiferromagnetic transition at 27 K. Temperature dependence of $1/T_1T$ shows the Curie-like behavior above 27 K.

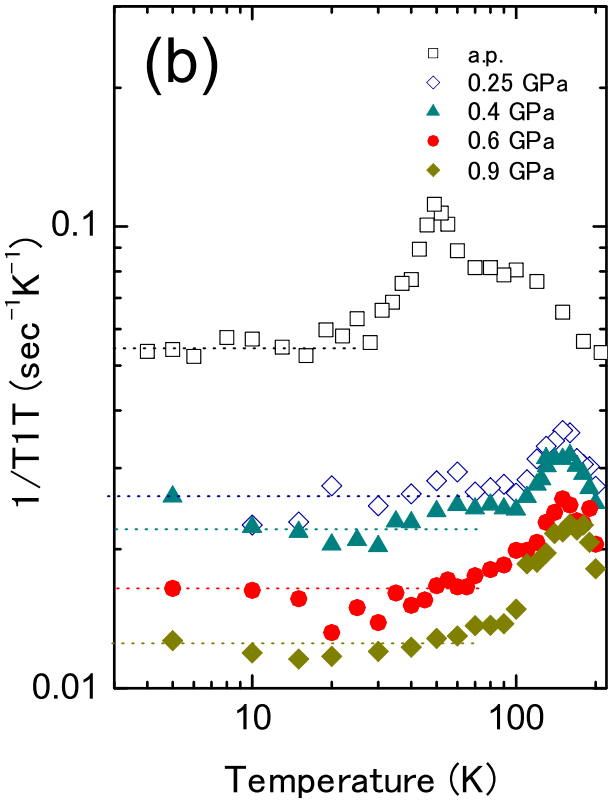

Figure 2.1: Temperature dependence of $1/T_1T$ of κ-NCS under several pressures [11].

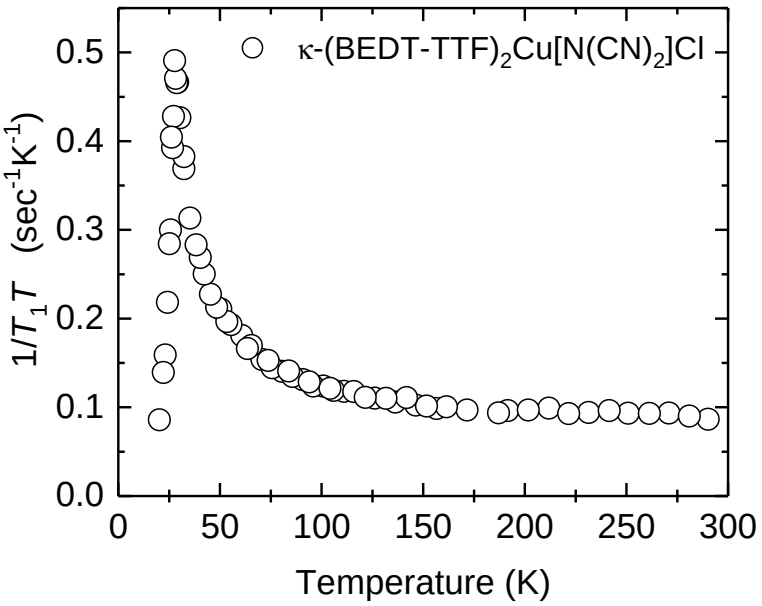

Figure 2.2: Temperature dependence of $1/T_1T$ of κ-(BEDT-TTF)$_2$Cu[N(CN)$_2$]Cl [12].

2.3 NMR study on superconductivity

2.3.1 Knight shift

NMR spectroscopy is informative probe to investigate the symmetry of superconducting gap. In the superconducting state, although the bulk magnetization measurement observes the diamagnetic signal from Meissner effect, Knight shift directly observe the spin susceptibility. Therefore, the pairing state of the Cooper pair, whether spin-singlet or triplet pairing state, can be investigated. In the spin-singlet superconducting state, spin susceptibility tends to zero as $T \to 0$. On the other hand, spin susceptibility does not change in the triplet superconducting state. Consequently, Knight shift decreases below T_c in singlet state but is independent of temperature in triplet state.

Figure 2.3 shows the temperature dependence of the Knight shift of organic superconductor κ-Br salt under a magnetic field of 7.8 T parallel (open circles) and perpendicular (closed circles) to the conduction plane [13]. The measurement in parallel field, in which H_{c2} is higher than 30 T [14], shows decrease in the Knight shift below T_c, while in perpendicular field ($H_{c2} \sim 10$ T), superconductivity is suppressed above 4 K. This result indicates the spin part of the wave function is in a singlet state.

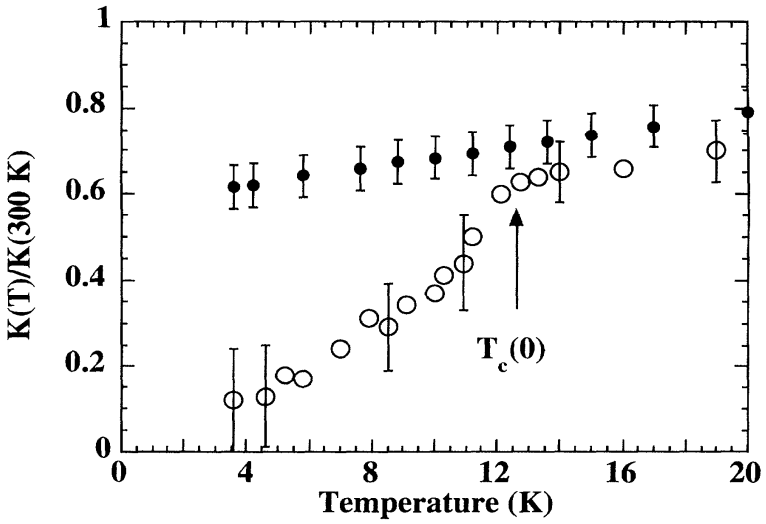

Figure 2.3: Temperature dependence of Knight shift of κ-Br [13].

2.3.2 $1/T_1$

The orbital part of Cooper pair wavefunction is restricted to satisfy the Pauli exclusion principle. Namely, the angular momentum $L = 0, 2$ (s-wave, d-wave) in the spin-singlet state and $L = 1$

(p-wave) in the spin-triplet state. In the spin-singlet state, T_1 measurements explicitly distinguish the s-wave superconducting gap from others.

In the superconducting state, $1/T_1$ arises from the scattering of the thermally excited quasiparticles. Then, $1/T_1$ is written as [15],

$$\frac{1}{T_1} = \frac{\pi A^2}{\hbar} \int_0^\infty \left\{ N_s^2(E) + M_s^2(E) \right\} f(E)(1 - f(E))dE, \tag{2.6}$$

where E is the energy of the quasiparticles, $f(E)$ is the Fermi distribution function. $N_s(E)$ is the density of states of the quasiparticles and $M_s(E)$ is the anomalous density of states, which is related to the coherence effect. In the isotropic s-wave superconductor, $N_s(E)$ and $M_s(E)$ are expressed as

$$N_s(E) = \frac{N_0 E}{\sqrt{E^2 - \Delta^2}} \tag{2.7}$$

$$M_s(E) = \frac{N_0 \Delta}{\sqrt{E^2 - \Delta^2}}, \tag{2.8}$$

where N_0 is the density of states at the normal state and Δ is the superconducting gap. $N_s(E)$ and $M_s(E)$ have strong divergence at the gap edge (Fig. 2.4) which leads to an increase in $1/T_1$ just below T_c. At low temperatures $1/T_1$ decreases exponentially because of $f(E)$. Figure 2.5

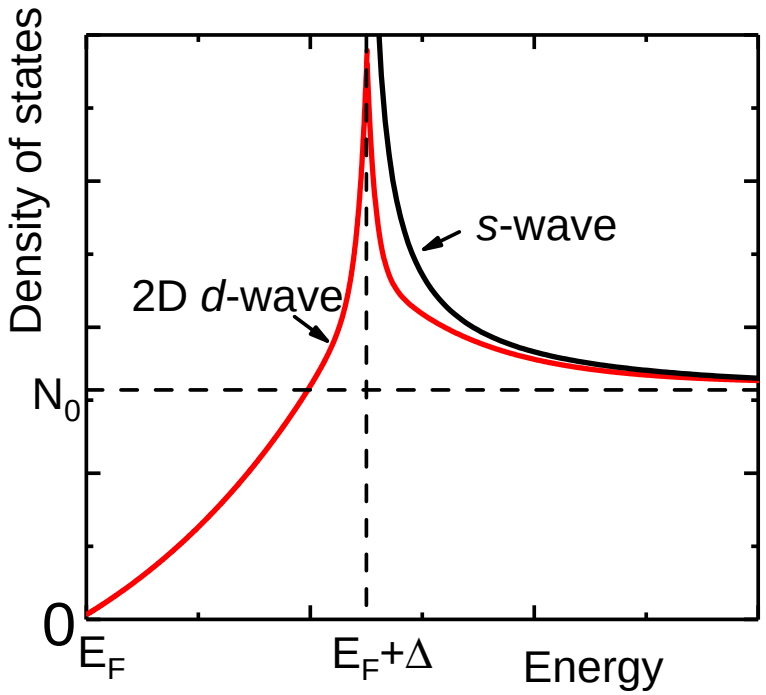

Figure 2.4: Density of states of isotropic s-wave superconductivity and two-dimensional d-wave superconductivity.

shows the temperature dependence of T_1 in aluminum, in which the horizontal axis is normalized

by $T_c = 1.178$ K [16]. Below T_c, T_1 sharply decreases (coherence peak) and then shows thermally activated behavior down to the lowest temperature, which is the typical behavior of isotropic s-wave superconductor.

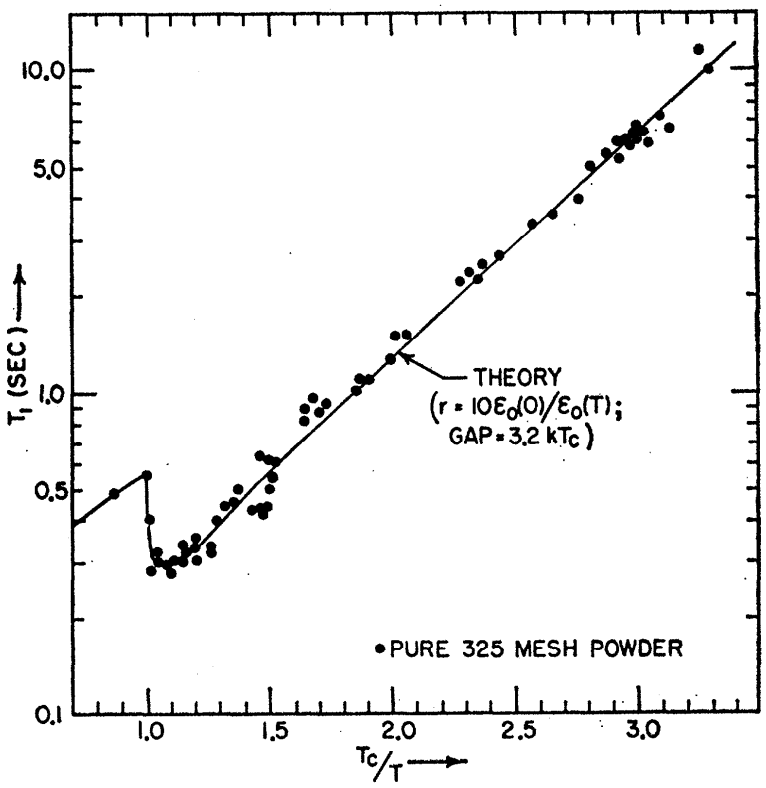

Figure 2.5: Temperature dependence of T_1 in the powdered sample of aluminum [16].

In the two-dimensional d-wave superconductor, order parameter is written as $\Delta \cos 2\phi$. Therefore, $N_s(E)$ and $M_s(E)$ are as follows,

$$N_s(E) = \int_0^{2\pi} \int_0^{\pi} \frac{E}{\sqrt{E^2 - \Delta^2 \cos^2 2\phi}} \sin\theta d\theta d\phi \tag{2.9}$$

$$M_s(E) = \int_0^{2\pi} \int_0^{\pi} \frac{\Delta \cos 2\phi}{\sqrt{E^2 - \Delta^2 \cos^2 2\phi}} \sin\theta d\theta d\phi. \tag{2.10}$$

When the superconducting gap has nodes, the divergence at the gap edge is weaken as shown in Fig. 2.4. In this case, $M_s(E) = 0$ when averaged over the Fermi surface. Thus, due to the absence of $M_s(E)$ and the weak divergence of $N_s(E)$ at the gap edge, the coherence peak just below T_c is either small or absent for d-wave symmetry. $N_s(E)$ in the low energy is proportional to E when $E \to 0$. Therefore, $1/T_1$ at low temperatures can be written as

$$\frac{1}{T_1} \propto \int_0^{\infty} E^2 \mathrm{e}^{-E/k_B T} dE = T^3 \int_0^{\infty} x^2 \mathrm{e}^{-x} dx. \tag{2.11}$$

Then $1/T_1$ is proportional to T^3. Figure 2.6 shows the temperature dependence of $1/T_1$ of κ-Br salt in the superconducting state [13]. The coherence peak was not observed and $1/T_1$ follows a cubic temperature dependence below T_c. This behavior indicates that the line node exists in the superconducting gap. From the results of Knight shift and $1/T_1$, NMR experiment suggests the superconducting order parameter of κ-Br salt has the symmetry of d-wave.

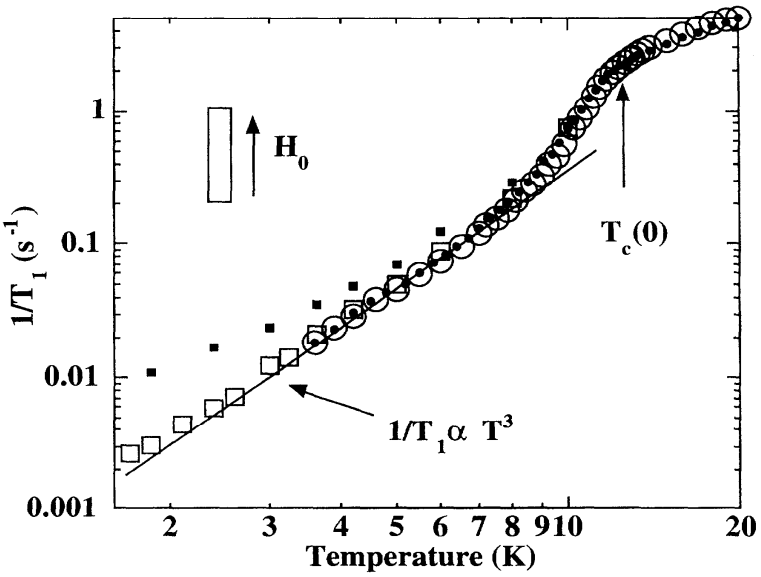

Figure 2.6: Temperature dependence of $1/T_1$ of κ-Br under the magnetic field parallel to the conduction plane [13].

Part I

Studies of Superconductivity in κ-(BEDT-TTF)$_2X$ by ^{13}C NMR

Chapter 3

Introduction

3.1 Structure of κ-(BEDT-TTF)$_2X$

3.1.1 Crystal structure

Organic conductors κ-(BEDT-TTF)$_2X$ have quasi-two-dimensional structure, and the repeat unit contains the layer of the conducting BEDT-TTF molecules and the layer of insulating anions X [Fig. 3.1(a)]. The packing arrangement of BEDT-TTF molecules are labeled by Greek letters. κ-type salts have face-to-face molecular dimers, which are oriented approximately at the angle of 90 degrees with respect to their neighbors [Fig. 3.1(b)]. In these salts, various anions X can enter into the insulating layer and modify the distance between BEDT-TTF dimers. Particularly, X = Cu[N(CN)]$_2$Cl, Cu[N(CN)]$_2$Br and Cu(NCS)$_2$ (hereafter referred to as the κ-Cl, κ-Br and κ-NCS, respectively) salts are extensively investigated. Lattice parameters of these salts are listed in Table 3.1.

Table 3.1: The lattice parameters of κ-(BEDT-TTF)$_2X$.

X	Cu(NCS)$_2$	Cu[N(CN)$_2$]Br	Cu[N(CN)$_2$]Cl
space group	$P2_1$	Pnma	Pnma
a(Å)	16.248(5)	12.942(3)	12.977(3)
b(Å)	8.440(2)	30.016(4)	29.979(4)
c(Å)	13.124(5)	8.539(3)	8.480(2)
β(°)	110.30(3)		
V(Å^3)	1688.0(9)	3317(7)	3299(1)
Ref.	[5]	[6]	[7]

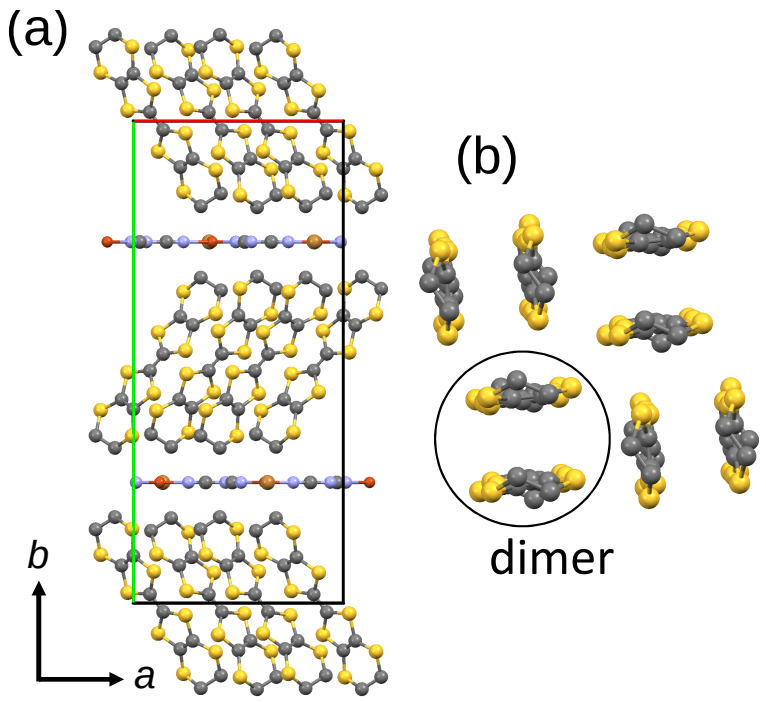

Figure 3.1: (a) Crystal structure of κ-(BEDT-TTF)$_2X$. (b) Packing arrangement of κ-type salt.

3.1.2 Band structure

BEDT-TTF salts are charge transfer salts, where one BEDT-TTF molecule provides 0.5 electron to anion X. κ-(BEDT-TTF)$_2X$ salts are understood as half-filled system because of the dimerization. One electron moves from the two molecules to the monovalent anions X. The dimerization creates the hybrid orbitals that are bonding orbital and anti-bonding orbital as shown in Fig. 3.2. Here, the t_{dimer} is the transfer integral within the dimer. As three electrons occupy this dimer, one hole is created and contributes conductivity. Figure 3.3 shows (a) the band structure calculated by the tight-binding method and (b) the Fermi surface of the half-filled band [17]. As two dimers are in the unit cell, four bands in Fig. 3.3 accommodate a total of eight electrons. These band structures of κ-(BEDT-TTF)$_2X$ salts predict a metallic state but in real materials, physical properties other than metallic behavior is observed. Next we introduce the physical properties of κ-(BEDT-TTF)$_2X$ salts.

3.2 Physical properties of κ-(BEDT-TTF)$_2X$

Figure 3.4 shows the temperature dependence of resistivity obtained for various κ-(BEDT-TTF)$_2X$ salts in various pressures [18]. κ-Cl salt shows semiconducting behavior over the whole temperature range at ambient pressure, but application of mechanical pressure induces the resis-

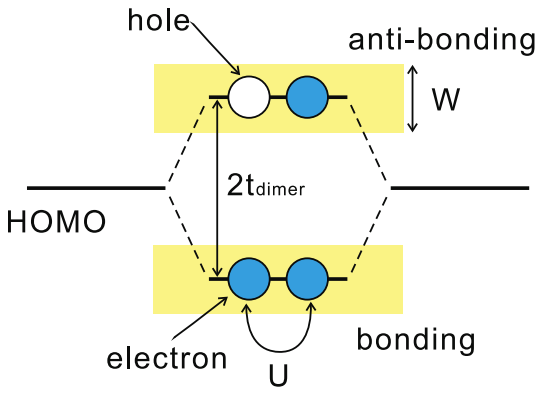

Figure 3.2: Schematic image of orbital hybridization.

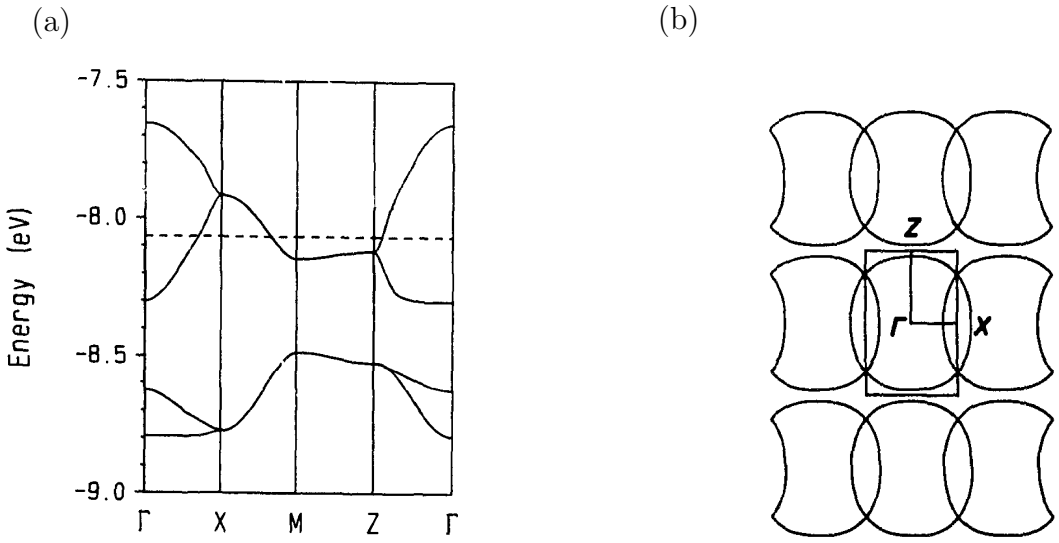

Figure 3.3: (a) Band structure and (b) Fermi surface.

tance maximum around 100 K and metallic phase at low temperature. Then, κ-Cl salt shows superconducting transition at 12.5 K under a pressure of 0.3 kbar [6]. These properties can be understood in the pressure-temperature (P-T) phase diagram (Fig. 3.5) [19, 20, 21]. In κ-Br and κ-NCS salts, the same temperature dependence of resistivity as κ-Cl salt under pressures was observed at ambient pressure. Therefore, these salts can be mapped on the P-T phase diagram of κ-Cl salt. These results indicate that applying the physical/chemical pressure can change the lattice parameter and increase in conduction bandwidth W with respect to the on-site Coulomb energy U. Finally, Fig. 3.5 explains the variety of physical properties both by physical and chemical pressures. Here, chemical pressure corresponds to the anion substitution.

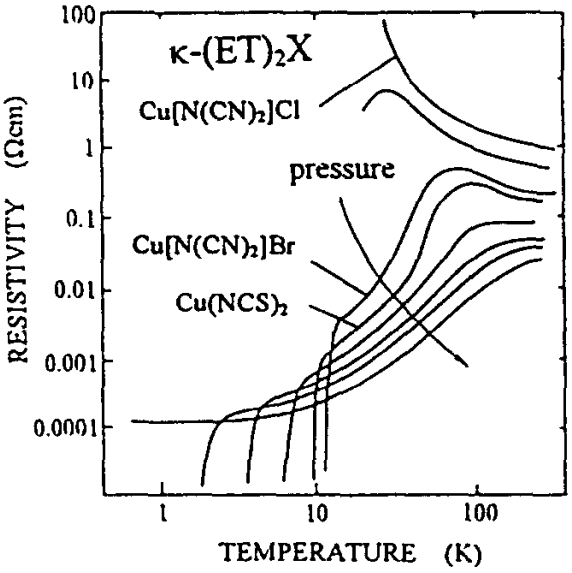

Figure 3.4: Temperature dependence of electrical resistivity for κ-(BEDT-TTF)$_2X$ [18].

The main feature of the P-T phase diagram is that superconducting phase is adjacent to antiferromagnetic phase. Connection between antiferromagnetism and superconductivity has been expected, and κ-(BEDT-TTF)$_2X$ salts have been investigated extensively as candidates for a strongly correlated electron system.

3.3 Magnetic properties of κ-(BEDT-TTF)$_2X$

Temperature dependence of the magnetic susceptibility of κ-(BEDT-TTF)$_2X$ salts is shown in Fig 3.6. Temperature dependence and absolute values of susceptibility are almost same in all three salts above 50 K. Below 30 K, susceptibility of κ-Cl salt shows rapid increase because of spin canting in the antiferromagnetism. In κ-Br and κ-NCS salts, the slope of susceptibility is

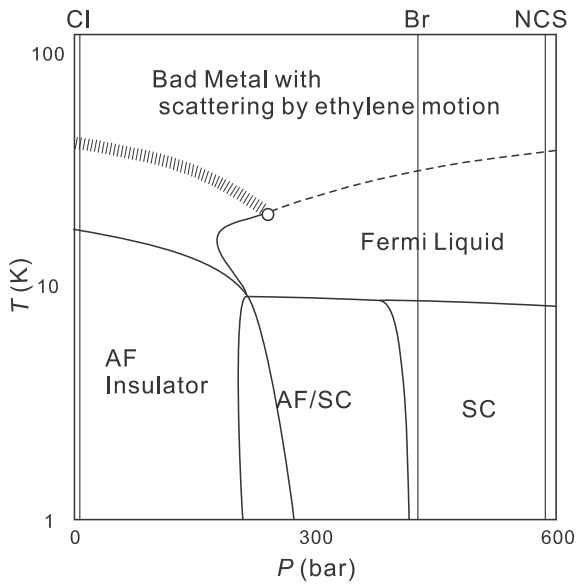

Figure 3.5: Pressure–temperature phase diagram of κ-(BEDT-TTF)$_2X$ [22]. Horizontal axis corresponds to the physical/chemical pressure.

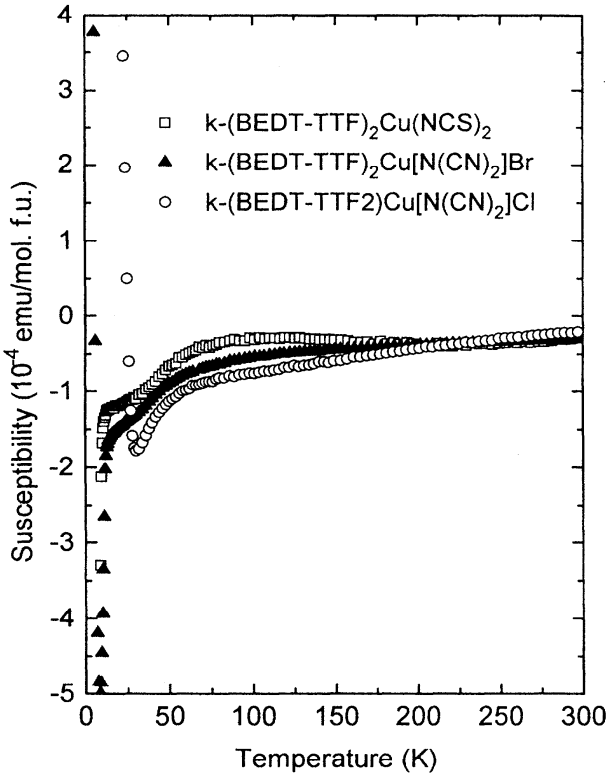

Figure 3.6: Temperature dependence of magnetic susceptibility of κ-(BEDT-TTF)$_2X$ [12].

small at 35 K compared with that of κ-Cl salt. This anomaly was interpreted as due to the suppression of the antiferromagnetic fluctuation [23] and clearly observed in the T_1 measurement. Figure 3.7 shows the temperature dependence of $1/T_1T$ of κ-(BEDT-TTF)$_2X$ salts. In κ-Cl salt, $1/T_1T$ increases from room temperature toward antiferromagnetic transition temperature $T_N =$ 27 K. The behavior of $1/T_1T$ can be understood by two contributions. One is the temperature-dependent antiferromagnetic (AF) term, which originates from the enhanced susceptibility with the wave vector close to the ordering vector Q, and the other is that the $\chi''(q)$ from the long wavelength gives rise to the constant contribution. Namely,

$$\frac{1}{T_1T} = \frac{2\gamma_n^2 k_B A_{\rm hf}^2}{\gamma_e^2 \hbar^2} \left(\sum_{q \simeq Q} \frac{\chi''(q)}{\omega} + \sum_{q \neq Q} \frac{\chi''(q)}{\omega} \right) \tag{3.1}$$

$$= \left(\frac{1}{T_1T} \right)_{\rm AF} + \left(\frac{1}{T_1T} \right)_{\rm FL}. \tag{3.2}$$

Temperature dependence of $1/T_1T$ of κ-Br and κ-NCS salts deviates from that of κ-Cl salt at $T^* = 45$ K and 50 K, respectively. This behavior indicates the suppression of $(1/T_1T)_{\rm AF}$ term below T^*. T^* of κ-Br salt is lower than that of κ-NCS salt. This difference indicates that the antiferromagnetic correlation of κ-Br salt is stronger than that of κ-NCS salt.

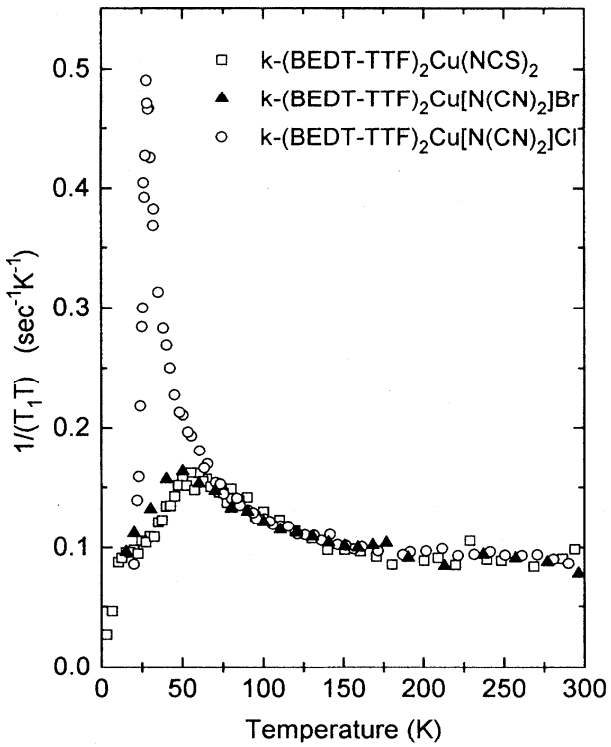

Figure 3.7: Temperature dependence of $1/T_1T$ of κ-(BEDT-TTF)$_2X$ [12].

3.4 Superconductivity of κ-(BEDT-TTF)$_2X$

3.4.1 Anisotropic superconductivity

Superconducting properties of κ-(BEDT-TTF)$_2X$ salts are highly anisotropic due to two-dimensional crystal and electronic structure. For example, while upper critical field H_{c2} of κ-Br salt under magnetic fields perpendicular to the plane is 10 T [14, 13, 24], that under magnetic fields parallel to the plane is higher than 30 T [14]. The coherence length ξ estimated from H_{c2} is also highly anisotropic. The superconducting parameters are listed in Table 3.2. From the strong anisotropy, anomalous properties of superconductivity is expected. One of the interesting features is the superconducting fluctuation phenomena. Details will be introduced in 3.4.3.

Table 3.2: The superconducting parameter of κ-(BEDT-TTF)$_2X$.

	Cu(NCS)$_2$	Cu[N(CN)$_2$]Br	Ref.
T_c (K)	10.4	11.6	[5, 7]
$H_{c2}^{\parallel}$ (T)	30-35	30	[14]
$H_{c2}^{\perp}$ (T)	8	10	[14, 13, 24]
$\xi^{\parallel}$ (Å)	70	37	[25]
$\xi^{\perp}$ (Å)	5	6	[25]
$2\Delta/k_BT_c$	3.6	5	[25]

3.4.2 Impurity effect on superconductivity

Superconducting gap symmetry

Anisotropy of superconducting gap in conduction plane has been suggested from various experiments, such as NMR [13], STS [26], and thermal conductivity [27] and so on. However, some of the experiments (for instance, μSR [25], specific heat [28]) concluded the isotropic superconducting gap. To study the superconducting symmetry in the conduction plane, impurity effect on superconducting gap is a powerful technique. In this study, we focus on the study of impurity effect by NMR measurement, which has not been investigated in the organic conductor.

Impurity effect

Superconducting pair breaking effect by impurities has been intensively studied to reveal the superconducting properties of the pure material in cuprates and heavy-fermion system [29]. Namely,

magnetic and nonmagnetic impurity doping to unknown superconductor helps to determine the symmetry of superconducting gap function, because the scattering by magnetic impurities suppresses superconductivity with isotropic superconducting gap more efficiently than that with anisotropic superconducting gap, and vice versa, nonmagnetic impurities suppress drastically the anisotropic superconductivity. The suppression of T_c has been investigated in detail for various superconductors. Fig. 3.8 shows the T_c versus magnetic/nonmagnetic impurity doping concentration of MgB_2 and high-T_c cuprates [30, 31]. In a isotropic superconductor MgB_2, T_c was suppressed to 80 % of pure sample even by doping 10 % of nonmagnetic impurities. While in anisotropic superconductor, 10 % of nonmagnetic Zn suppresses T_c to 0 K.

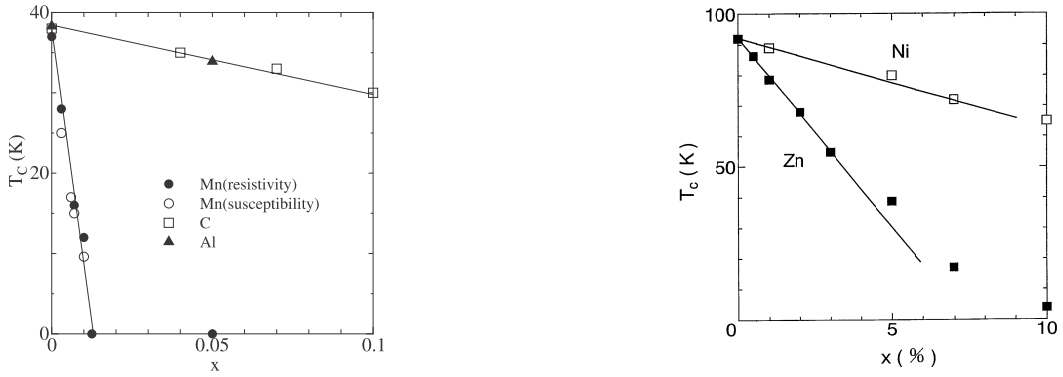

Figure 3.8: The relation of T_c and the impurity doping ratio x. Left: $Mg_{1-x}M_xB_2$ (M = Mn, Al) and $Mg(B_{1-x}C_x)2$ [30]. Right: $YBa_2(Cu_{1-x}M_x)_3O_7$ (M = Zn, Ni). [31]

The suppression of T_c by disorder was investigated in κ-NCS salt. To introduce disorders, substitution of BMDT-TTF [bis(methylenedithio)tetrathiafulvalene, Fig 3.9(a)] molecule for the BEDT-TTF molecule and X-ray irradiation to create structural defects were performed [32, 33]. However, these methods have some drawback from the aspect of NMR experiment. X-ray irradiation predominately causes damages on the surface of crystals due to the absorption and also produces free radicals on the surface. Because NMR measurement detects the signal from the entire sample, we would mainly observe the undamaged inner part of the sample. BMDT-TTF molecules can be introduced uniformly. However, because of the difference in the molecular structure between BMDT-TTF and BEDT-TTF, crystal structure would be distorted in addition to the distortion of the electronic state. It complicates the study of impurity effect. Furthermore, constituent element of BMDT-TTF molecule is the same as that of BEDT-TTF molecule, so the substitution ratio is difficult to be estimated. Naito *et al.* reported that the T_c of κ-Br salt can be controlled by BEDT-STF [bis(ethylenedithio)dithiadiserenafulvalene, Fig. 3.9 (b)] molecule substitution [34]. In this molecule, only two sulfur atoms close to the central C=C bond of BEDT-TTF molecule were replaced with selenium. Because molecular structure of BEDT-STF molecule is the

same as that of BEDT-TTF molecule, structural distortion is small and only potential scattering can cause the impurity effect.

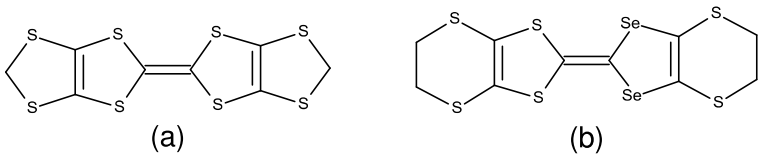

Figure 3.9: (a) BMDT-TTF molecule. (b) BEDT-STF molecule

In fact, lattice parameters of BEDT-STF 20 % doped κ-Br (a=12.934, b=30.070, c=8.536 $\AA$) is almost the same as that of pristine κ-Br (Table 3.1)[34]. Figure 3.10 shows the temperature dependence of resistivity of κ-[(BEDT-TTF)$_{1-x}$(BEST-STF)$_x$]$_2$Cu[N(CN)$_2$]Br. From the resistivity and X-ray diffraction measurements, the relation of T_c and doping concentration ratio was determined (Fig 3.11). Suppression of T_c can be explained either as the impurity effect or as the chemical pressure effect, because resistivity maximum is suppressed by BEDT-STF doping. To reveal the effect of BEDT-STF doping to electronic state, NMR study is required.

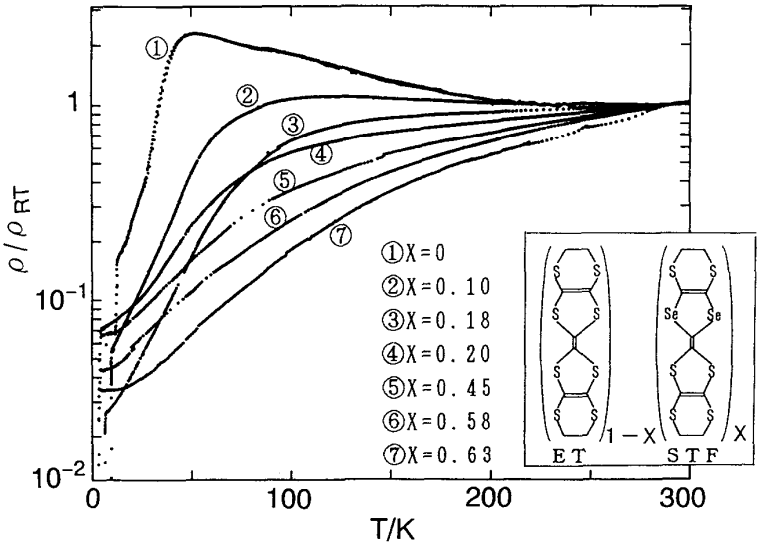

Figure 3.10: Temperature dependence of resistivity of κ-[(BEDT-TTF)$_{1-x}$(BEST-STF)$_x$]$_2$Cu[N(CN)$_2$]Br [35].

Doping effect can be investigated by T_1 measurements. In κ-Br and κ-NCS salts, the peak behavior of $1/T_1T$ at T^* is suppressed by applying pressure or introducing the disorder by X-ray irradiation. Figure 2.1 and 3.12 show the temperature dependence of $1/T_1T$ of κ-NCS and κ-Br salts under several pressures [36, 11]. Applying the pressure causes the increase in the bandwidth, then density of states decreases. As a result, $(1/T_1T)_{\rm FL}$ term decreases. Concomitantly, the

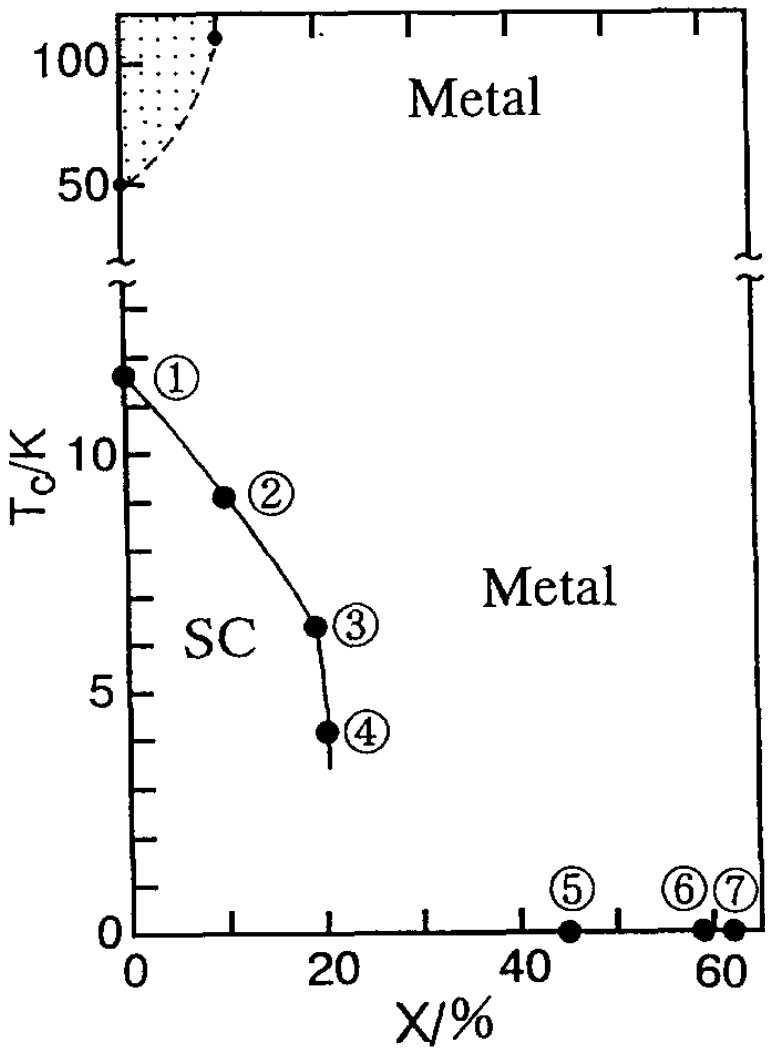

Figure 3.11: The relation between x and T_c [35].

peak of $1/T_1T$ at T^* is suppressed and shifts to high temperature. These results are considered as the suppression of antiferromagnetic fluctuation. Temperature dependence of $1/T_1T$ of X-ray irradiated κ-NCS salt are shown in Fig. 3.13 [37]. The $(1/T_1T)_{\rm FL}$ term does not change but only $(1/T_1T)_{\rm AF}$ term is suppressed because disorder can disrupt the correlation of antiferromagnetic fluctuation.

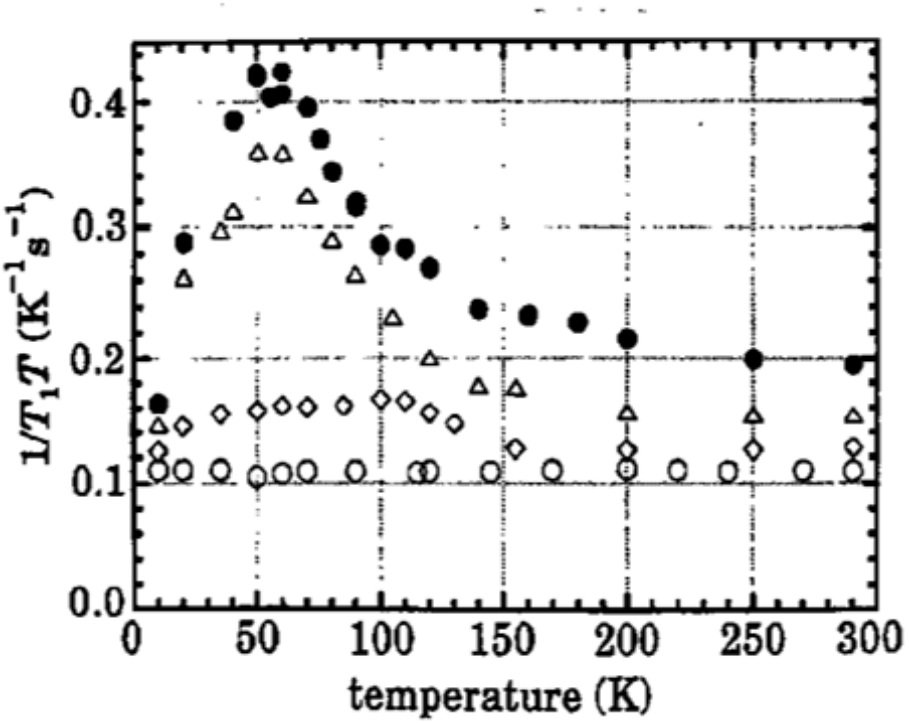

Figure 3.12: Temperature dependence of $1/T_1T$ of κ-Br under several pressures [36].

NMR study on impurity effect

As mentioned above, decrease in T_c by nonmagnetic impurity for anisotropic superconductor is larger than that for isotropic superconductor. Nonmagnetic impurity causes potential scattering near the Fermi surface. In s-wave superconducting gap, as shown in Fig. 2.4, there is no density of states at E_F. Therefore, small impurity doping does not affect the quasiparticle density of states. On the other hand, because of finite density of states at E_F in d-wave superconductor, residual density of states by impurity scattering is observed by doping small amount of impurity. Residual density of states below T_c can be observed by $1/s$. Figure 3.14 shows the temperature dependence of $1/T_1$ in (a) $Mg_{1-x}Al_xB_2$ [38] and (b) $YBa_2(Cu_{1-x}Zn_x)_3O_7$ [39]. In $Mg_{1-x}Al_xB_2$, temperature dependence of $1/T_1$ normalized at T_c [inset of Fig. 3.14(a)] is almost the same between $x = 0$ % and 5 %. However, $1/T_1$ at the lowest temperature increases with increasing the doping

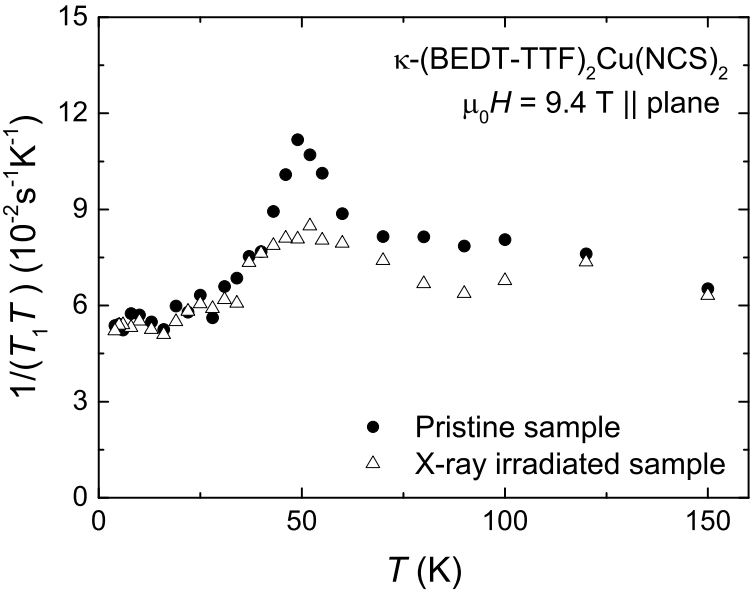

Figure 3.13: Temperature dependence of $1/T_1T$ of X-ray irradiated and pristine κ-NCS [11, 37].

ratio in $YBa_2(Cu_{1-x}Zn_x)_3O_7$. Therefore, increase in the residual density of states in anisotropic superconductor is the good evidence that the Cooper pair is scattered by impurity. We investigated that the behavior of $1/T_1$ below T_c to reveal the doping effect in κ-Br salt.

The local electronic state at the impurity site should be revealed to understand the pair breaking mechanism. The microscopic experiment that can probe microscopically the local electronic state is desired. The electronic spin state near the impurity site was investigated in cuprate superconductors using the NMR spectroscopy [40]. Figure 3.15 shows the temperature dependence of $1/T_1$ of Zn 1 % doped $YBa_2Cu_3O_7$. The Cu site near the nonmagnetic Zn impurity (open circles) is more strongly affected compared to the Cu site far from the impurity (closed circles). Precise NMR experiment detected separately the signal from Cu nuclei near the Zn impurity, and revealed that the nonmagnetic impurities induce staggered moment in the cuprate superconductors. However, NMR signal from Zn site cannot be observed because of very strong magnetic fluctuations at the impurity site. The ^{13}C NMR study on BEDT-STF-doped salts provides important information because we can observe selectively the electronic properties at the BEDT-TTF sites and the BEDT-STF sites by doping naturally abundant BEDT-STF molecules into ^{13}C enriched κ-Br salt (BEDT-TTF sites), and by doping the ^{13}C enriched BEDT-STF molecules into the naturally abundant κ-Br salt (BEDT-STF sites).

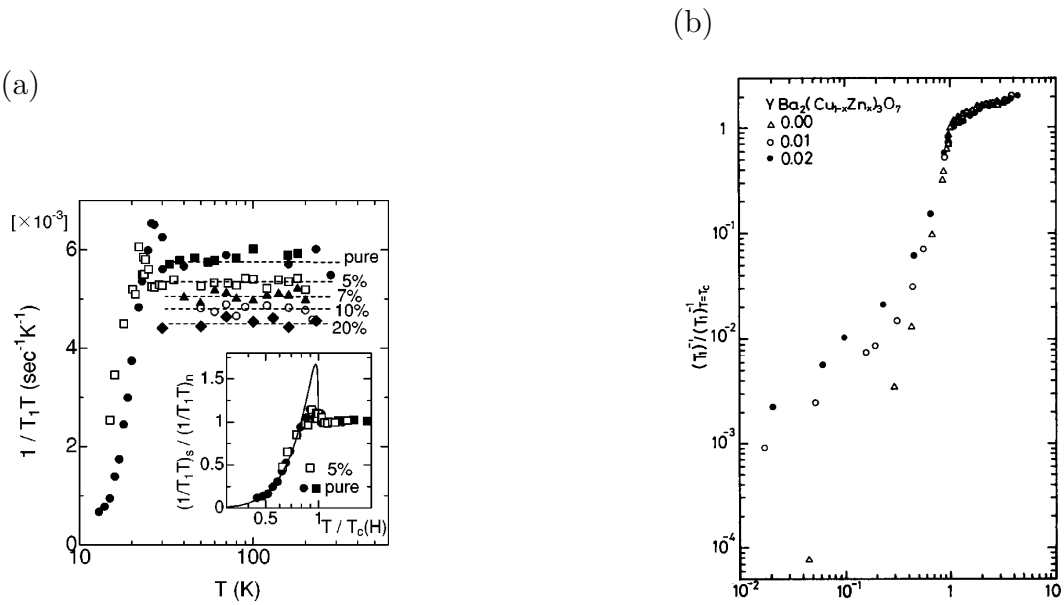

Figure 3.14: Temperature dependence of $1/T_1$ in several doping ratio of nonmagnetic impurity. Left: $Mg_{1-x}Al_xB_2$. Right: $YBa_2(Cu_{1-x}Zn_x)_3O_7$. [38, 39]

3.4.3 Superconducting fluctuation

Near the second order phase transition, thermal and quantum fluctuations induce a short-range coherence even above T_c. The universality of physical quantities in this critical regime has been intensively studied for various types of magnetic transitions. For the second-order superconducting transition, the short-range coherence of superconducting order parameter should also be induced in the normal state, where the thermal average of order parameter does not possess the finite value. The prominent effect of fluctuating superconducting order parameter was observed by the Nernst effect measurement on cuprate superconductor [41], in which a vortex-like signal was detected in the critical regime above T_c. To understand the mechanism for the fluctuating superconducting order parameter to affect the bulk properties, both theoretical and experimental studies have been carried out on the high-T_c superconductors [42, 43, 44, 45]. However, enhanced magnetic fluctuations, which originate from the antiferromagnetic transition near the superconducting phase, contaminate the pure effect of fluctuating superconducting order parameter. In order to investigate the critical fluctuation of superconducting order parameter, we should examine a superconductor that shows superconducting transition in the conventional Fermi liquid state.

Recently, the vortex-like signal was observed above T_c in κ-Br salt by Nernst effect measurement [46]. This report leads us to study the fluctuating superconducting state in a series of κ-(BEDT-TTF)$_2X$ salts, because in the organic superconductors the conventional Fermi liquid state is established when superconductivity sets in [47, 48]. Besides, the effects associated with superconductivity can be controlled by magnetic fields, as the upper critical field $H_{c2}^{\perp} \simeq 10$ T [13, 24]

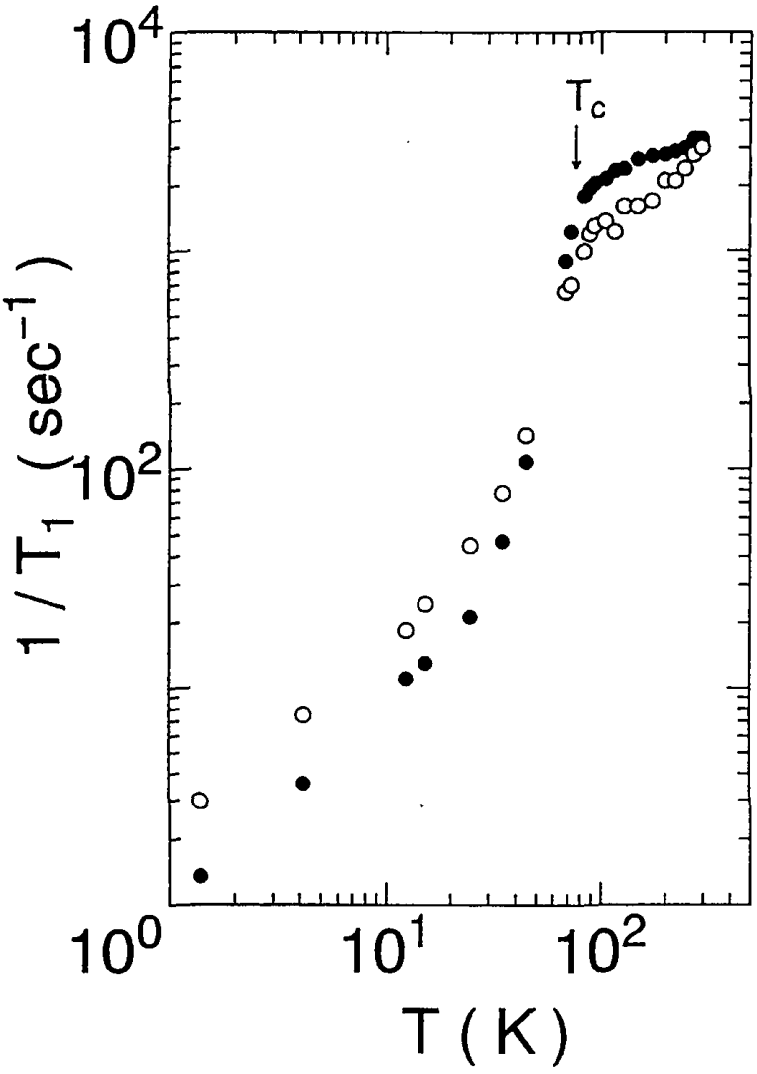

Figure 3.15: Temperature dependence of $1/T_1$ of $YBa_2(Cu_{1-x}Zn_x)_3O_7$ ($x = 1$ %). Closed (open) circles indicate Cu site far from (near) the Zn impurity. [40]

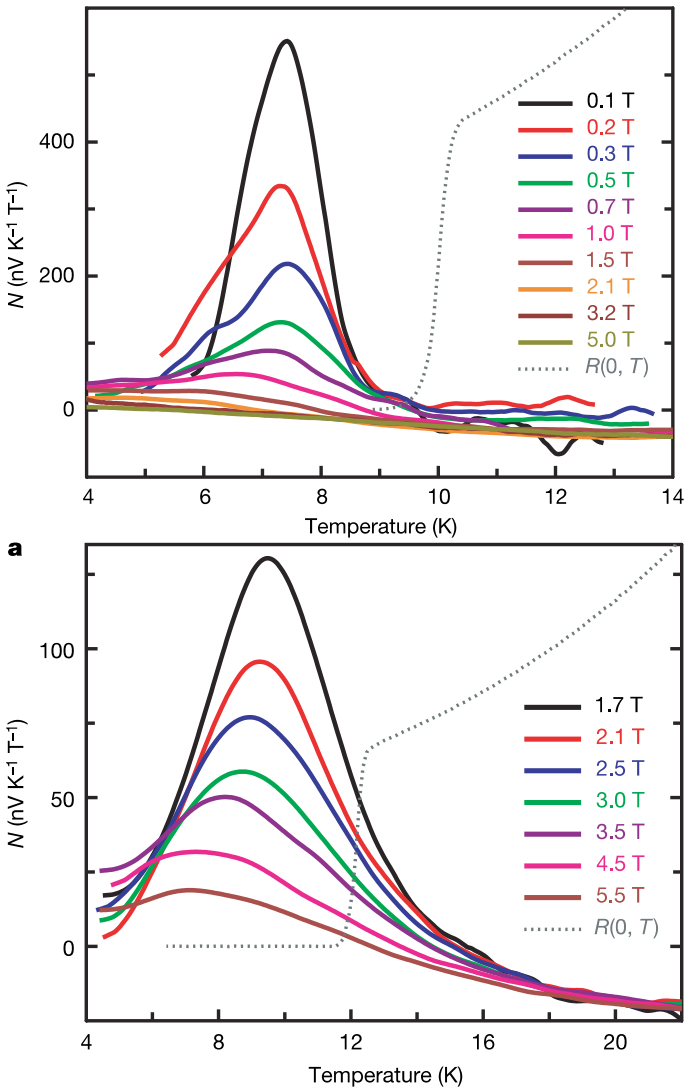

Figure 3.16: Temperature dependence of Nernst signal of κ-NCS (upper panel) and κ-Br (lower panel) salts under the various magnetic fields (solid lines) and resistivity at the zero field (dotted lines) [46]

is accessible with conventional superconducting magnets. The results of Nernst effect measurements in κ-Br and κ-NCS salts are shown in Fig. 3.16. Solid lines are the temperature dependence of Nernst signal under the several magnetic fields and dotted lines are the temperature dependence of resistivity at the zero field. In this study external magnetic fields were applied perpendicular to the conduction plane. Increase in the Nernst signal of κ-NCS salt starts at lower temperature than the temperature where zero resistivity was observed. Whereas, field-dependent Nernst signal increases from 18 K, which is much higher than T_c, in κ-Br salt. They claimed that the region of superconducting fluctuation increases in the vicinity of antiferromagnetic phase.

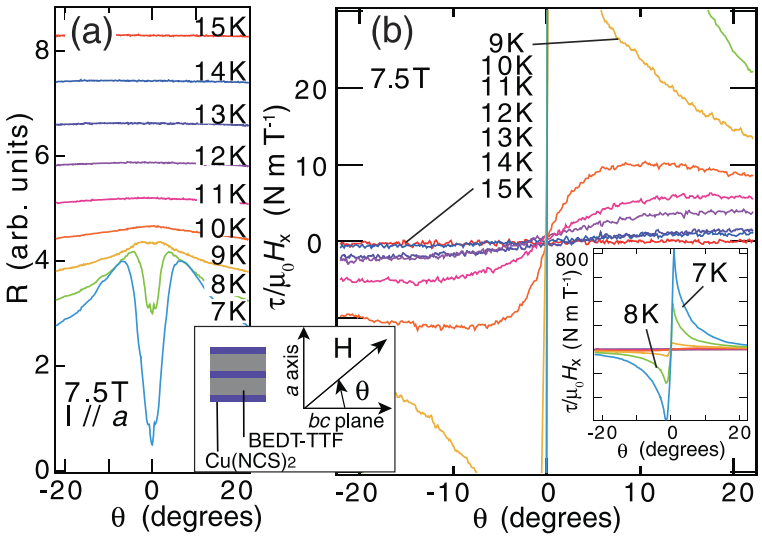

Figure 3.17: Angular dependence of the (a) interlayer resistance and (b) magnetic torque at 7.5 T for various temperatures in κ-NCS . The inset of (a) shows a schematic of the crystal structure and the definition of the field angle. The inset of (b) shows the overall views of the torque curves [49].

On the other hand, comparable critical regime for both κ-Br and κ-NCS salts was observed by magnetic torque measurements [49, 50]. Figure 3.17(a) and (b) shows the angular dependence of resistance and magnetic torque measurements of κ-NCS salt at 7.5 T. The Meissner signal due to the superconducting fluctuation was observed in the torque measurement below 12 K, although resistance drops at zero degrees due to superconductivity was only observed below 8 K. The inconsistency of Nernst and torque measurements might be due to the difference in the external field direction. The external field was applied perpendicular to the conduction plane for the Nernst effect measurement, whereas parallel to the conduction plane for the magnetic torque measurement. As the field orientation cannot be changed for these experimental techniques, other experiments that can be conducted in both parallel and perpendicular fields are required. In this work, we report

the results of ^{13}C NMR experiment on κ-Br and κ-NCS salts. As the experimental accuracy does not depend on the external field orientation, we applied the magnetic fields both parallel and perpendicular to the conduction plane, and measured the nuclear spin-lattice relaxation time T_1.

NMR study on superconducting fluctuation

In addition to the Nernst and torque measurements, the precursor of superconducting transition above T_c was also detected by magnetization measurements [51, 52]. These experiments probed the vortices generated by the short-range Cooper pairs in the normal state, and confirmed that fluctuating superconducting state is realized in κ-Br salt. However, because of the large magnetization of vortices, we cannot explore the variation of quasi-particle density of states in the fluctuating superconducting state, which is essential for the microscopic understanding of critical superconducting fluctuation [53].

The NMR spectroscopy enables us to measure directly the quasi-particle density of states when the system is in the Fermi liquid state. The previous T_1 measurement was performed on cuprate superconductors. Figure 3.18 shows the temperature dependence of $1/T_1T$ of $YBa_2Cu_3O_{6.95}$ in the magnetic fields from 2.1 T up to 27.3 T. Although T_c at zero field is 92.5 K, $1/T_1T$ increases with increasing field below 120 K. However, T_1 measurement could not observe separately the effect of superconducting fluctuations [44, 43], because the strong spin fluctuations near antiferromagnetic phase violate the conventional Fermi liquid state. In the organic superconductors, as the spin fluctuations are weak enough to stabilize the Fermi liquid state above T_c, NMR experiment should be performed on κ-(BEDT-TTF)$_2X$ salts.

When a system is in a Fermi liquid state, $1/T_1T$ is temperature-independent [eq. (2.4)]. This relation is modified either by enhanced magnetic fluctuations near magnetic transition, or by the superconducting fluctuation near T_c, which corrects the quasi-particle density of states [44, 54]. Theoretical study has revealed that superconducting fluctuations can correct quasi-particle density of states in three different processes, which are called Aslamazov-Larkin, Maki-Thompson, and density of states processes [45]. While Aslamazov-Larkin process is irrelevant to the dynamical susceptibility which determines $1/T_1T$, density of states process reduces the quasi-particle density of states and Maki-Thompson process increases them.

3.5 Purpose of this study

Although the study of impurity effect on superconductivity was performed in κ-Br salt by BEDT-STF doping, the effect of impurity doping on the electronic state is unclear. BEDT-STF

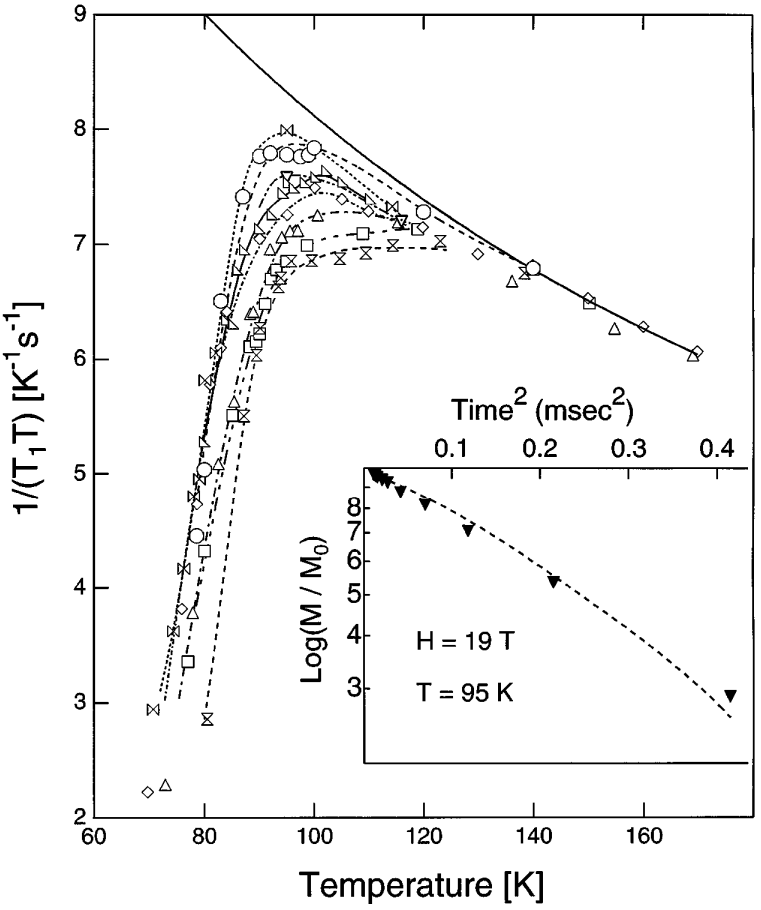

Figure 3.18: Temperature dependence of $1/T_1T$ of $YBa_2Cu_3O_{6.95}$ in the magnetic fields from 2.1 T up to 27.3 T [43].

doping causes the reduction of T_c whether by impurity effect or chemical pressure effect. Impurity effect causes the potential scattering and chemical pressure effect causes the increase in bandwidth then magnetic correlation is weakened. In order to reveal the mechanism of BEDT-STF doping effect, we performed NMR measurements.

Superconducting fluctuation was studied in the cuprate superconductor, but detailed study is difficult due to the magnetic fluctuation above T_c. In κ-Br salt Fermi liquid state is established just above T_c and large superconducting fluctuation region was observed. We focus on this material and investigate the electronic state in the superconducting fluctuation state.

Chapter 4

Experiments

4.1 Sample preparation

We utilized the ^{13}C enriched (hot) BEDT-TTF molecule, for which single side of the central C = C bond was enriched with ^{13}C [left hand side of Fig. 4.1(a)] [55]. This asymmetric molecule eliminates the NMR peak splitting due to the nuclear spin-spin coupling at the C = C bond (Pake doublet) [56].

In the study of impurity effect, we prepared four kinds of molecules, which are hot BEDT-TTF, naturally abundant (cold) BEDT-TTF, hot BEDT-STF, and cold BEDT-STF molecules (Fig. 4.1). For the hot BEDT-STF molecule the carbon nuclei at the sulfur side of the central C=C bond was selectively enriched. As the ^{13}C NMR signal originates only from the enriched ^{13}C nuclei, these molecules allow us to study the impurity effect on bulk electronic properties by doping cold BEDT-STF molecule to hot BEDT-TTF crystal [TTF-7 and TTF-9, as shown in Fig. 4.1(a)], and the local impurity scattering effect by doping hot BEDT-STF molecule to cold BEDT-TTF crystal [STF-10, as shown in Fig. 4.1(b)]. The BEDT-STF molecules can enter into the BEDT-TTF crystal by solving both BEDT-STF, and BEDT-TTF molecules during the electrochemical oxidation process [34]. We checked that BEDT-STF molecule is uniformly introduced in the sample by the X-ray microprobe analysis.

The superconducting diamagnetism of BEDT-STF doped samples was observed using a SQUID magnetometer (Quantum Design, MPMS). As shown in Fig. 4.2 (a), the superconducting transition of doped sample is as sharp as that of pristine sample, which indicates the uniform doping of BEDT-STF molecule. We determined the actual BEDT-STF concentration x by comparing T_c of each sample with the previously established x to T_c relation [Fig. 4.2 (b)] [34]. As shown in Table 4.1, the determined x values (7 %, 9 %, and 10%) are smaller than the nominal values (8 %, 15 %, and 15 %), because the solubility of BEDT-STF molecule is smaller than that of BEDT-TTF molecule.

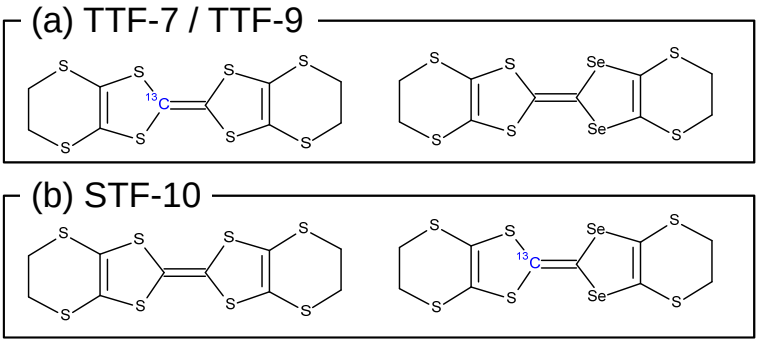

Figure 4.1: Combination of BEDT-TTF and BEDT-STF molecules in the samples prepared in present study. TTF (STF) indicates that BEDT-TTF (BEDT-STF) molecule is ^{13}C enriched. Number is the concentration of BEDT-STF molecule. These labels are defined in Table 4.1.

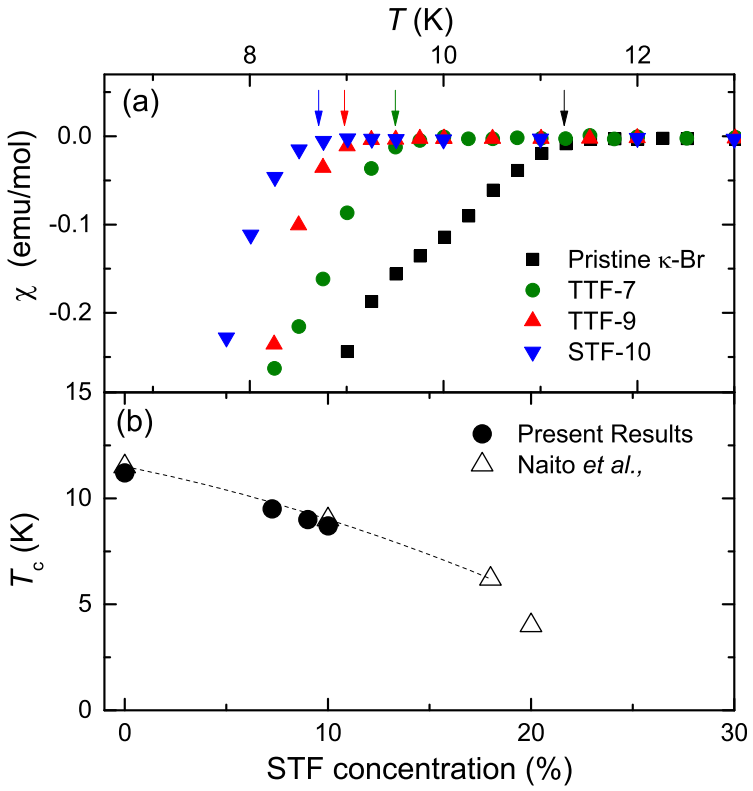

Figure 4.2: (a) Temperature dependence of magnetic susceptibility in each sample. Arrows indicate the T_c. (b) The plot of T_c versus STF concentration. The data of open triangular was measured by Naito *et al*. [34], Closed circles represent the present results. T_c is determined by (a) and STF concentration is the result of comparison to triangular. Dashed line is the quadratic function.

T_c of κ-Br and κ-NCS salts were also checked by magnetization measurement for the study of superconducting fluctuation. We determined the the mean-field T_c of our samples at low field as $T_c = 11.4$ K for κ-Br , $T_c = 9.3$ K for κ-NCS , which are consistent with the previous studies [7, 5].

4.2 Magnetic susceptibility measurement

In order to examine the effect of BEDT-STF doping to bulk properties, temperature dependence of static magnetization in the normal state was measured for the TTF-9 sample, the mass of which is 2.5 mg. Magnetic field of 4 T was applied perpendicular to the conduction plane.

4.3 NMR measurement

The NMR spectra and spin-lattice relaxation time T_1 were measured using a spin-echo method and a saturation recovery method. In the study of impurity effect, the external magnetic fields of 7 T for pristine sample and 6.7 T for BEDT-STF doped samples were applied along the crystalline c direction (in-plane), for which the upper critical field is higher than 30 T [14]. In the study of superconducting fluctuation, NMR experiments were performed under the several magnetic fields for κ-Br and κ-NCS salts. The direction of the external magnetic field was perpendicular (b-axis for κ-Br and a^*-axis for κ-NCS) and parallel (c-axis for κ-Br and any in-plane direction for κ-NCS) to the conduction plane. We also performed NMR experiments on deuterated κ-$d[n, n]$-Br salts ($n = 2, 4$), in which the hydrogen at the ethylene group of BEDT-TTF molecule was partially and fully enriched with deuteron for n is 2 and 4, respectively. The deuteration to κ-Br salt brings the electronic state toward the antiferromagnetic phase [57]. For the deuterated samples, field orientation was fixed to the c direction to eliminate the angle dependence of $1/T_1T$ values originating from the angle dependent hyperfine coupling constant and investigated quantitatively the deuteration effect.

Table 4.1: List of samples

Sample	^{13}C enriched molecule	T_c	x
pristine	BEDT-TTF	11.2 K	0 %
TTF-7	BEDT-TTF	9.5 K	7 %
TTF-9	BEDT-TTF	9.0 K	9 %
STF-10	BEDT-STF	8.7 K	10 %

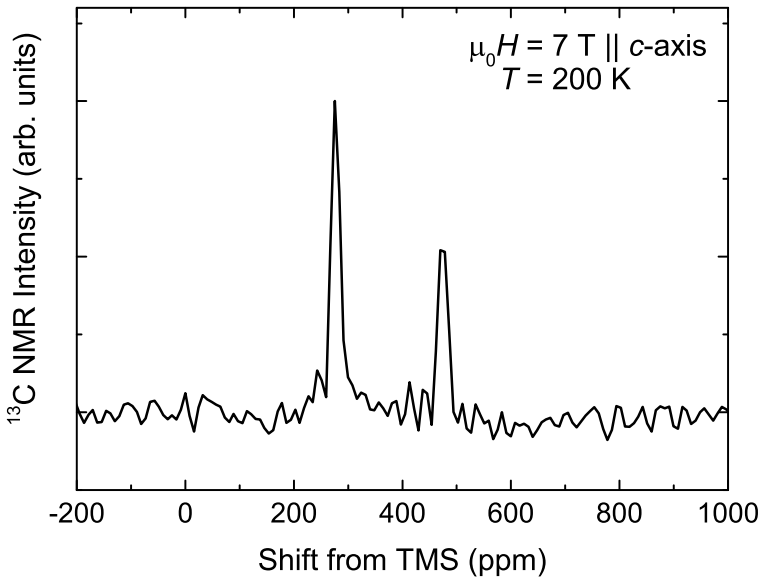

Figure 4.3: NMR spectrum of κ-Br

Figure 4.3 shows the NMR spectra of κ-Br salt obtained at 200 K. The horizontal axis is the NMR frequency shift with respect to the reference material of tetramethylsilan (TMS). For κ-Br salt, distinct two peaks were observed. In principle, as κ-Br salt possesses eight independent ^{13}C sites in magnetic fields, eight NMR peaks from each ^{13}C would be expected. In the field parallel to c direction, however, every four peaks are superposed, and thus the two-peak structure is observed. These two sites originate from two nonequivalent carbon sites at the C=C bond. Each side of the C=C bond becomes nonequivalent when two BEDT-TTF molecules form a dimer. One site which is close to the center of BEDT-TTF dimer is called inner site, and the other is called outer site. From the field orientation dependence of peak positions studied by Soto *et al.* [58], peaks at 277 ppm and 474 ppm were respectively assigned to the inner and outer sites.

For the T_1 measurement, we integrated the NMR intensity of both inner and outer sites to obtained the recovery profile of the nuclear magnetization, because the two peaks merge to form a single peak at low temperature due to spectral broadening. As T_1 for the inner site ($T_1^{\rm inner}$) and the outer site ($T_1^{\rm outer}$) are different, we introduced a two-exponential function to fit the recovery profile,

$$\frac{M_0 - M(t)}{M_0} = 0.5 \exp\left(-\frac{t}{T_1^{\rm outer}}\right) + 0.5 \exp\left(-\frac{t}{T_1^{\rm inner}}\right). \tag{4.1}$$

Here, $M(t)$, M_0 represent the nuclear magnetization at t, in the thermal equilibrium state, respectively. When the well-separate two-peak spectra are observed, $T_1^{\rm inner}$ and $T_1^{\rm outer}$ can be measured independently. From the separately obtained $T_1^{\rm inner}$ and $T_1^{\rm outer}$ in κ-Br salt at the normal state, the ratio $T_1^{\rm inner}/T_1^{\rm outer}$ appears to be temperature independent, and its value is almost 3. Figure 4.4 and

4.5 show the recovery curves of the nuclear magnetization in the study of superconducting fluctuation and impurity effect, respectively. Dashed line and solid line are corresponding to eq. (4.1). All data is well fitted by this formula.

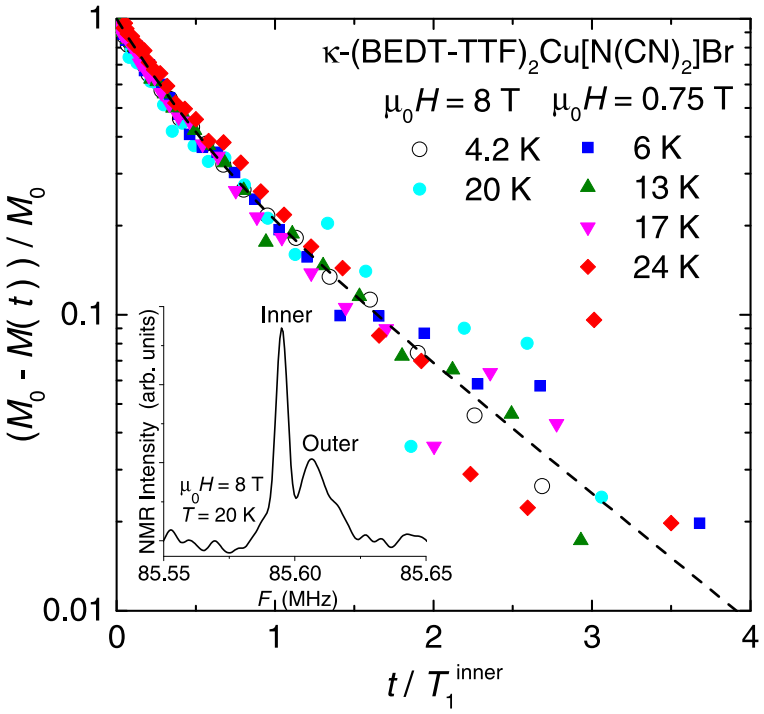

Figure 4.4: Recovery profile of nuclear magnetization of κ-Br at several magnetic fields and temperatures. The horizontal axis was scaled by $T_1^{\rm inner}$ determined at each temperature.

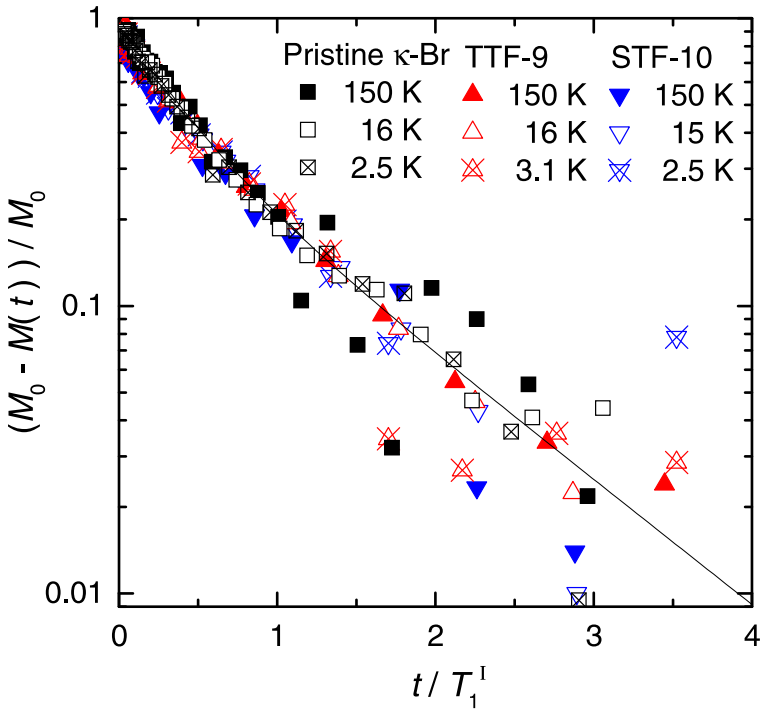

Figure 4.5: Recovery profile of nuclear magnetization of pristine κ-Br , TTF-9, and STF-10 samples at several temperatures. The horizontal axis was scaled by $T_1^{\rm inner}$ determined at each temperature.

Chapter 5

Results

5.1 Impurity effect

Figure 5.1 shows the spin susceptibility $\chi_{\rm spin}$ for TTF-9 below 150 K, in which the core diamagnetic contribution (-4.7×10^{-4} emu/mol) is subtracted. In order to compare the $\chi_{\rm spin}$ of TTF-9 with pristine κ-Br , we showed the previous data of pristine sample [12]. In the pristine sample the slope of $\chi_{\rm spin}$ changes at 35 K. This behavior was interpreted as due to the suppression of the antiferromagnetic fluctuation [23]. In TTF-9, deviation was observed at almost 45 K. This result implies that BEDT-STF doping suppresses the antiferromagnetic fluctuation and consistent with the present results of NMR spectroscopy.

5.1.1 Local distortion by BEDT-STF doping

The broad NMR spectrum of TTF-9, shown in Fig. 5.2, indicates that the BEDT-STF doping introduced the distribution in either $A_{\rm hf}$ or χ, both of which are determined by the electronic state at the Fermi energy. In the spectrum of TTF-9, we could not resolve the signal from BEDT-TTF sites close to or far from the BEDT-STF sites. The linewidth (inner site) of 106 ppm in TTF-9 is broader than that of 17 ppm in pristine κ-Br salt at 200 K. This line broadening was also observed in the samples, in which inhomogeneity is introduced by the X-ray irradiation [37, 22]. The X-ray irradiation to κ-Br salt induces metallic conductivity at high temperatures [59]. The comparable linewidth induced by BEDT-STF doping and X-ray irradiation leads us to expect that the conduction electrons are significantly modified by the BEDT-STF impurities.

Although broadened, the peak positions of TTF-9 are identical to those of pristine sample. This result suggests that at high temperatures the impurity effect appears locally, and the averaged magnetization over entire sample are almost unchanged. Whereas for STF-10, as σ and $A_{\rm hf}$ for

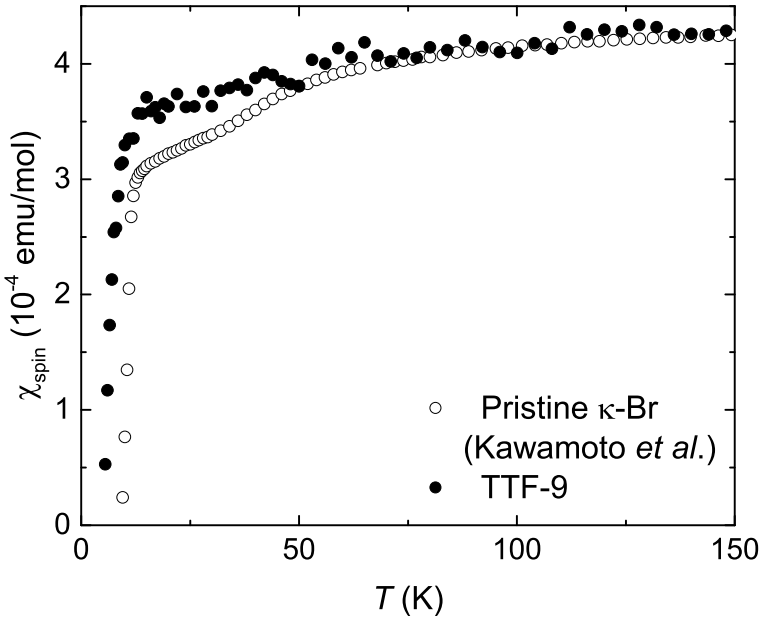

Figure 5.1: Temperature dependence of spin susceptibility of TTF-9 under the magnetic field of 4 T perpendicular to the conduction plane. The data of pristine κ-Br was previously reported by Kawamoto *et al.* [12].

BEDT-STF molecular orbital is different from those of BEDT-TTF molecule, the peak positions are shifted, and the peak separation becomes small. To this time, σ for BEDT-STF molecule has not been determined. However, the separation between two peaks ΔK is proportional only to $A_{\rm hf}\chi$ and independent of σ because σ is almost identical between inner and outer sites. The ratio of ΔK between STF-10 and pristine sample is 1.43. The bulk magnetization measurement, and NMR shift measurement in TTF-9 suggest that the uniform susceptibility χ is not modified by the BEDT-STF doping of less than 10 %. From this result we can assume that the small ΔK in STF-10 is mainly due to the small $A_{\rm hf}$ at the BEDT-STF molecule. As $A_{\rm hf}$ is directly related to the local electronic structure, the small $A_{\rm hf}$ at the BEDT-STF site indicates that the electronic states are locally distorted, which will then scatter the conduction electrons.

5.1.2 Magnetic fluctuation in the normal state

The bulk magnetization is almost unchanged by BEDT-STF doping at the temperatures higher than 100 K. At low temperatures, however, the suppression of magnetic fluctuations were observed from $1/T_1T$ measurement. As shown in Fig. 5.3, in pristine sample a maximum of $1/T_1T$ was observed at $T^* = 50$ K, below which $1/T_1T$ decreases and becomes temperature independent in the Fermi liquid state just above T_c. In TTF-7 and TTF-9, the peak behavior of $1/T_1T$ around T^*

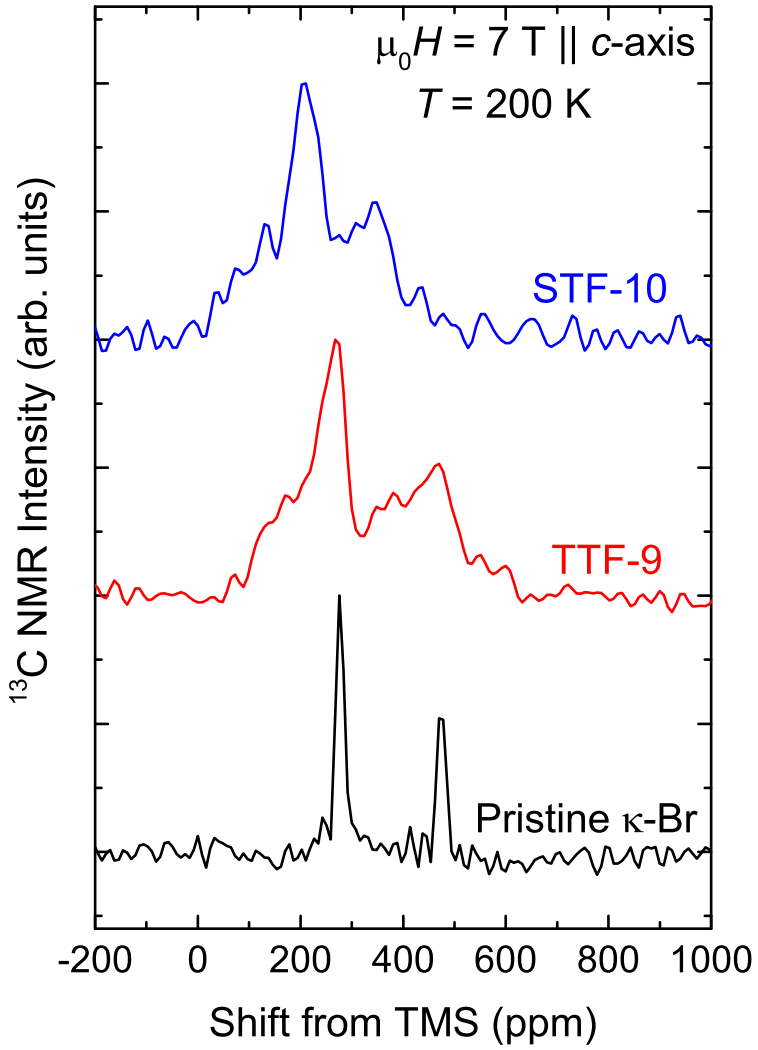

Figure 5.2: NMR spectrum in pristine κ-Br, TTF-9 and STF-10 samples at 200 K. Magnetic field of 7 T was applied parallel to c-axis.

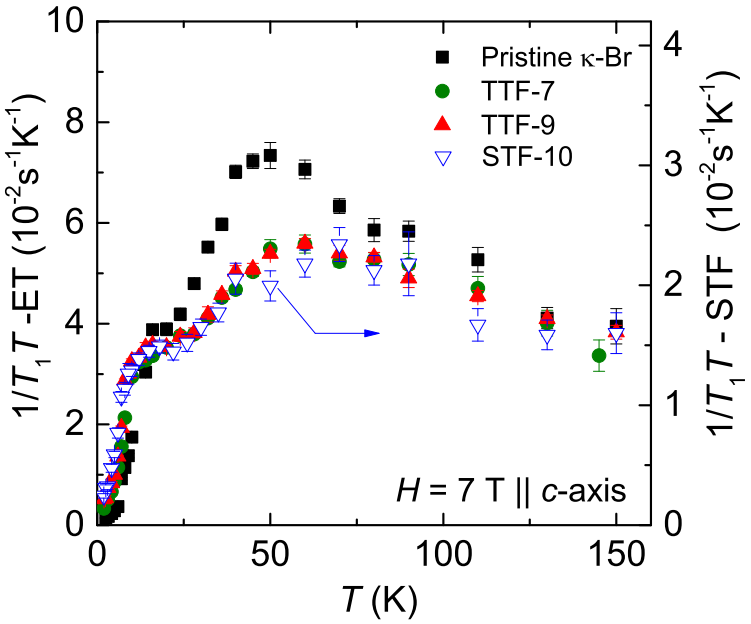

Figure 5.3: Temperature dependence of $1/T_1T$ for various salts. Left scale is corresponding to the $1/T_1T$ of pristine κ-Br, TTF-7 and TTF-9. Right scale is corresponding to that of STF-10.

is reduced, and the Fermi liquid behavior was observed from the temperatures higher than that in pristine sample. As the $(1/T_1T)_{\rm AF}$ term increases at low temperature, the suppression of the peak behavior at T^*, and doping independent high temperature behavior indicate that the $(1/T_1T)_{\rm AF}$ term is suppressed, but the $(1/T_1T)_{\rm FL}$ term is barely affected by BEDT-STF doping. When a mechanical pressure is applied to κ-Br salt, the$(1/T_1T)_{\rm FL}$ term is reduced because of the increase in the bandwidth, and accordingly the $(1/T_1T)_{\rm AF}$ term is suppressed [36]. The suppression of only $(1/T_1T)_{\rm AF}$ term was observed in the X-ray irradiated κ-(BEDT-TTF)$_2$Cu(NCS)$_2$, in which the antiferromagnetic correlation is disturbed by the vacancies introduced by X-ray irradiation [37]. The BEDT-STF doping effect can be understood as the scattering of antiferromagnetic correlations by the BEDT-STF impurity. When conventional Lorentz form is assumed for the dynamical susceptibility,

$$\chi(Q,\omega) = \frac{\chi_0}{1 + Q^2\xi^2 - i\omega/\Gamma}, \tag{5.1}$$

its temperature dependence is characterized by the antiferromagnetic correlation energy Γ. The temperature dependence of $1/T_1T$ above 100 K is identical between TTF-9 and pristine samples. This result suggests that the BEDT-STF doping does not modify the antiferromagnetic correlation energy, but does limit the antiferromagnetic correlation length ξ to the mean impurity-impurity distance at low temperatures. As Γ should be reduced when the bandwidth becomes large, the invariant Γ after BEDT-STF doping is consistent with the small effects on $(1/T_1T)_{\rm FL}$ term. The

bulk effect of BEDT-STF impurity has been revealed by studying TTF-7, and TTF-9. Now, the local effect at the BEDT-STF site can be investigated by measuring STF-10. The result of $1/T_1T$ measurement on STF-10 is shown in Fig. 5.3 with the right scale. The temperature dependence of $1/T_1T$ in STF-10 can be scaled to TTF-9 at all temperature range by multiplying a factor of 2.4. As shown in eq (2.4), $1/T_1T$ is proportional to $A_{\rm hf}^2$. Since the obtained constant factor of 2.4 is close to the square of the ratio between $A_{\rm hf}$ for BEDT-TTF and BEDT-STF molecules, which has been estimated as 1.43 from the separation of two-peak NMR spectra, this factor is explained only by the difference in $A_{\rm hf}$. The consistency between NMR shift and $1/T_1T$ results strongly suggests that the magnetic susceptibility is uniformly modulated, and the local susceptibility at the BEDT-STF sites is equivalent to the other BEDT-TTF sites. In a case of nonmagnetic Zn doping to YBCO, a staggered moment is induced near the nonmagnetic impurity. A strong magnetism is not induced at and near the BEDT-STF sites, because the frontier molecular orbital, which is constituted of 10 carbon and 8 sulfur atomic orbitals, is not significantly modified by substitution of two Se atoms. Whereas for cuprate, as the whole atomic orbital is replaced by substituting Zn atom for Cu atom, drastic change in local magnetism was observed. We conclude that the BEDT-STF impurity brings about a weak potential disorder in the conduction band.

The impurity potential of BEDT-STF molecules can be estimated by calculating the binding energy of the highest occupied molecular orbital (HOMO). The HOMO energy of BEDT-TTF $E_{\rm TTF}$ and BEDT-STF $E_{\rm STF}$ calculated numerically by MOPAC 2012 program are $E_{\rm TTF} = -6.9810$ eV and $E_{\rm STF} = -6.7058$ eV. In κ-Br salt, two BEDT-TTF molecules form a dimer, and the bonding orbital of the dimer is at the Fermi energy. The energy for the bonding orbital of the BEDT-TTF=BEDT-STF dimer can be calculated as -7.12 eV, which is 0.10 eV larger than the energy for BEDT-TTF dimer. A dimer with two BEDT-STF moleculs can be neglected, because its concentration is only 1 % when the BEDT-STF doping concentration is 10 %. As the bandwidth has been estimated as 0.6 eV [19], the impurity potential of 0.1 eV will scatter weakly the conduction electrons.

5.1.3 Superconducting breaking effect

At high temperature, the small potential disorder appears to be detrimental to the long range magnetic correlations. In this subsection we discuss the impurity scattering effect on superconducting properties. For pristine sample in 7 T, $1/T_1T$ demonstrates T^2 temperature dependence just below T_c, and the Fermi liquid-like behavior ($1/T_1T \propto$ const.) appears at low temperatures (Fig. 5.4). This temperature dependence is characteristic of unconventional superconductivity with nodes on superconducting gap. The low-temperature Fermi liquid-like behavior originates from

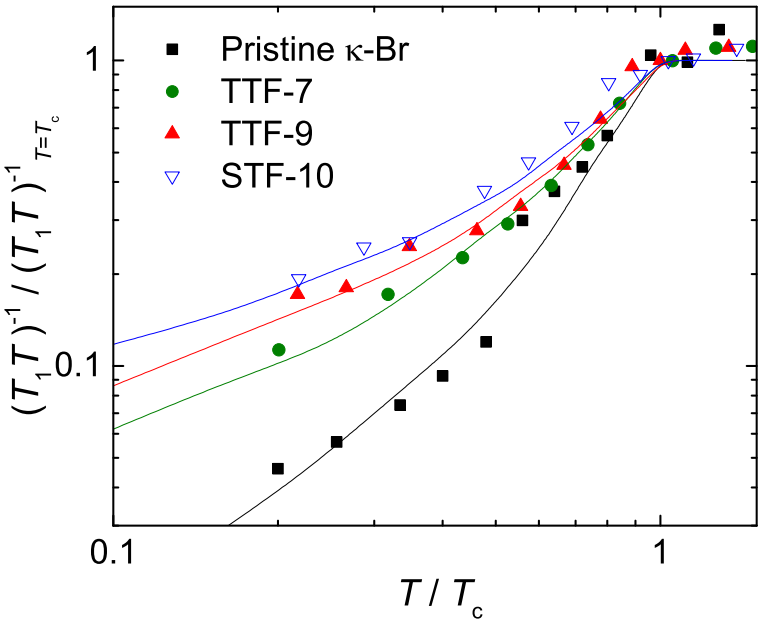

Figure 5.4: Temperature dependence of $1/T_1T$ in each sample for the superconducting state. Vertical and horizontal axes are normalized at the value of T_c. Solid lines are the calculation by considering the residual density of states near the Fermi energy.

the residual density of states induced near the gap nodes by the external magnetic fields. The overall temperature dependence in the superconducting state is consistently explained by a model of d-wave superconducting gap with some residual density of states at low energy. The good fit of our calculation to the experimental data confirms that superconductivity in κ-Br possesses a d-wave symmetry.

In TTF-7 and TTF-9, $1/T_1T$ at the lowest temperature increases with increasing the doping concentration. As $1/T_1T$ at the lowest temperature is determined by the residual DOS, the increase in $1/T_1T$ by doping indicates that the impurity scattering generates additional DOS. The impurity scattering rate $1/\tau$ can be estimated by fitting $1/T_1$ data to our model calculation. We can determine DOS with impurity scattering by Eilenberger equation [60]. From the diagonal components of quasiclassical Green's function

$$g = \frac{w_l + \hbar\langle g\rangle/2\tau}{\sqrt{(w_l + \hbar\langle g\rangle/2\tau)^2 + |\Delta|^2|\phi|^2}}, \tag{5.2}$$

DOS is obtained after the analytic continuation to the real axis, $\omega_l \to -i\omega + \delta$. Here, ω_l is the Matsubara frequency and defined as $(2l + 1)\pi k_B T$ (l = 0,1,2,$\cdots$). Δ is gap function and ϕ is anisotropy factor. We hypothesized the two dimensional d-wave anisotropy, $\phi(\boldsymbol{k}) = \cos 2\theta_{\boldsymbol{k}}$. The results for TTF-7, TTF-9 and pristine κ-Br are shown in Fig. 5.4 (solid lines). For pristine κ-Br, we assumed that the residual DOS are generated by the scattering by vortex cores. This assumption is

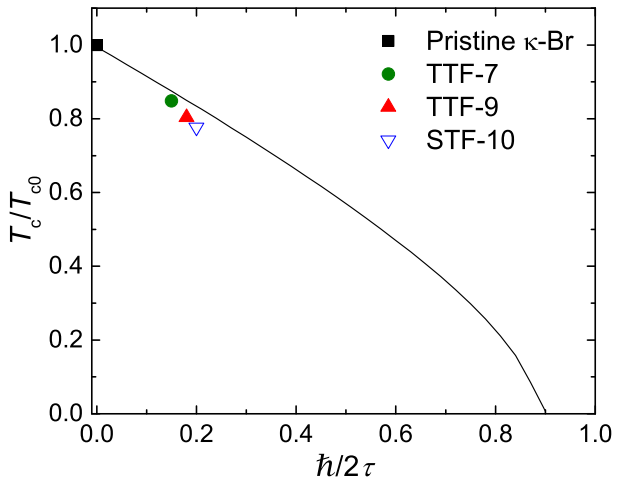

Figure 5.5: Relation between T_c and $\hbar/2\tau$. $T_{c0} = 11.2$ K and T_c of each sample are displayed in Table 4.1. $\hbar/2\tau$ was determined by fitting $1/T_1$ data to model calculation. The solid curve is calculated from eq. (5.3).

valid in the present context, as all the NMR experiments were performed in a comparable magnetic field strength, and therefore residual DOS induced by magnetic fields should be constant for all sample no matter what the mechanism is. As a result, the values of $\hbar/2\tau$ are 0, 0.15, 0.18 for pristine κ-Br, TTF-7 and TTF-9, respectively. A more sophisticated calculation, which includes DOS generation by Doppler shift, will be required to compare the results obtained in different magnetic fields.

The relation of the observed T_c and the parameter of $\hbar/2\tau$ for each sample is plotted in Fig. 5.5. Solid line shows the suppression of T_c from the T_c of pristine κ-Br, T_{c0}, which is calculated using the scattering time τ as [61]

$$\ln \frac{T_c}{T_{c0}} + 2\pi k_B T_c \sum_{l=0}^{\infty} \left(\frac{1}{\omega_l} - \frac{1}{\omega_l + \hbar/2\tau} \right) = 0. \tag{5.3}$$

The observed T_c for each sample is almost explained by this relation, which suggests that the impurity potential of BEDT-STF molecular orbitals scatters the quasiparticles, and suppresses T_c. The decreasing rate of T_c/T_{c0} for experiments is slightly larger than that for calculation. This result indicates that another factor of decrease in T_c exists, that is, chemical pressure effect. Substituting of BEDT-STF molecule for BEDT-TTF molecule causes the increase in bandwidth, and then in the pressure-temperature phase diagram of κ-(BEDT-TTF)$_2X$, κ-Br salt is shifted at high pressure side by BEDT-STF doping. The mechanism of T_c suppression by BEDT-STF doping has not been revealed by the resistivity measurement. The present NMR experiment unravels unambiguously the microscopic mechanism of T_c suppression.

In STF-10 sample, the local effect of quasiparticle scattering would be observed. At the doping concentration of 10 %, however, temperature dependence of $1/T_1$ in STF-10 is almost the same as that in TTF-9. Similar to the high-temperature magnetic susceptibility, superconducting properties are also uniformly affected by the impurities. The in-plane coherence length in κ-Br has been measured as approximately 30 Å[51, 25]. Whereas the mean distance between BEDT-STF impurities at $x = 10$ % is estimated as 17 Å from the in-plane lattice constants $a = 12.942$ Å, and $c = 8.539$ Å. These length scales indicate that 10 BEDT-STF molecules are located within the coherence volume. Therefore, a quasiparticle is scattered by several impurities within a coherence, and the impurity effect at the impurity site is averaged to result in a uniform quasiparticle state. A experiment on the sample with smaller doping concentration, in which one impurity exists in a coherence volume, is required to investigate the scattering effect by a single impurity.

5.1.4 Summary

We performed ^{13}C NMR measurements in pristine and BEDT-STF doped κ-Br . We observed the electronic states at near and far from the impurity site by utilizing the selectively ^{13}C enrichment BEDT-TTF or BEDT-STF molecules. BEDT-STF doping causes the decrease in the peak of $1/T_1T$ at 50 K, that is, the disturbance of the antiferromagnetic correlation. The result of the same temperature dependence of $1/T_1T$ at bulk and impurity sites indicates that magnetism of BEDT-STF doped κ-Br is homogeneous in the normal state. In the superconducting state, $1/T_1$ far below T_c is increased with BEDT-STF doping and proportional to temperature. These results show the increase in residual density of states at Fermi energy. Hence, the reduction of T_c is originated from the impurity effect. The temperature dependence of $1/T_1$ can be explained by introducing the residual density of states at Fermi energy into the d-wave quasiparticle density of states, which is a good evidence that κ-Br has d-wave superconducting gap. Temperature dependence of $1/T_1$ at the impurity site has also the same as that at bulk site. This result is assumed to be due to observing the averaged quasiparticles that is scattered by some BEDT-STF molecules within a coherence length.

5.2 Superconducting fluctuation

5.2.1 κ-(BEDT-TTF)$_2$Cu[N(CN)$_2$]Br

Figure 5.6 shows the temperature dependence of $1/T_1T$ for κ-Br salt in various magnetic fields. The temperature-independent Fermi liquid behavior as eq. (2.4) was observed below 20 K, which

confirms that the magnetic fluctuations near antiferromagnetic transition are sufficiently suppressed, and the Fermi liquid state is established when superconductivity sets in. The vertical dashed line in Fig. 5.6 denotes the mean-field $T_c = 10$ K, which was determined by the abrupt decrease in NMR shift at 0.75 T. (Right scale of Fig. 5.6(a)) When magnetic field of 8 T is applied perpendicular to the conduction plane $H_\perp$ (Fig. 5.6(a)), superconductivity is completely destroyed and Fermi liquid behavior persists down to 4.2 K. In smaller fields, $1/T_1T$ deviates from the Fermi liquid behavior below 14 K, which is higher than the mean-field $T_c = 10$ K. We suggest that the decrease in $1/T_1T$ above T_c is caused by the fluctuating superconducting order parameter.

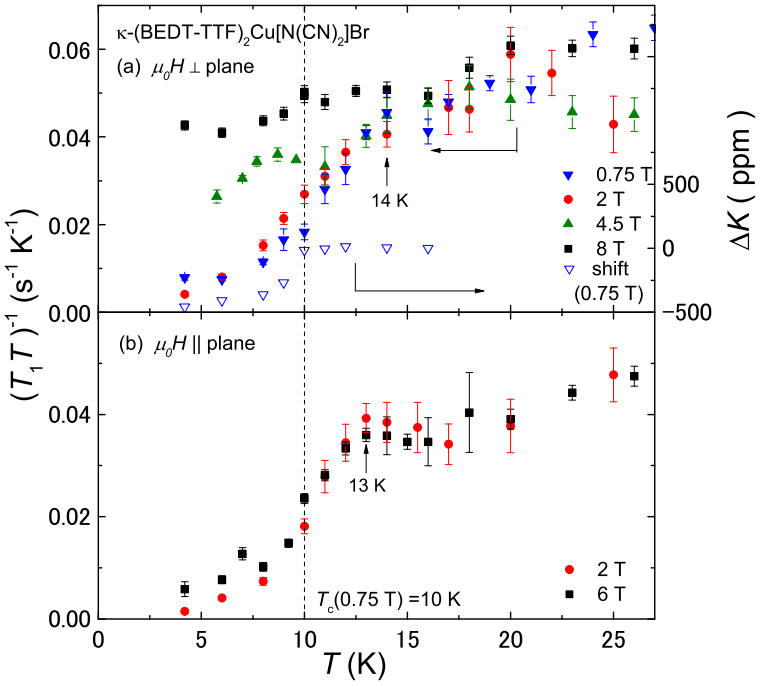

Figure 5.6: Temperature dependence of $1/T_1T$ for κ-Br salt in various magnetic fields perpendicular (a) and parallel (b) to the conduction plane. Open symbol shows the temperature dependence of NMR shift in 0.75 T. Dashed line denotes the mean-field $T_c = 10$ K, which was determined by the abrupt decrease in NMR shift. The reduction of $1/T_1T$ observed above T_c indicates that the fluctuating superconducting order parameter affects the quasi-particle density of states.

The reduction of $1/T_1T$ was also observed in the parallel magnetic field (Fig. 5.6(b)). As 8 T is not strong enough to suppress superconductivity and induce Fermi liquid behavior at low temperatures, the onset of $1/T_1T$ reduction was determined as the temperature at which $1/T_1T$ deviates from the high-temperature Fermi liquid behavior. The onset for $H_\perp$ (14 K) is slightly higher than that for $H_\parallel$ (13 K). This subtle difference is due to the anisotropy of coherence length. Since decrease in $1/T_1T$ at temperatures higher than T_c was observed in both $H_\perp$ and $H_\parallel$, we

conclude that κ-Br salt shows fluctuating superconducting state regardless of the magnetic field directions. Present results indicate that the density of states process is dominant in κ-Br salt compared to the Maki-Thompson process.

5.2.2 κ-(BEDT-TTF)$_2$Cu(NCS)$_2$

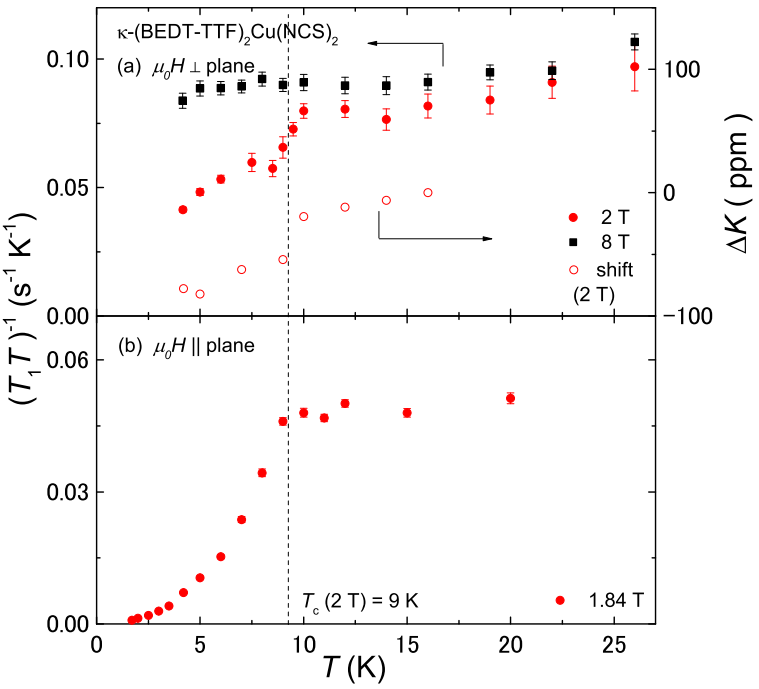

Figure 5.7: Temperature dependence of $1/T_1T$ for κ-NCS salt in magnetic fields perpendicular (a) and parallel (b) to the conduction plane. Open symbol shows the temperature dependence of NMR shift in 2 T, which determined the mean-field $T_c = 9$ K. Although T_c is comparable to that for κ-Br salt, κ-NCS salt shows the reduction of $1/T_1T$ above T_c only in the temperature range very close to T_c.

The same measurements were performed for κ-NCS salt, and the results were displayed in Fig. 5.7. The Fermi liquid behavior was observed at all temperature region in $H_\perp = 8$ T. At a small field, deviation of $1/T_1T$ from the Fermi liquid behavior starts almost at the mean-field $T_c = 9$ K. Similarly, in a parallel field, the decrease in $1/T_1T$ from the temperature-independent value was observed only below T_c. These results indicate that the temperature region, where superconducting fluctuations become significant, is limited very close to T_c in κ-NCS salt.

5.2.3 The difference of superconducting fluctuation in κ-(BEDT-TTF)$_2X$

Now, we compare the results of κ-Br and κ-NCS salts. Although superconducting transition occurs at comparable temperatures in both salts, the reduction of $1/T_1T$ due to the superconducting fluctuation was observed only in κ-Br salt, in consistent with Nernst effect and magnetization measurements [46, 52]. The superconducting parameters for κ-Br and κ-NCS salts should be compared to understand the universal behavior of fluctuating superconducting state.

In the critical regime above T_c, the short-range superconducting coherence can be observed when the thermal energy becomes comparable to the energy cost required to induce superconducting gap within the Pippard length ξ. Therefore, the critical temperature range is determined by the superconducting gap size Δ, T_c, and ξ, as

$$\frac{|T - T_c|}{T_c} \propto \left(\frac{k_B T_c}{\xi_{\parallel}^2 \xi_{\perp} \Delta} \right)^2 \equiv G, \tag{5.4}$$

where $\xi_{\parallel}$ and $\xi_{\perp}$ are the in-plane and inter-plane Pippard length. The typical temperature range for a three-dimensional BCS superconductor is as narrow as $G \sim 10^{-6}$. Wider critical regime is expected for low dimensional superconductors with short $\xi_{\perp}$. Our experimental results suggest that G of κ-Br salt reaches to the order of 10^{-1}, which is comparable to the results obtained for high-T_c cuprate.

We estimated the ratio $2\Delta/k_BT_c$ from the temperature dependence of $1/T_1$ in the superconducting state. Figure 5.8 shows the temperature dependence of $1/T_1$ normalized at T_c for κ-Br and κ-NCS salts. The power-law temperature dependence suggests that d-wave superconductivity with nodes on superconducting gap is realized in both κ-Br and κ-NCS salts. The fit to the temperature dependence with the theoretical curve for d-wave superconductivity gives the estimation of $2\Delta/k_BT_c$, which are 7 for κ-Br salt and 5 for κ-NCS salt. The ratio between κ-Br and κ-NCS salts is in perfect agreement with the values reported in the literature [25]. We note that the large Δ for κ-Br salt seems to reduce critical temperature regime defined in eq. (5.4). However, because the Pippard length is also related to Δ as $\xi = \hbar v_F/\pi\Delta$, the larger Δ increases the critical regime by reducing the coherence length. Here we assumed that only the coherence length in the conduction plane $\xi_{\parallel}$ is determined by Δ because of the two-dimensional nature of superconductivity in κ salts. In fact, $\xi_{\parallel}$ for κ-Br salt (3.7 nm) is twice shorter than that for κ-NCS salt (7.0 nm), whereas $\xi_{\perp}$ is almost comparable between κ-Br and κ-NCS salts [25].

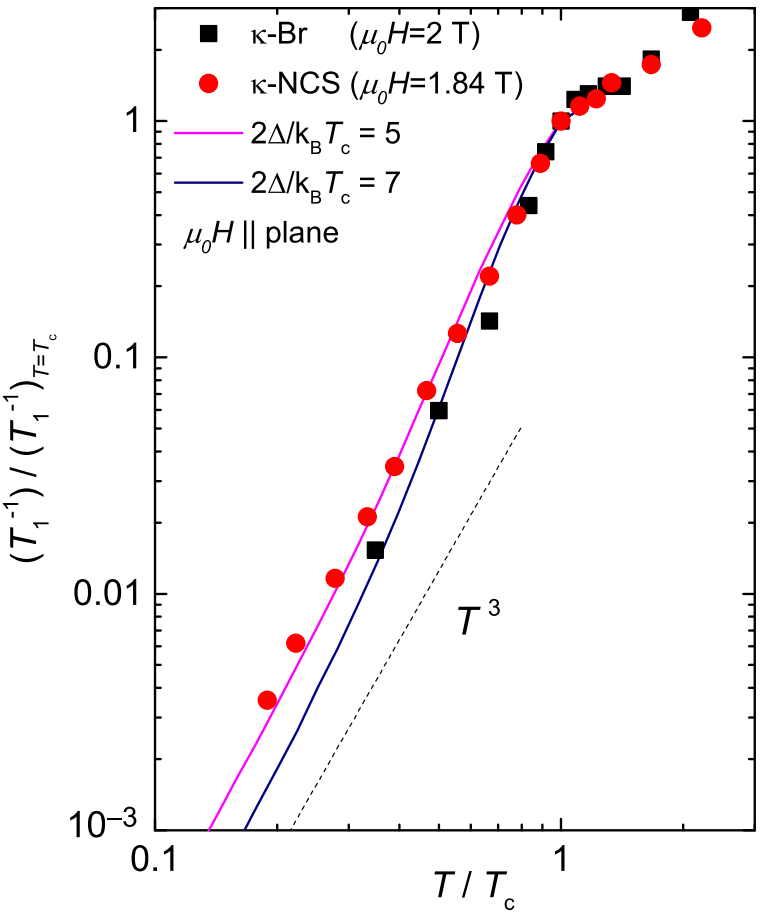

Figure 5.8: superconducting parameter $2\Delta/k_BT_c$ estimated from the temperature dependence of $1/T_1$ in the superconducting state. The vertical axis is $1/T_1$ scaled by the value at T_c, and the horizontal axis is the reduced temperature T/T_c. We estimated $2\Delta/k_BT_c$ by fitting the experimental data to the theoretical curve for the d-wave superconductor.

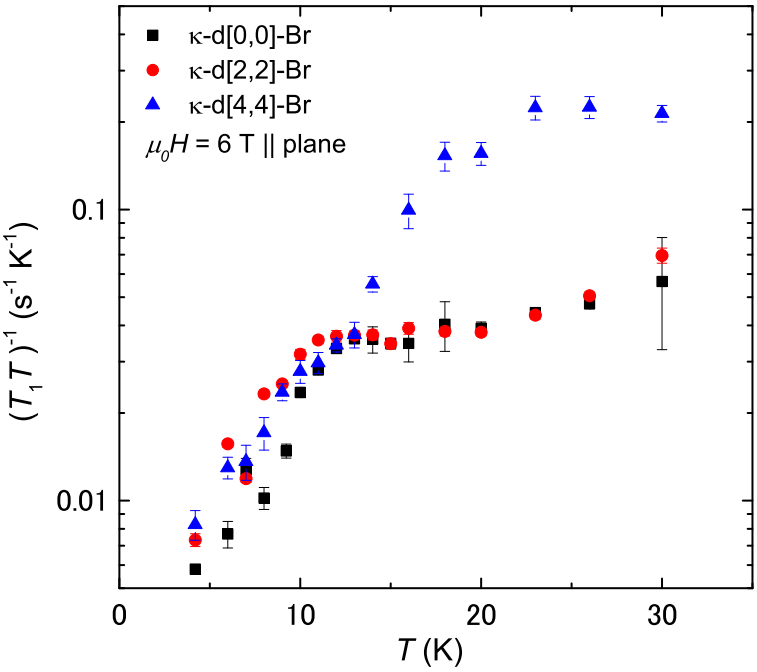

Figure 5.9: Deuteration effect on the Fermi liquid state near T_c. Strong temperature dependence due to the reduction of $(1/T_1T)_{\mathrm{AF}}$ term was observed in κ-$d[4,4]$-Br salt, while κ-$d[0,0]$-Br and κ-$d[2,2]$-Br salts show the Fermi liquid behavior below 20 K. In κ-$d[4,4]$-Br, the effects of the superconducting fluctuation was contaminated by the strong magnetic fluctuations near the antiferromagnetic phase transition.

5.2.4 Deuteration effect of κ-(BEDT-TTF)$_2$Cu[N(CN)$_2$]Br

The larger Δ is expected for the deuterated κ-$d[4,4]$-Br salt, which locates very close to the antiferromagnetic phase. Previous NMR study for κ-$d[4,4]$-Br salt suggested a possibility that the critical superconducting regime starts from rather high temperatures [62]. We also measured $1/T_1T$ near T_c for κ-$d[4,4]$-Br salts with $n = 0, 2, 4$ applying the magnetic field of 6 T along the c direction. In Fig. 5.9, a strong temperature dependence of $1/T_1T$ was observed around 20 K in κ-$d[4,4]$-Br salt in consistent with previous report [62]. This behavior cannot be directly interpreted as the effect of fluctuating superconducting order parameter, because enhanced magnetic fluctuations contaminate the pure effect of superconducting fluctuations. The strong temperature dependence observed in κ-$d[4,4]$-Br salt indicates that the $(1/T_1T)_{\rm AF}$ term remains dominant until low temperatures. The increase in $1/T_1T$ by enhanced magnetic fluctuations was observed only above 30 K in κ-$d[2,2]$-Br and κ-$d[1,1]$-Br salts. This $(1/T_1T)_{\rm AF}$ term is suppressed below 20 K, and the Fermi liquid state is stabilized at T_c in these salts. The comparable constant value of $1/T_1T = 0.035$ s^{-1}K^{-1} indicates that the deuteration does not significantly modify the $(1/T_1T)_{\rm FL}$ term. We suggest, from the deuteration independent behavior of $1/T_1T$ below 14 K, that κ-$d[4,4]$-Br salt also shows the reduction of $(1/T_1T)_{\rm FL}$ term due to superconducting fluctuation near T_c, although details were hindered by the $(1/T_1T)_{\rm AF}$ term.

5.2.5 Summary

In summary, we observed the reduction of $1/T_1T$ starting above T_c in κ-Br salt in fields both parallel and perpendicular to the conduction plane, and addressed the fluctuating superconducting order parameter as the origin of this reduction. The microscopic NMR experiment enabled the direct observation of quasi-particle density of states in the fluctuating superconducting state. We revealed that, in the fluctuating superconducting state in κ-Br salt, the quasi-particle density of states is reduced from the normal-state value because of the dominant density of states process. In κ-NCS salt, the reduction of quasi-particle density of states due to superconducting fluctuation was observed only in the temperature range very close to T_c. Our systematic study clarified the field-orientation dependence of the superconducting fluctuation and convinced that the superconducting fluctuation has larger effect on $1/T_1T$ in κ-Br salt than that in κ-NCS salt. From the estimation of superconducting gap size for κ-Br and κ-NCS salts, we suggest that the small critical regime in κ-NCS salt is due to the long coherence length. We also measured $1/T_1T$ in the deuterated κ-$d[n,n]$-Br salts, and found that the deuteration induces the large $(1/T_1T)_{\rm AF}$ term even at T_c, which contaminates the pure effect of superconducting fluctuation. These results indicate that

κ-$d[0,0]$-Br salt is an ideal system to study pure effect of superconducting fluctuation, and provide microscopic information to understand the electronic properties in the fluctuating superconducting state.

Part II

^{13}C NMR Studies of Magnetic Fluctuations in λ-$(BETS)_2GaCl_4$

Chapter 6

Introduction

6.1 Basic properties of λ-$(BETS)_2GaCl_4$

6.1.1 Crystal structure

As shown in Fig. 6.1(a), λ-$(BETS)_2GaCl_4$ salt has quasi-two-dimensional structure, consisting of conducting layers of BETS molecules and insulating layers of $GaCl_4$. In the conduction plane, BETS molecules are arranged as λ-modification, in which all molecules are oriented parallel to each other and two BETS molecules form a dimer. As a result, this salt possesses the half-filled electron system as well as κ-$(BEDT\text{-}TTF)_2X$. Band structure reflects the dimerization, that is, there is a splitting between bonding and anti-bonding orbitals as shown in Fig. 6.2. Although the arrangement of λ-modification is completely different from that of κ-modification, the shape of the Fermi surface is similar to each other.

6.1.2 Physical properties

Figure 6.3 show the temperature dependence of the resistivity of λ-$(BETS)_2GaCl_4$ salt [64]. Resistivity shows a semiconducting behavior at room temperature and a broad hump at 100 K. Below 100 K, system becomes metallic and then superconducting transition was observed at 6 K. Susceptibility measurement shows consisting result as shown in Fig. 6.4. Although the susceptibility slightly increases with decreasing temperature, the result can be understood as the Pauli paramagnetic behavior down to T_c.

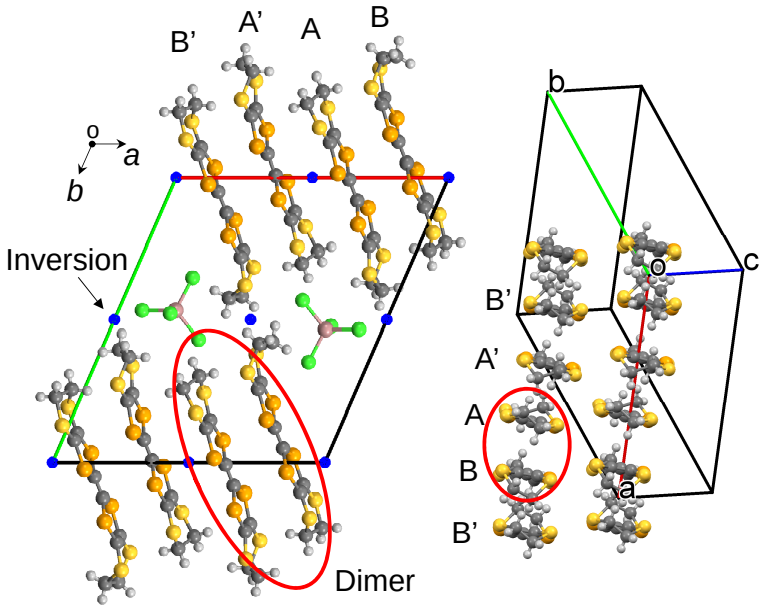

Figure 6.1: Crystal structure of λ-$(BETS)_2GaCl_4$ salt.

6.1.3 Superconductivity

Recently, superconducting properties of λ-$(BETS)_2GaCl_4$ salt have been extensively studied. Near the upper critical field, hints of the presence of a Fulde–Ferrell–Larkin–Ovchinnikov phase have been found in several experiments [64, 67, 68]. Thermodynamic properties were measured in the superconducting state under various magnetic fields as shown in Fig. 6.5 [66]. Electronic specific heat is proportional to T^2 at zero field far below T_c and shows linear temperature dependence with increasing magnetic fields, suggesting the d-wave superconducting gap symmetry. The anisotropy of the superconducting gap has been also studied by other probes (Table 6.1) but its symmetry has not been determined completely. To investigate the properties of superconductivity, NMR experiments can provide the information of superconducting gap symmetry microscopically. Hence, we performed the NMR measurements of λ-$(BETS)_2GaCl_4$ salt in the superconducting state.

Table 6.1: Experimental investigation of superconducting gap symmetry in λ-$(BETS)_2GaCl_4$.

Experiment	Symmetry	Ref.
Microwave conductivity	s-wave	[69]
STM	d-wave	[70]
Specific heat	d-wave	[66]
μSR	s- or d-wave ?	[71]

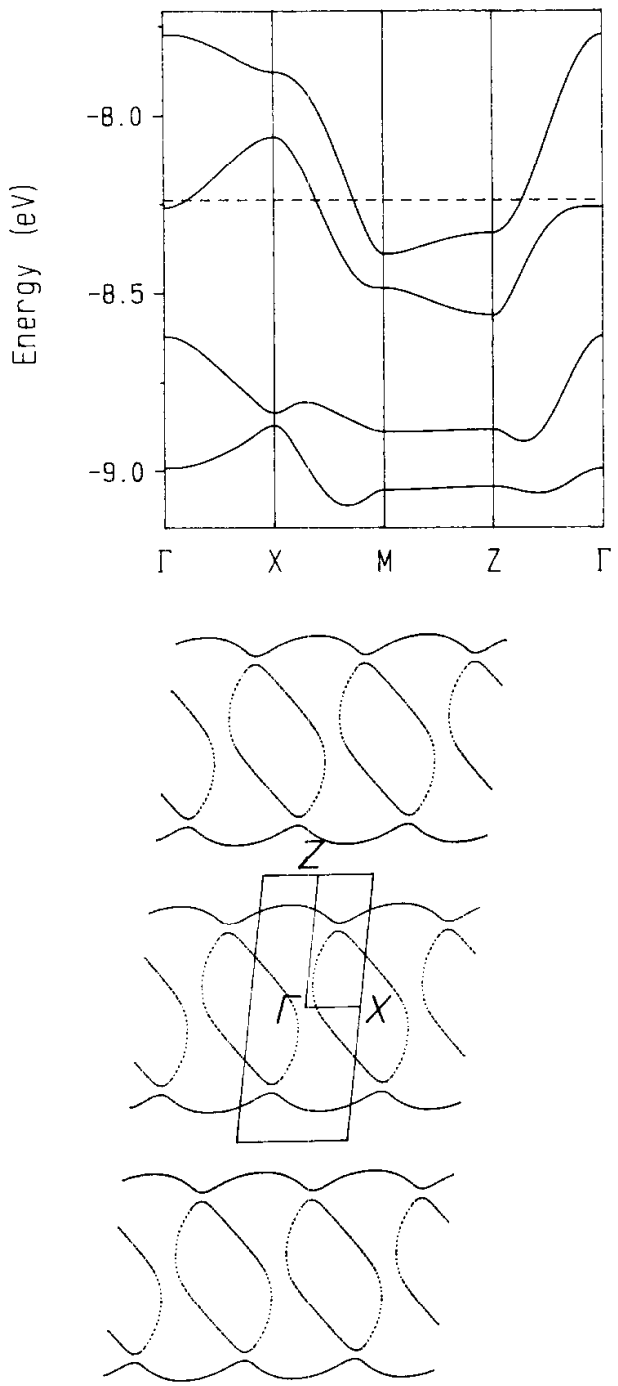

Figure 6.2: Energy band structure and Fermi surface [63].

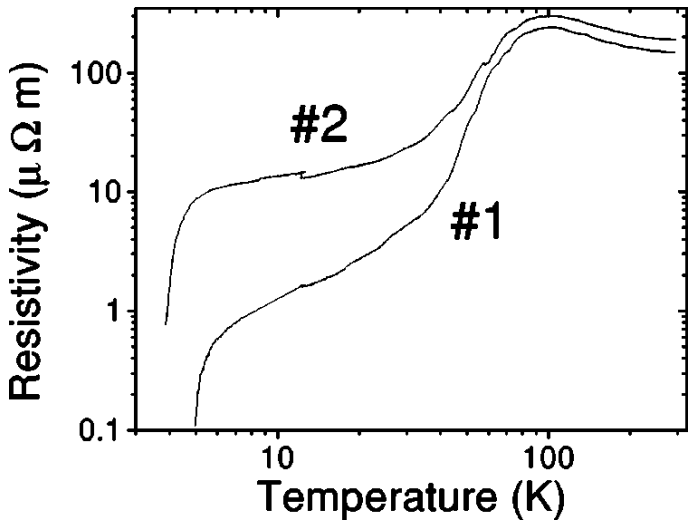

Figure 6.3: Temperature dependence of resistivity in λ-$(BETS)_2GaCl_4$ salt [64].

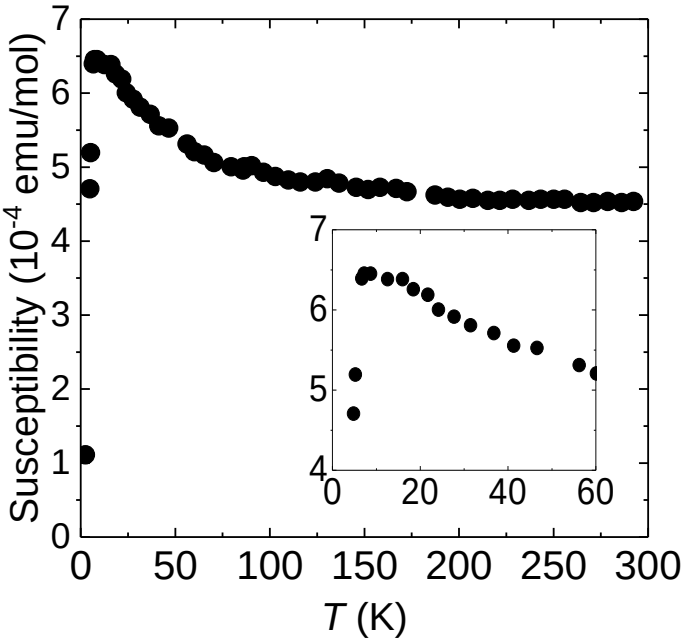

Figure 6.4: Temperature dependence of susceptibility in λ-$(BETS)_2GaCl_4$ salt cited from Ref. [65].

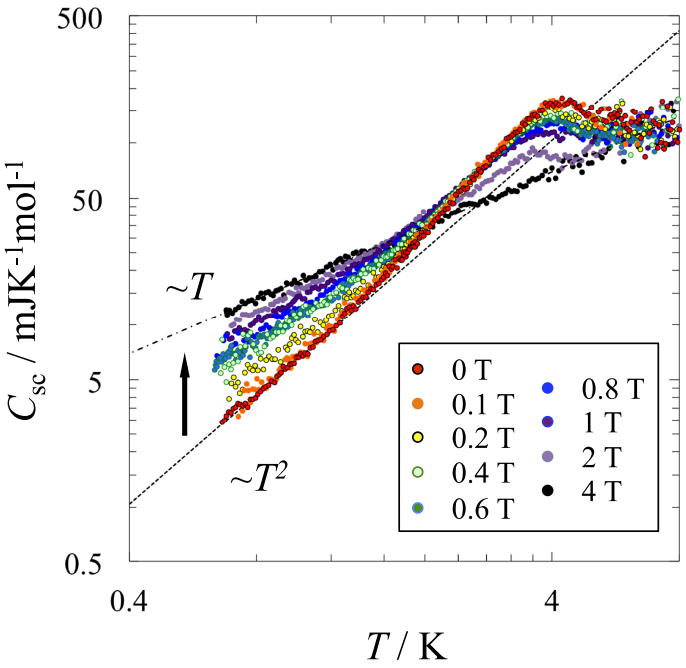

Figure 6.5: Temperature dependence of specific heat at several magnetic fields [66].

6.2 Phase diagram study of λ-modification

6.2.1 Donor substitution

To reveal the mechanism of superconductivity in λ-$(BETS)_2GaCl_4$ salt, the electronic phase near the superconducting state should be investigated. In spite of extensive studies for the superconductivity, the pressure–temperature (P–T) phase diagram has not been established in the λ-modification in contrast to the well-known κ-modification [19]. To investigate the P–T phase diagram of the λ-modification, a preliminary study was conducted wherein the bandwidth was controlled by changing the donor in a series of λ-D_2GaCl_4 (D= BEDT-TTF, BEDT-STF, BETS) salts [72]. As shown in Fig. 6.6, the λ-$(BEDT\text{-}TTF)_2GaCl_4$ and λ-$(BEDT\text{-}STF)_2GaCl_4$ salts are insulators whereas the λ-$(BETS)_2GaCl_4$ salt is metallic at ambient pressure. Resistivity measurements taken of the λ-D_2GaCl_4 salts under pressure revealed that the substitution effect of BEDT-TTF, BEDT-STF, and BETS molecules can be understood in terms of chemical pressure, but in their report, superconductivity of λ-$(BEDT\text{-}STF)_2GaCl_4$ salt under pressure was not observed. Recently, a superconducting phase transition was observed in the λ-$(STF)_2GaCl_4$ salt above 1.22 GPa [73] (Fig. 6.7). Authors suggested that no indication of superconductivity in the previous experiment is considered as due to the sample quality.

Regarding the magnetic properties, the ESR measurement for λ-$(BEDT\text{-}TTF)_2GaCl_4$ salt suggests an antiferromagnetic phase transition at $T_N = 13$ K [72]. Recently, ^{13}C NMR measurements

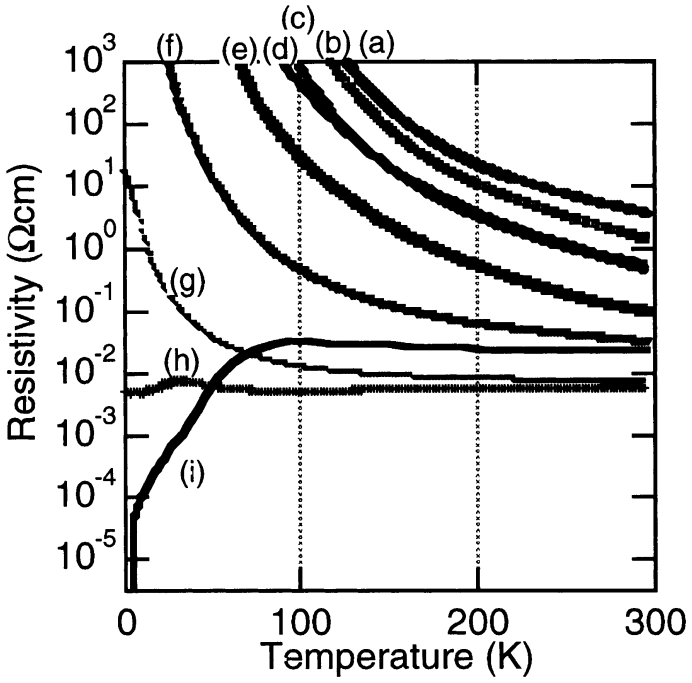

Figure 6.6: Temperature dependence of resistivity for λ-D_2GaCl_4 under applying pressures [72]. Applying pressures are (a) ambient pressure, (b) 0.45, (c) 1.65 GPa in λ-(BEDT-TTF)$_2$GaCl$_4$ salt, (d) ambient pressure, (e) 0.45, (f) 1.35, (g) 1.73, (h) 1.8 GPa in λ-(BEDT-STF)$_2$GaCl$_4$ salt, and (i) ambient pressure in λ-(BETS)$_2$GaCl$_4$ salt.

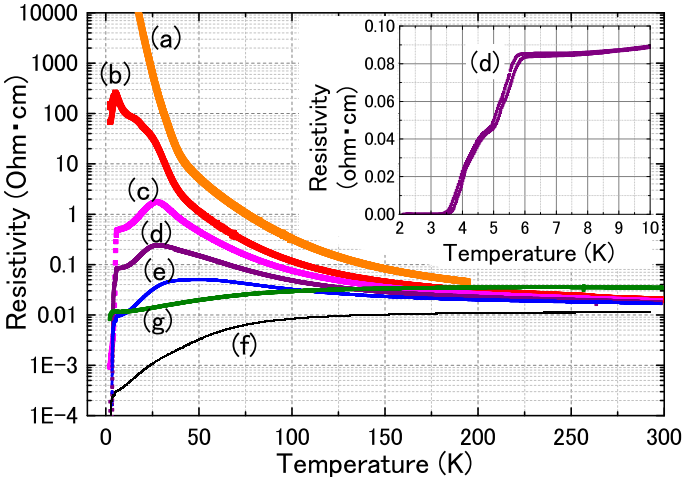

Figure 6.7: Temperature dependence of the resistivity in λ-STF$_2$GaCl$_4$ at several pressures [73]. Applying pressures are (a) 1.10, (b) 1.22, (c) 1.27, (d) 1.31, (e) 1.35, (f) 1.60, and (g) 1.90 GPa. (a) to (f) and (g) were obtained for the different samples.

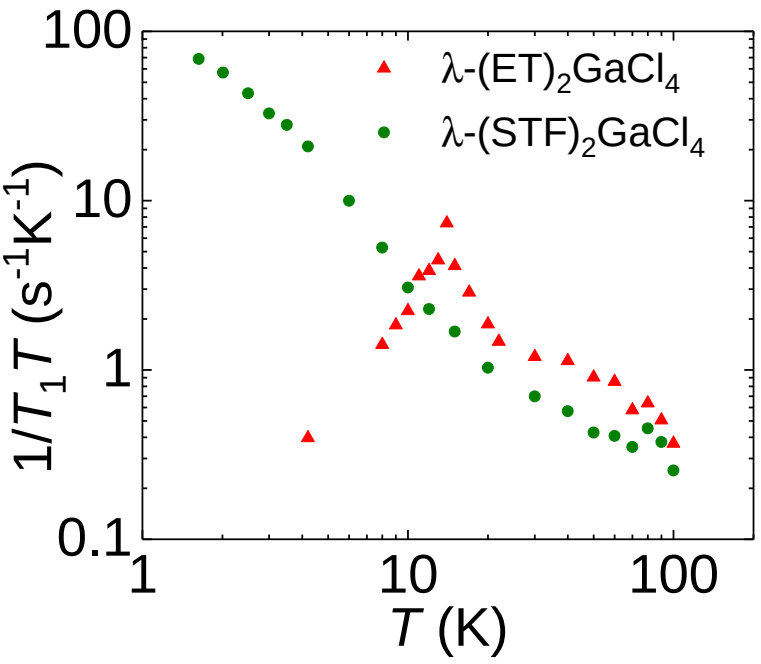

Figure 6.8: Temperature dependence of $1/T_1T$ in λ-(BEDT-TTF)$_2$GaCl$_4$ and λ-(BEDT-STF)$_2$GaCl$_4$ salts using ^{13}C NMR.

were performed in λ-(BEDT-TTF)$_2$GaCl$_4$ and λ-(BEDT-STF)$_2$GaCl$_4$ salts [74, 75]. Figure 6.8 shows the temperature dependence of $1/T_1T$ in the λ-(BEDT-TTF)$_2$GaCl$_4$ (triangles) and λ-(BEDT-STF)$_2$GaCl$_4$ (circles) salts. In λ-(BEDT-TTF)$_2$GaCl$_4$ salt, a divergent peak of $1/T_1T$ and discrete NMR line splitting were observed at 13 K, suggesting the commensurate antiferromagnetic phase. On the other hand, $1/T_1T$ of λ-(BEDT-STF)$_2$GaCl$_4$ salt increases with decreasing temperature down to the lowest temperature, which indicates the development of antiferromagnetic fluctuation. Magnetic susceptibility measurement also suggested that no magnetic transition [73]. From these results, we can obtain a P–T phase diagram (Fig. 6.9) that plots the $T_{\rm N}$, T_c, and semiconductor–metal crossover temperature $T_{\rm MI}$ cited from Ref. [65, 72, 73]. The positions of each salt in terms of pressure were estimated by comparing trends in the resistivity and the pressure dependence of T_c. From the P–T phase diagram, it is interesting to examine the effect of the antiferromagnetic phase on the electronic state at high pressure region.

6.2.2 Anion substitution

On the other hand, physical properties in a series of λ-(BETS)$_2$GaBr$_x$Cl$_{4-x}$ ($0 \leq x \leq 2.0$) have been investigated [65]. Figure 6.10 shows the temperature dependence of resistivity in λ-(BETS)$_2$GaBr$_x$Cl$_{4-x}$ ($0 < x < 1.50$) salts. With increasing the bromine content, the T_c increases

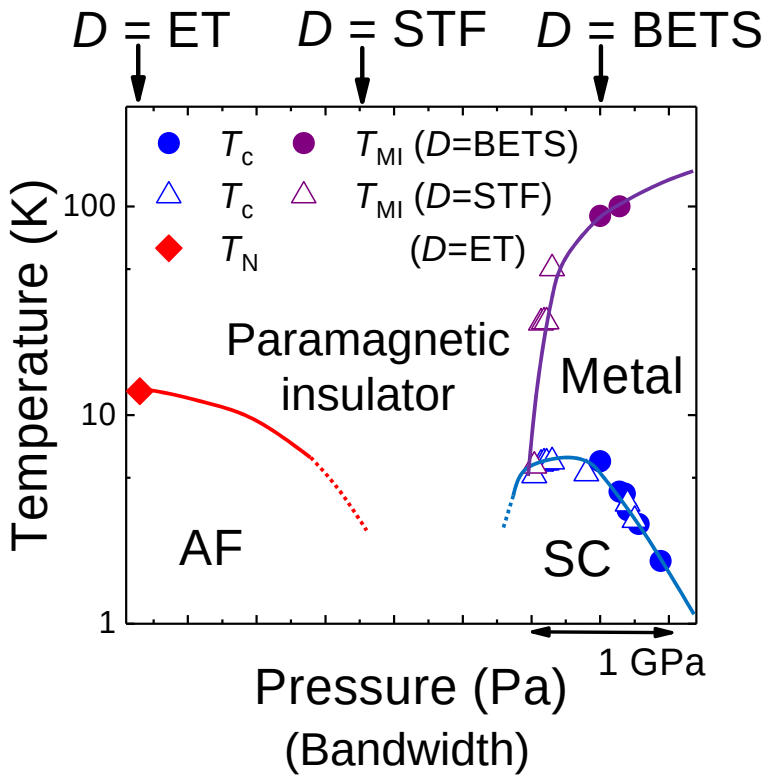

Figure 6.9: Pressure–temperature phase diagram of λ-D_2GaCl_4 [72].

up to $x = 0.69$, and then superconductivity is suppressed. The metal–insulator crossover temperature around 100 K in $x = 0$ is decreased with increasing x and finally the sample of $x = 1.5$ shows the insulating behavior in the entire temperature range.

Magnetic susceptibility has also been studied between $0 \leq x \leq 1.3$ as shown in Fig. 6.11. When x is 1.3, susceptibility is depressed below 25 K and no anisotropy was observed. Therefore, author suggests that the phase adjacent to the superconducting phase of λ-$(BETS)_2GaCl_4$ salt is nonmagnetic insulating phase.

6.3 Previous NMR studies of λ-$(BETS)_2GaCl_4$

The effect of these electronic phases to the electronic state of λ-$(BETS)_2GaCl_4$ salt is of great interest to consider the mechanism of superconductivity. In order to study the effect of them, NMR spectroscopy is one of the best probes because the local spin susceptibility and magnetic fluctuations can be observed through the Knight shift and the nuclear spin-lattice relaxation time T_1 measurements, respectively. So far, ^{77}Se NMR measurement have been performed. Figure 6.13 shows the temperature dependence of $1/T_1T$ for ^{77}Se NMR using single crystal in the metallic state [76]. $1/T_1T$ shows constant down to 10 K suggesting the Fermi liquid state, and then increases

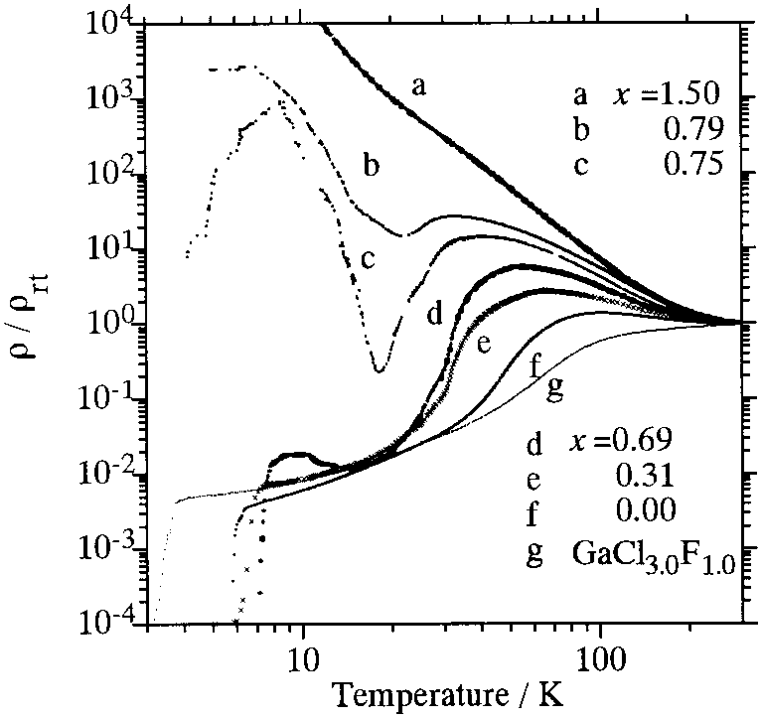

Figure 6.10: Temperature dependence of resistivity in λ-$(BETS)_2GaBr_xCl_{4-x}$ ($0 \leq x \leq 2.0$) and λ-$(BETS)_2GaCl_3F_1$ [65].

below 10 K. Authors suggested that antiferromagnetic fluctuation. However, the linewidths of ^{77}Se NMR using randomly oriented samples and single crystal samples show the different behaviors at low temperatures [76, 77].

^{1}H NMR measurement have also been performed, but the result is quite different from that of ^{77}Se NMR measurement. Because the ^{1}H site of ethylene group of BETS molecules weakly couples with the electron system, the mechanism of relaxation process can be originated other than the electronic system. Therefore, ^{1}H site is not suited to study the electronic state of BETS systems. The contradictions arise from experimental difficulties with low sensitivity and broad linewidths in ^{77}Se NMR signal and the additional relaxation mechanism from molecular motions due to weak coupling of the ^{1}H nuclei with the π conducting electrons.

Therefore, measurements from the well-established ^{13}C nuclei are desirable [78]. In this study, we performed these ^{13}C NMR measurements by synthesizing ^{13}C-enriched BETS molecules in which one side of the central C=C bond is replaced by ^{13}C. By using the ^{13}C-enriched sample, we can overcome the difficulties of previous NMR studies because the ^{13}C sites exhibit a sharp spectral response, high sensitivity, and large electron density at the nucleus. Hence, we can reveal the magnetic properties of λ-$(BETS)_2GaCl_4$ salt more clearly.

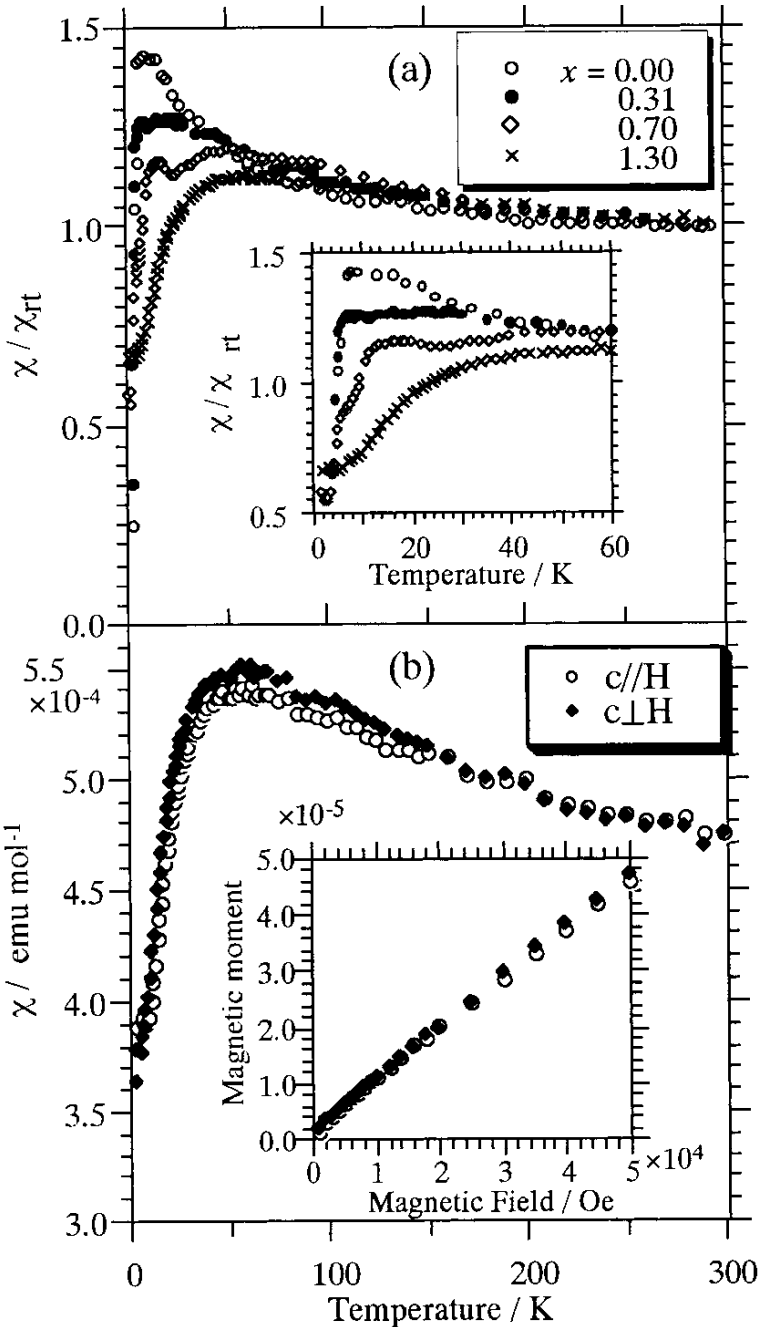

Figure 6.11: (a)Temperature dependence of magnetic susceptibility in λ-$(BETS)_2GaBr_xCl_{4-x}$ ($0 \leq x \leq 2.0$). (b) Temperature dependence of magnetic susceptibility in λ-$(BETS)_2GaBr_{1.3}Cl_{2.7}$ under the magnetic field parallel and perpendicular to the c-axis [65].

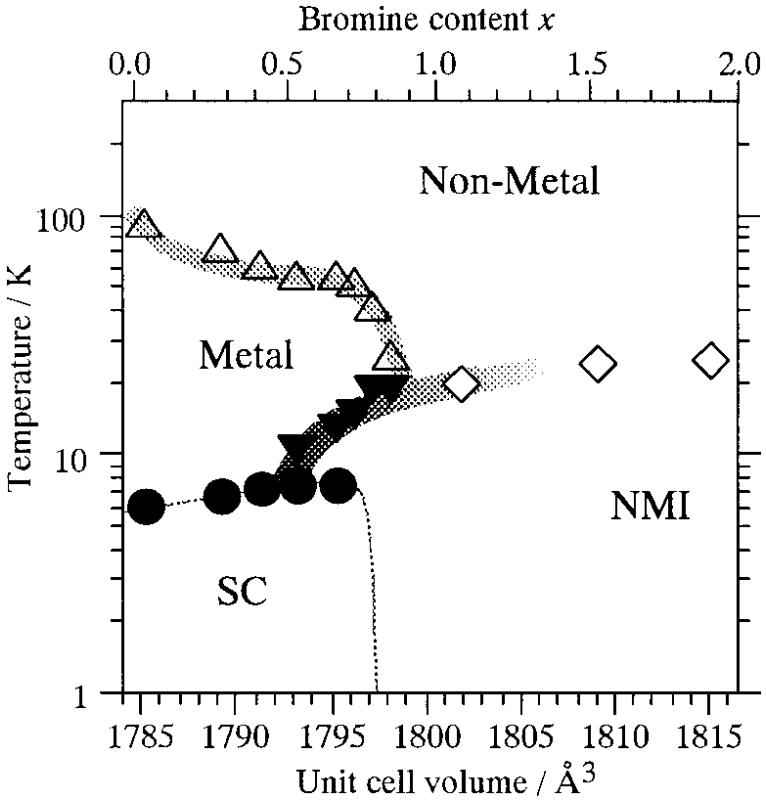

Figure 6.12: Phase diagram of λ-$(BETS)_2GaBr_xCl_{4-x}$. Horizontal and vertical axis corresponds to the cell volume and temperature, respectively. SC and NMI represents the superconductor and nonmagnetic insulator [65].

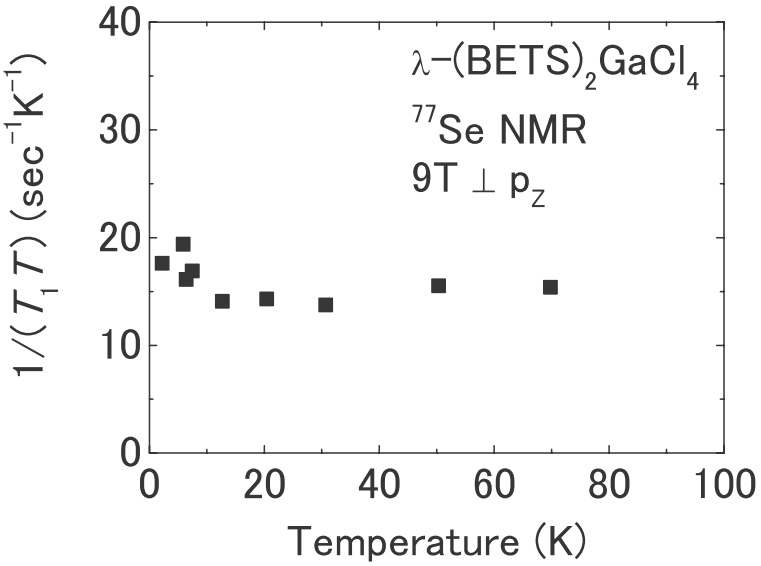

Figure 6.13: Temperature dependence of $1/T_1T$ in ^{77}Se NMR [76].

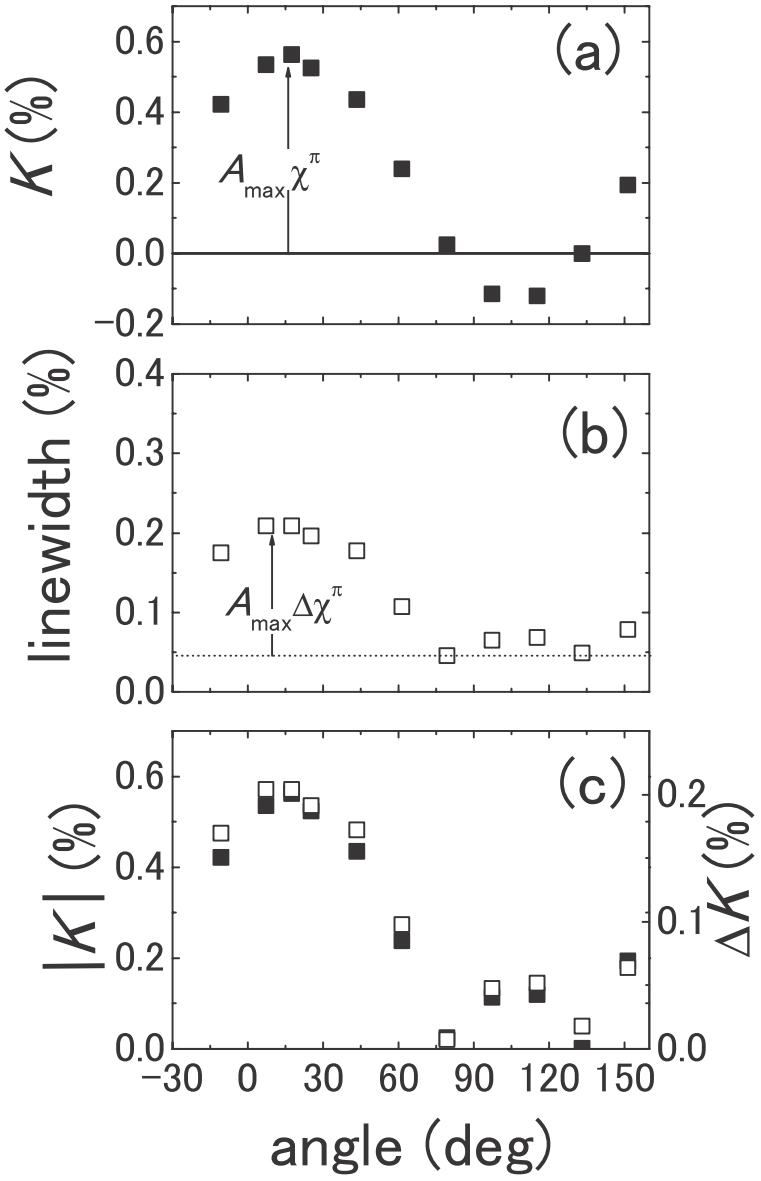

Figure 6.14: Angle dependence of (a) Knight shift, (b)linewidth. (c) Left and right axes indicate the absolute value of Knight shift and $\Delta K = \sqrt{\text{width}^2 - \text{width}^2_{min}}$ [76].

6.4 Motivation of the study

Because several insulating phases have been proposed as the adjacent phase of λ-$(BETS)_2GaCl_4$ salt, we investigated the effect of them to the paramagnetic state of λ-$(BETS)_2GaCl_4$ salt by ^{13}C NMR measurement. Furthermore, we studied the symmetry of superconducting gap through the ^{13}C NMR measurement in the superconducting state to discuss the effect of adjacent electronic phase on the superconductivity.

Chapter 7

Experiments

7.1 Sample preparation

We prepared λ-$(BETS)_2GaCl_4$ salt using ^{13}C enriched BETS molecules. BETS molecules were prepared in accordance with the prescription given in Ref. [79]. At the last step of the synthesis of BETS molecules, 15 % of ^{13}C-enriched ketone (**1**) and 85 % of naturally abundant ketone (**2**) were mixed (Fig. 7.1). Thereby we obtained 72 % of C=C molecules (**3**), which is NMR inactive, 26 % of ^{13}C=C molecules (**4**), and 2 % of ^{13}C=^{13}C molecules (**5**). This coupling ratio statistically reduces the products of ^{13}C=^{13}C molecules, which cause contamination of the NMR spectrum through the Pake doublet effect [56]. We determined the actual ratio by mass spectroscopy as 72 % of C=C molecules, 28 % of ^{13}C=C molecules, and the trace amount of ^{13}C=^{13}C molecules. Single crystals of the λ-$(BETS)_2GaCl_4$ salt were grown by the electrochemical oxidation method [80]. The typical size of the sample used in NMR measurements is $6.0 \times 0.28 \times 0.23$ mm^3. A T_c of 5.8 K was confirmed from the increase in the resonance frequency of the NMR coil at zero magnetic field as shown in Fig. 7.2.

7.2 NMR measurement

The NMR experiment in the paramagnetic state was conducted in a magnetic field of 6.5 T. We measured the magnetic field angle dependence of NMR spectra in the a^*b^*-plane. The orientation of the magnetic field $\theta = 0°$ corresponds to the magnetic field parallel to the conducting plane. Temperature dependence of NMR spectra was measured at $\theta = -16°$ where the peak separation of each site becomes the largest to determine the NMR shift precisely. This field direction is perpendicular to the molecular plane. The nuclear spin-lattice relaxation time T_1 was measured at the same condition, but we could obtain the reliable data only at low temperatures because

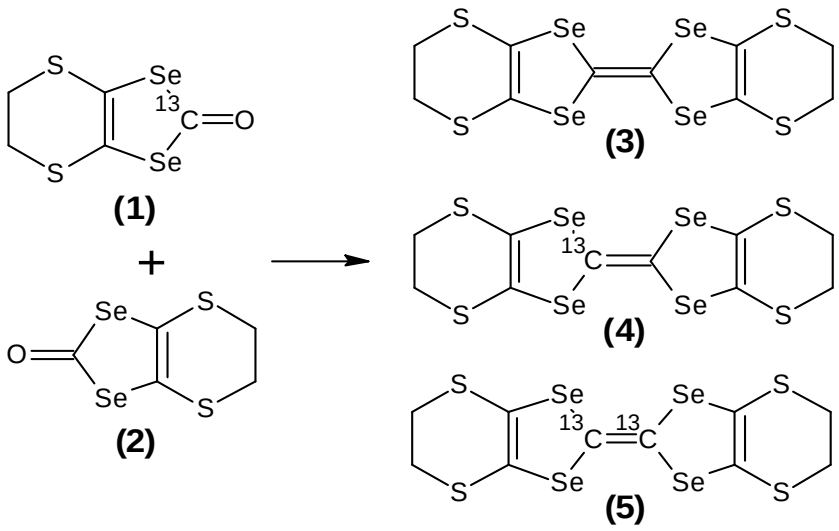

Figure 7.1: Preparation of ^{13}C-enriched BETS molecules.

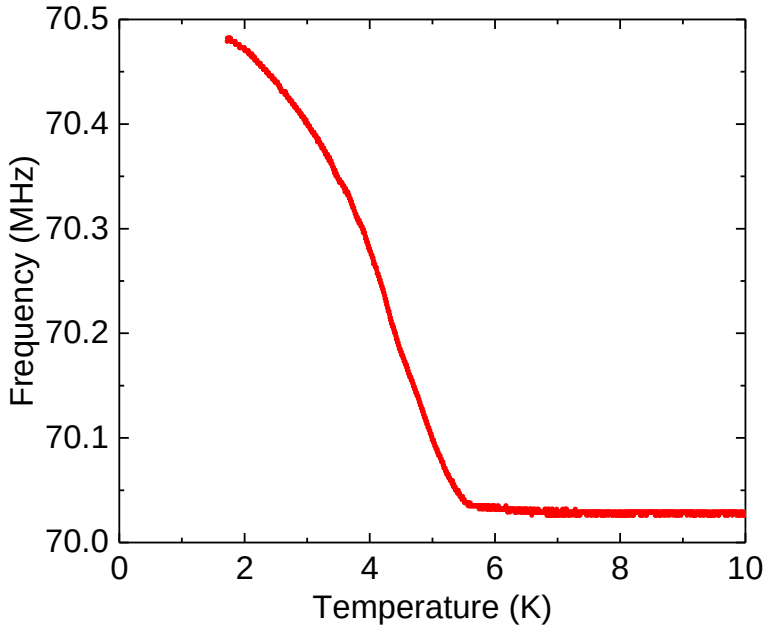

Figure 7.2: Temperature dependence of resonant frequency of the NMR coil observing the Meissner effect.

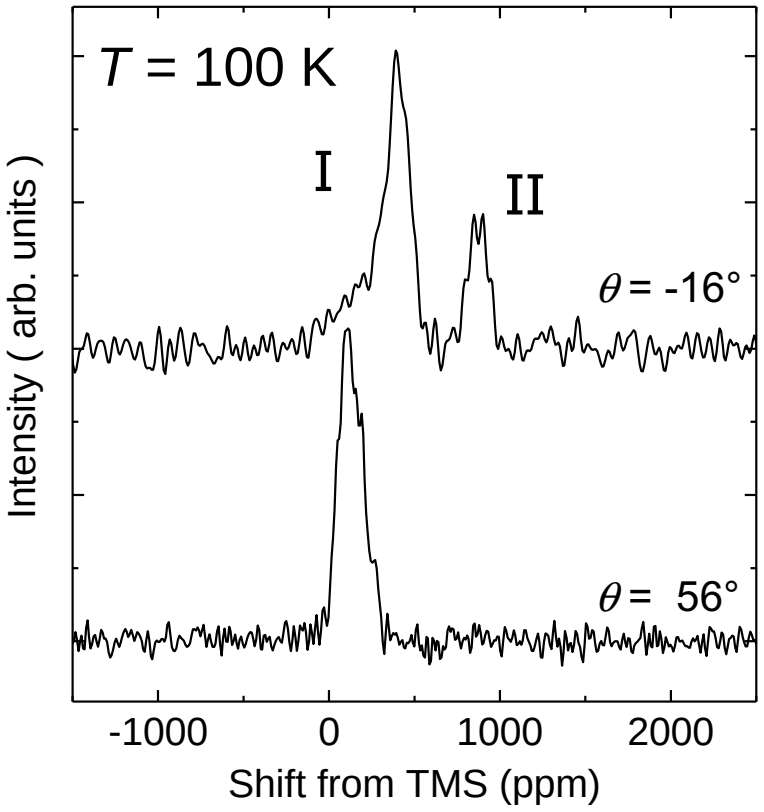

Figure 7.3: NMR spectra at the field direction of $\theta = -16^\circ$ and 56° at 100 K.

of long T_1. Therefore, the entire temperature dependence of T_1 was measured at $\theta = 56^\circ$ where T_1 becomes shortest and all peaks are superposed. This field direction enables to obtain the high quality T_1 data due to the high intensity of the signal and short T_1. In these field directions, the upper critical field at 1.5 K is substantially lower than 6.5 T, so that the superconducting state was completely suppressed in the study of the paramagnetic state. In the NMR experiment of superconducting state, magnetic fields of 2.5 T and 6.5 T were applied parallel to the conduction plane precisely ($\theta = 0^\circ$), in which the upper critical field becomes the largest as $\sim$ 10 T [64, 67, 68].

The NMR spectra were acquired by fast Fourier transformation of the echo signal with a $\pi/2$-π pulse sequence. Typical $\pi/2$ pulse lengths were 2 μs. The NMR shifts with respect to the reference material of tetramethylsilane (TMS) and linewidths (full widths at half maximum) were evaluated by fitting the peaks to Lorentzian fitting functions. T_1 measurements were performed by the conventional saturation-recovery method.

In the λ-$(BETS)_2GaCl_4$ salt, there are two crystallographically nonequivalent molecules A and B, which have respectively equivalent molecules A$'$ and B$'$ related by inversion symmetry in a unit cell (Fig. 6.1). One BETS molecule has two crystallographically independent ^{13}C sites, so that four peaks can be expected in the NMR spectrum. Actually, we observed at most two peaks I

and II (Fig. 7.3) at $\theta = -16$. We deduce that the ratio of intensities of peaks I and II is about $3:1$. Therefore peak I is composed of three sites. Note that a shoulder structure in the left peak can be seen. This can be understood as a consequence of the superposition of the three sites. T_1 were estimated for peak I at $\theta = -16^\circ$ and for observed single peak at 56°. The single peak at 56° is due to the superposition of four ^{13}C sites. Because each ^{13}C site has different hyperfine coupling constant, the recovery profile deviates from the single exponential function. To correct this deviation, we used a stretched exponential function,

$$\frac{M_0 - M(t)}{M_0} = \exp\left(-\left(t/T_1\right)^{\beta}\right). \tag{7.1}$$

Here, $M(t)$ and M_0 are the nuclear magnetizations at t and at thermal equilibrium, and β is the stretching exponent. The recovery profiles could be fitted with β of 0.8 for all temperatures.

Chapter 8

Results

8.1 Paramagnetic state

8.1.1 NMR shift and linewidth

Figure 8.1 shows the temperature dependence of the NMR spectra. The NMR shift of peak I significantly depends on the temperature rather than that of peak II due to the difference of the hyperfine coupling constant. The temperature dependence of the NMR shift is shown in Fig. 8.3. As discussed in 2.1, the NMR shift δ^i can be written as $\delta^i = K^i + \sigma = A^i\chi_s + \sigma$ (i identifies results related to peaks I and II). To assess quantitatively the degree of spin susceptibility, we evaluated the A^i and σ by δ^i–χ plot (Fig. 8.2). We assume the same chemical shift for peaks I and II because the chemical shift is insensitive to the difference between A and B molecules and to the position of the central ^{13}C sites [81]. Spin susceptibility data are cited from Ref. [65]. In consequence, A^{I} for peak I is 2.61 kOe/μ_B, A^{II} for peak II is 8.55 kOe/μ_B, and σ is 149 ppm. The σ of 149 ppm is comparable to that of BEDT-TTF molecules [78].

The Knight shift of each spectra is also shown in Fig. 8.3 with the corresponding scale given to the right. The Knight shift weakly increases with decreasing temperature and shows peak behavior at 20 K. With a further decrease in temperature, the Knight shift decreases, where the linewidth steeply increases (Fig. 8.4). The linewidth at 1.5 K is approximately three times larger than that at 20 K for peak II. The linewidth which has the larger hyperfine coupling constant becomes broader at the lowest temperature. This result suggests that the line broadening comes from the inhomogeneity of the spin susceptibility. The present result of line broadening is consistent with that for ^{77}Se NMR. Moreover, we found that with decrease in temperature, the line broadening is evident below 20 K, at which Knight shift starts to decrease. To quantitatively discuss the distribution of spin susceptibility, we investigated the angle dependence of Knight

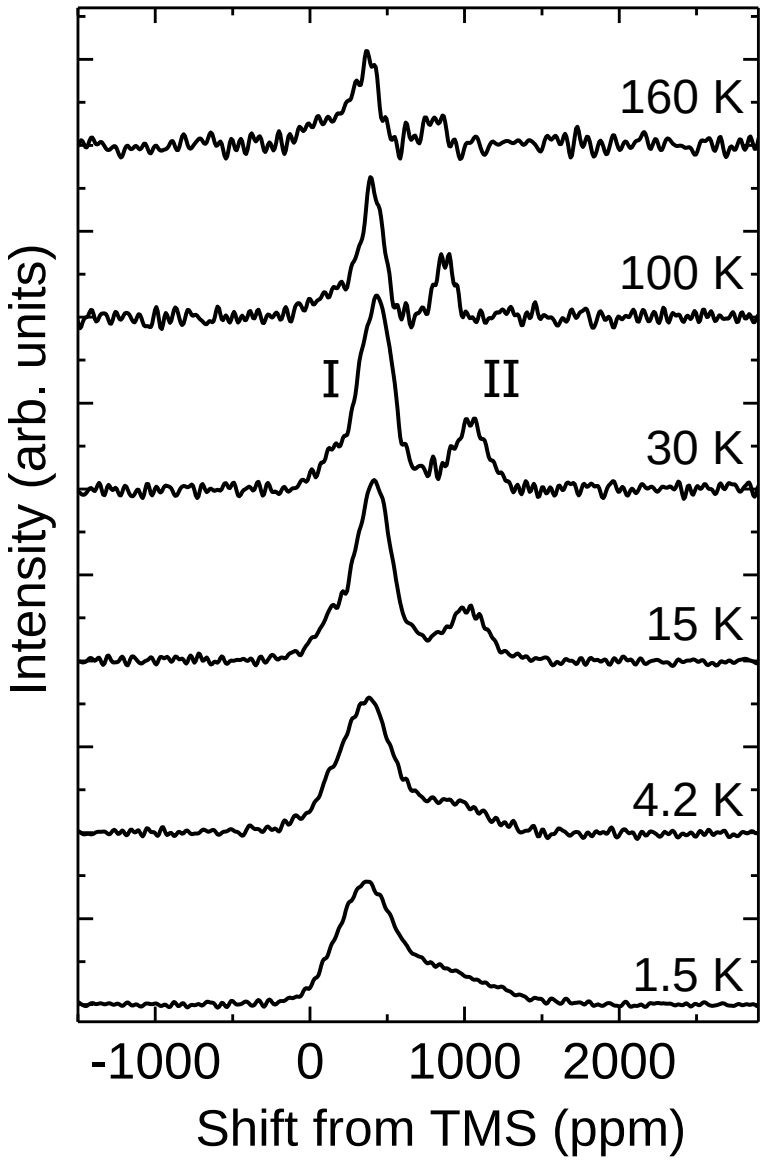

Figure 8.1: (a)Temperature dependence of NMR spectra.

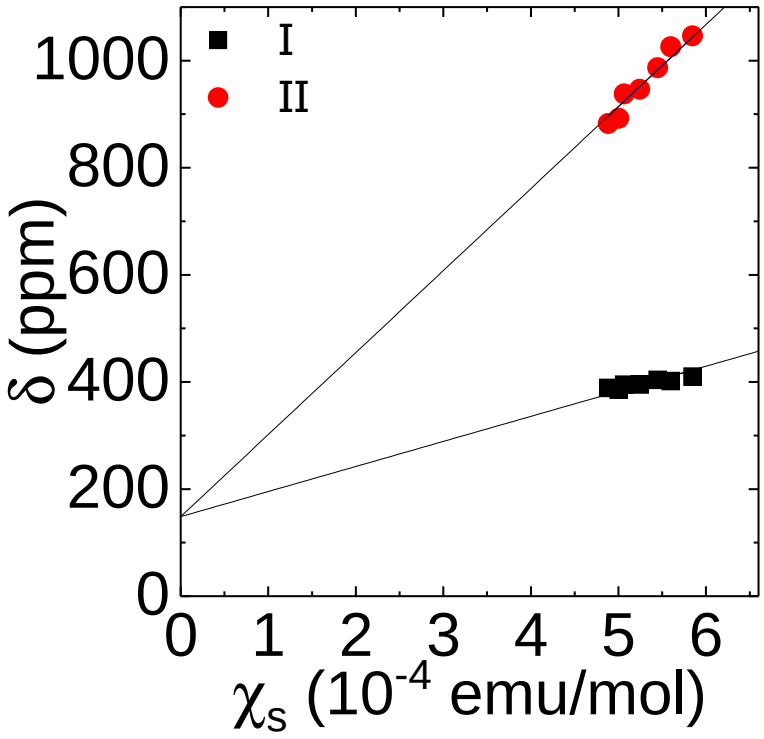

Figure 8.2: $\delta - \chi$ plot between 30 K and 100 K. The data of susceptibility are cited from Ref.[65]

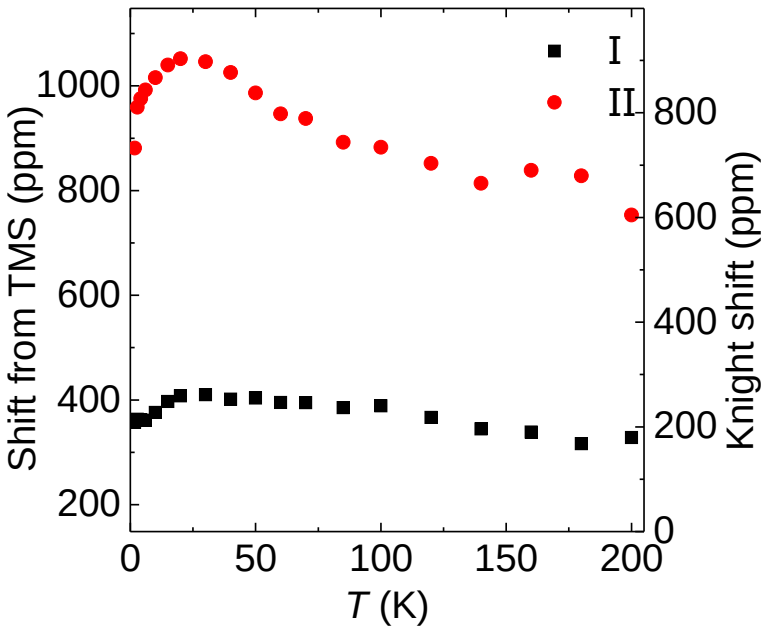

Figure 8.3: Temperature dependence of the NMR shift (left scale). The Knight shift is shown in the right scale.

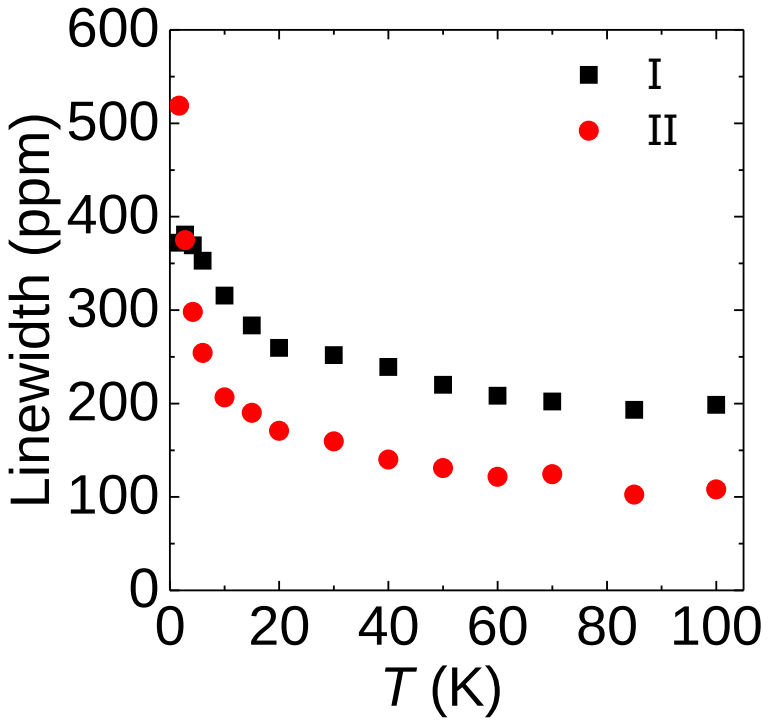

Figure 8.4: Temperature dependence of linewidth.

shift and linewidth in 8.1.2. The behavior of Knight shift and linewidth can be explained due to the development of magnetic fluctuations below 20 K. This interpretation is compatible with the results of increase in $1/T_1T$ below 20 K as discussed in 8.1.3.

8.1.2 Angle dependence of NMR spectra

Field angle dependence of NMR spectra were measured at (a) 1.8 K and (b) 30 K as shown in Fig. 8.5. By rotating the sample, NMR spectra change from asymmetric single peak to double peak. Figure 8.6 shows the field orientation dependence of NMR shift (left scale, closed symbol) and linewidth (right scale, open symbol) obtained by fitting with two Lorentzians. NMR shift and linewidth vs field orientation curves can be fitted by the sine curve. From these fittings, we can estimate that NMR shift shows the maximum at θ=−18° and shows the minimum at θ=−108°. By considering the relation between crystal structure and field orientation, the maximum (minimum) of NMR shift was observed when the magnetic field is applied perpendicular (parallel) to the molecular plane. This result is consistent with the previous ^{77}Se NMR measurements [76]. Because the chemical shift is 149 ppm, main contribution of the angle dependence of the NMR shift is due to the Knight shift. Linewidth has also the same angle dependence as the Knight shift. These results suggest that the angle dependence of Knight shift $K(\theta)$ and linewidth

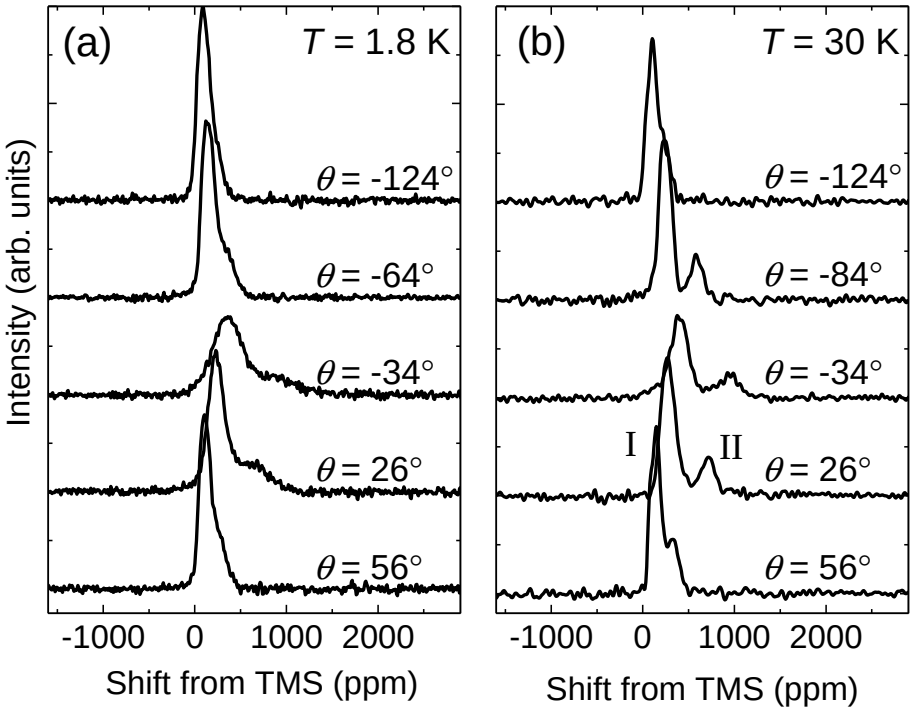

Figure 8.5: Field orientation dependence of NMR spectra at (a)1.8 K and (b)30 K.

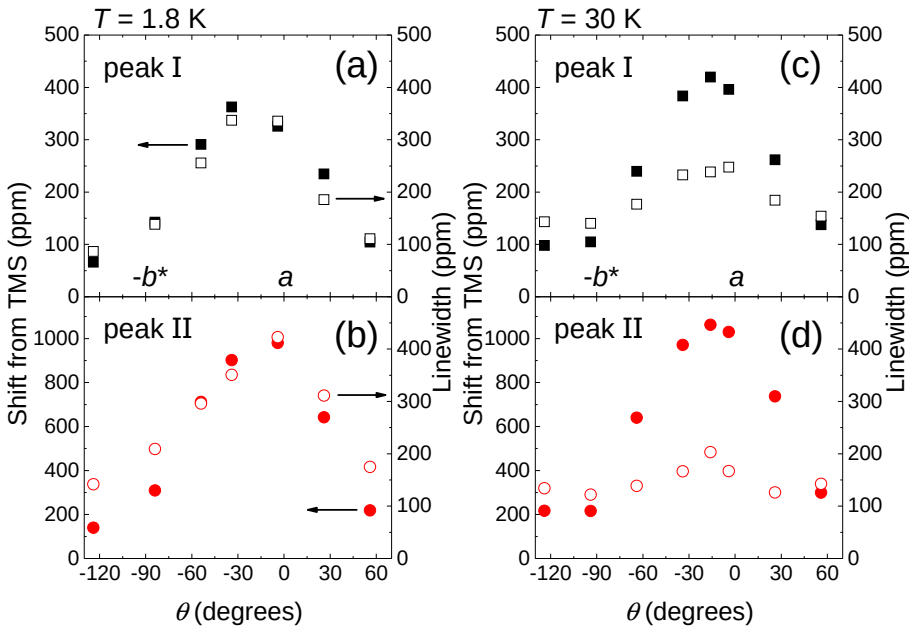

Figure 8.6: Angle dependences of NMR shift (left scale) and linewidth (right scale). The origin of the horizontal axis corresponds to the magnetic field applied parallel to the conduction plane.

$\omega(\theta)$ can be written as, $K(\theta) = A(\theta)\chi$ and $\omega(\theta) = A(\theta)\Delta\chi$. Here, $A(\theta)$, χ and $\Delta\chi$ are the hyperfine coupling constant, the spin susceptibility and the distribution of the spin susceptibility. To evaluate the degree of electronic inhomogeneity, we discuss the relative distribution of the spin density, $\Delta\chi/\chi = \omega(\theta)/K(\theta)$. These values of each peak are displayed in Table 8.1.

Table 8.1: Relative distribution of the spin density $\Delta\chi/\chi$.

	1.8 K	30 K
peak I	0.91	0.33
peak II	0.29	0.061

$\Delta\chi/\chi$ for peak I is larger than that for peak II. This is consistent with the interpretation that the peak I is composed of three ^{13}C sites. Increasing ratios of peak I and II from 30 K to 1.8 K are 2.7 and 4.9, which are correlated to the hyperfine coupling constant. This result suggests that the increase in the linewidth with decreasing temperature is due to the inhomogeneity of local spin susceptibility. We compare the results of ^{13}C NMR with ^{77}Se NMR measurements. The value $\Delta\chi/\chi = 0.29$ of peak II ($T = 1.8$ K) is almost comparable with the value $\Delta\chi/\chi = 0.3$ ($T = 1.9$ K) obtained from ^{77}Se NMR experiment [76]. Note that the value of peak I cannot be compared quantitatively due to the superposition of three ^{13}C sites. Therefore, we suggest that the degree of inhomogeneity of local spin susceptibility is essential for λ-$(BETS)_2GaCl_4$ salt.

8.1.3 Spin-lattice relaxation time T_1

Magnetic fluctuation at high temperature

In order to study the magnetic fluctuation, we measured T_1. Figure 8.7 shows the temperature dependence of $1/T_1T$ at $\theta = 56°$. $1/T_1T$ increases with decreasing temperature down to $T^* = 55$ K. When the system has two-dimensional antiferromagnetic spin fluctuations, general formula of eq. 2.3 can be rewritten as Curie-Weiss expression, $1/T_1T = C/(T + \Theta)$ [82]. Here C and Θ are the Curie constant and Weiss temperature. This expression is represented as the solid line in Fig. 8.7 with values $C = (11.6 \pm 0.4)$ s^{-1}, $\Theta = (31.5 \pm 4.2)$ K for $\theta = 56°$. The temperature dependence of $1/T_1T$ above T^* is reproduced well by Curie-Weiss expression, which suggests the existence of an antiferromagnetic fluctuation in λ-$(BETS)_2GaCl_4$ salt. Similar behavior was observed in κ-Br salt. $1/T_1T$ for κ-Br salt shows Curie-Weiss behavior above 50 K [12]. This temperature dependence of $1/T_1T$ follows that for κ-Cl salt which is an antiferromagnetically ordered Mott insulator. This behavior suggests that the existence of antiferromagnetic fluctuation

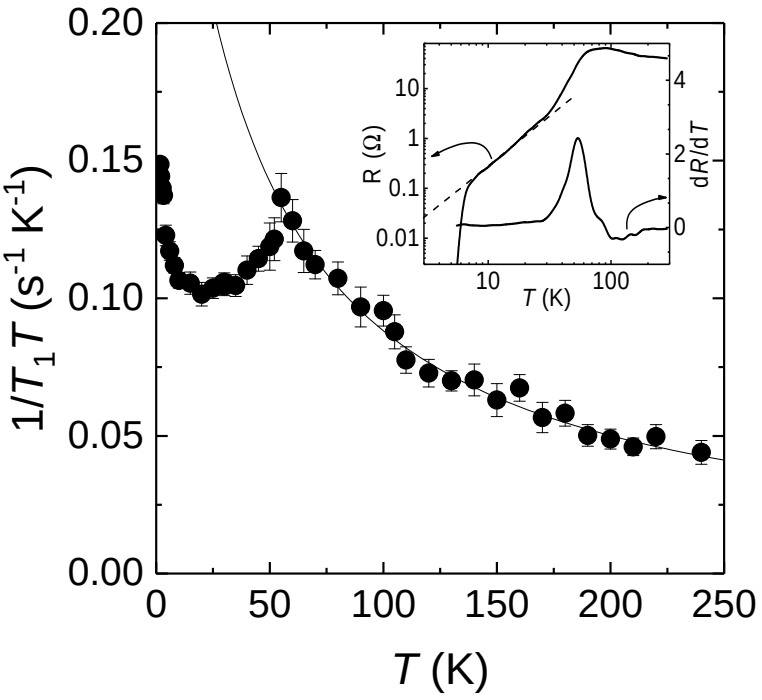

Figure 8.7: Temperature dependence of $1/T_1T$ at $\theta = 56°$. Inset shows the temperature dependence of the resistivity (left scale) and the temperature derivative of the resistivity (right scale).

in κ-Br salt originates from the antiferromagnetic Mott insulating phase. As mentioned above, the electronic phase of λ-D_2GaCl_4 salts can be understood using the P–T phase diagram in Fig. 6.9, which suggests that the antiferromagnetic fluctuation of λ-$(BETS)_2GaCl_4$ salt is derived from the neighboring antiferromagnetic phase.

One candidate for the antiferromagnetic phase is the dimer-Mott insulator. Indeed, the intermolecular overlap integral in the dimer for the λ-$(BETS)_2GaCl_4$ salt is similar to that for the κ-type salt with the interplanar distances of ~ 3.69 Å for the λ-$(BETS)_2GaCl_4$ salt and ~ 3.56 Å for the κ-Br salt [65, 83]. The tight-binding band structure calculation for the λ-$(BETS)_2GaCl_4$ salt also shows this characteristic feature of a dimer–Mott system as shown in Fig. 6.2 [63, 65]. Therefore, the superconducting phase of λ-modification can be adjacent to the antiferromagnetic dimer-Mott insulating phase.

At T^*, $1/T_1T$ shows a peak, below which $1/T_1T$ decreases. T^* corresponds to the temperature where the resistivity shows the inflection, as shown in the inset of Fig. 8.7 [68]. This result suggests that below T^*, which characterizes the crossover from semiconductor to metal, the development of itinerancy suppresses the antiferromagnetic fluctuation. At around 30 K, $1/T_1T$ becomes temperature independent and the resistivity shows T^2 behavior. These are hallmarks of a Fermi liquid state. The same relation between conductivity and antiferromagnetic fluctuation

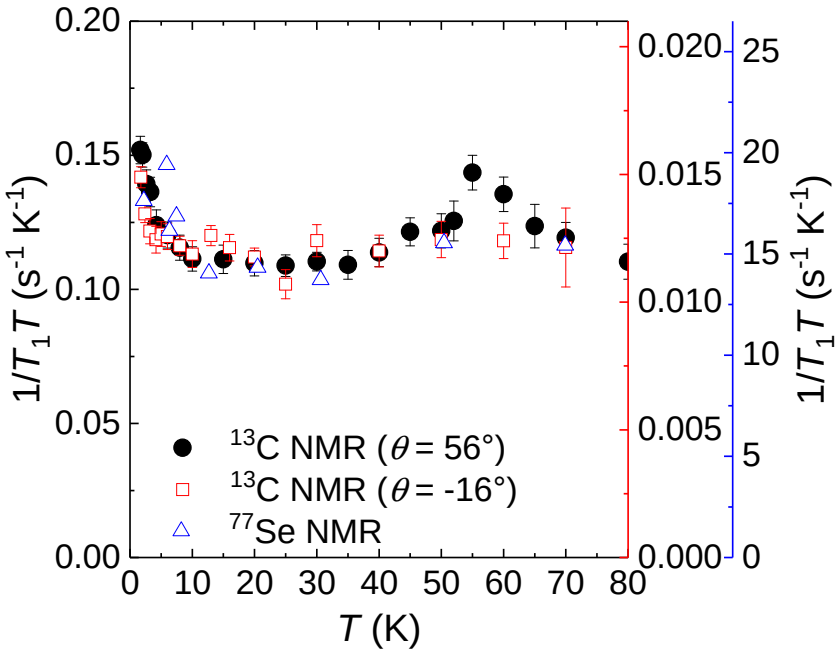

Figure 8.8: Temperature dependence of $1/T_1T$ for ^{13}C and ^{77}Se NMR [76]. The left scale and the left side of the right scale corresponds to the ^{13}C NMR at $\theta = 56°$ and $\theta = -16°$, respectively. The right side of the left scale corresponds th the ^{77}Se NMR.

has been discussed in κ-Br salt [47, 48].

Here, we discuss the difference between κ-Br and λ-$(BETS)_2GaCl_4$ salts. In κ-Br salt, the temperature dependence of $1/T_1T$ above T^* is expressed as the sum of the $(1/T_1T)_{AF}$ term and $(1/T_1T)_{FL}$ term (eq. 3.2), which indicates that there is a relaxation process due to the band structure at high temperatures. In addition, since the absolute value of $1/T_1T$ in the Fermi liquid state is comparable to that at high temperature, we considered that the $(1/T_1T)_{AF}$ term is almost suppressed in the Fermi liquid state. On the other hand, the temperature dependence of $1/T_1T$ above T^* is explained only the $(1/T_1T)_{AF}$ term, so that all carriers at the Fermi energy contribute to the antiferromagnetic fluctuation. As a result, in the Fermi liquid state antiferromagnetic electronic correlation is renormalized into the effective quasiparticle mass. These results imply that the electronic correlation of λ-$(BETS)_2GaCl_4$ salt is stronger than that of κ-type salt.

Magnetic fluctuation at low temperature

Below 10 K, we found that $1/T_1T$ increases again in accordance with the Curie-Weiss behavior. Figure. 8.8 shows the temperature dependence of $1/T_1T$ at $\theta = 56°$ (closed circles) and $-16°$ (open rectangles) below 70 K. Simultaneously, the result of $1/T_1T$ for ^{77}Se NMR are plotted (open triangles) [76]. From the result of $1/T_1T$ at $\theta = 56°$, C and Θ can be roughly estimated as $(0.12 \pm$

0.03) s^{-1}, $\Theta = (0.69 \pm 0.50)$ K, indicating that the origin of increase in $1/T_1T$ at low temperatures is different from the antiferromagnetic fluctuation above T^*. This anomalous enhancement was confirmed from the temperature dependence of $1/T_1T$ at $\theta = -16°$ and $1/T_1T$ for ^{77}Se NMR. These results suggested that increase in $1/T_1T$ at low temperatures is intrinsic and independent of field directions. A possible explanation of increase in $1/T_1T$ is the magnetic fluctuation enhanced by the nesting effect of the Fermi surface. In fact, λ-$(BETS)_2GaCl_4$ salt has a one-dimensional sheets in the Fermi surface [63, 84]. A similar Curie-like behavior of $1/T_1T$ was observed in $(TMTSF)_2PF_6$ salt under pressures [85], at which the superconducting state emerges near the spin-density-wave (SDW) phase. Resistivity measurements at the same pressure regions show linear temperature dependence in the normal state, destroying the superconductivity by the weak magnetic field [86], which suggests the non-Fermi liquid state. These results indicate that the SDW fluctuation is realized in the non-Fermi liquid state. A similar situation can be expected in λ-$(BETS)_2GaCl_4$ salt while the conducting properties have not been studied in the normal state near T_c. The existence of SDW fluctuation can consistently explain the line broadening and decrease in the Knight shift. Interestingly, in the alloy of λ-$(BETS)_2GaBr_xCl_{4-x}$ salts, the salts of $x = 0.0$ to $x = 0.75$ showed the semiconductor–metal crossover behavior and a metal–insulator transition occurred at 18 K in $x = 0.75$ salt (Fig. 6.10), showing the anomaly observed in the magnetic susceptibility measurement (Fig. 6.11) [65]. This metal–insulator transition might be the SDW transition.

Since the antiferromagnetic fluctuation at high temperatures is suppressed below T^*, it seems not to be related with the superconducting state directly. The behaviors at around T^* are reminiscent of κ-type salts, whereas the magnetic fluctuation at low temperatures can be intimately related with the superconducting state, suggesting the different pairing mechanism from that of κ-type salts.

In this thesis, we explained the results below 20 K by the development of the magnetic fluctuation. However, ^{77}Se NMR measurement suggests that the line broadening at low temperatures originates from the charge disproportionation in the conducting layer [76], which is still the possible mechanism. Since NMR spectroscopy is sensitive not to charge but also spin, charge sensitive experiments such as infrared or Raman spectroscopies are needed to reveal the charge disproportionation.

The λ-$(BETS)_2FeCl_4$ salt exhibits an antiferromagnetic phase transition at zero magnetic field at 8.3 K, which has been thought to be derived from the interaction between Fe $3d$ spins [87]. Recently, specific-heat measurements indicate that the antiferromagnetism in the λ-$(BETS)_2FeCl_4$ salt is caused by the antiferromagnetic alignment of π spins, whereas the Fe $3d$ spins are in the paramagnetic spin state [88]. Although the origin of antiferromagnetic ordering has been exten-

sively studied, this aspect has not been settled as yet. The development of magnetic fluctuation below 10 K in the nonmagnetic λ-$(BETS)_2GaCl_4$ salt indicates that the interaction between π spins of BETS molecules is a source of antiferromagnetic ordering in λ-$(BETS)_2FeCl_4$ salt.

8.2 Superconducting state

8.2.1 Knight shift

In order to clarify the influence of the magnetic fluctuation existing in λ-$(BETS)_2GaCl_4$ salt on superconductivity, we performed the ^{13}C NMR measurement in the superconducting state. For this purpose, magnetic field is applied parallel to the conduction plane, in which the upper critical field becomes the largest as 10 T. Figure 8.9 shows the NMR spectra at 6.5 T at several temperatures. Two NMR peaks were observed and the NMR shift decreases with decreasing temperature. Temperature dependence of NMR shift at 2.5 T and 6.5 T are plotted in Fig. 8.10. NMR shift suddenly decreases below T_c and the temperature of decrease in NMR shift is slightly different between 2.5 T and 6.5 T depending on the T_c. For more quantitative discussion, we performed δ^{I}-δ^{II} plot at 6.5 T below T_c, in which δ largely changes due to the superconducting transition (Fig. 8.11). Because each peak can be expressed as $\delta^i = A^i\chi + \sigma$, the relation between δ^{I} and δ^{II} as follows,

$$\delta^{\mathrm{II}} = \frac{A^{\mathrm{II}}}{A^{\mathrm{I}}}\delta^{\mathrm{I}} + \left(1 - \frac{A^{\mathrm{II}}}{A^{\mathrm{I}}}\right)\sigma. \tag{8.1}$$

As a result, we obtained $A^{\mathrm{II}}/A^{\mathrm{I}} = 4.27$ and $\sigma = 200$ ppm. The temperature dependence of Knight shift is plotted in the right scale of Fig. 8.10. These results suggested that Knight shift decreases towards zero with decreasing temperature. We concluded the spin-singlet Cooper pair in the superconducting state of λ-$(BETS)_2GaCl_4$ salt.

8.2.2 Spin-lattice relaxation rate $1/T_1$

Next we discuss the superconducting gap symmetry from $1/T_1$ measurement, which provides the information about the k-space. Figure 8.12 shows the temperature dependence of $1/T_1$ at 2.5 T and 6.5 T. $1/T_1$ decreases below T_c and coherence peak was not observed. Absolute value of $1/T_1$ at 6.5 T is larger than that at 2.5 T below T_c due to the difference of T_c. The temperature dependence can be well explained by the calculation assuming the two-dimensional d-wave superconducting gap with $2\Delta = 4k_BT_c$. This value is consistent with that obtained by the thermodynamic study [66]. These results indicate that the symmetry of superconducting gap is d-wave.

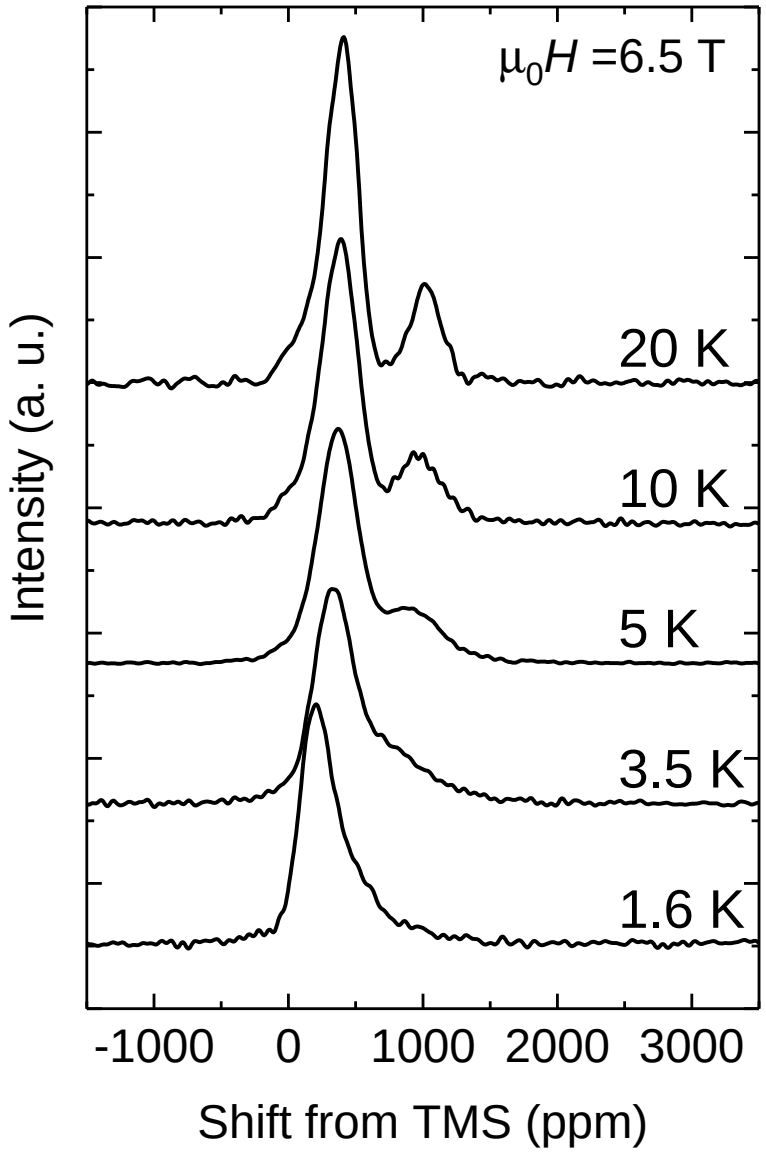

Figure 8.9: Temperature dependence of NMR spectra under the magnetic field applied parallel to the conduction plane.

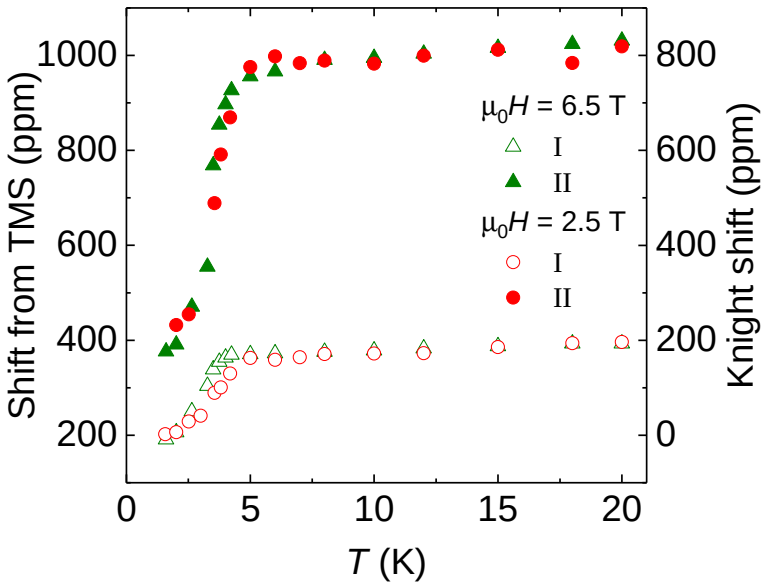

Figure 8.10: Temperature dependence of NMR shift.

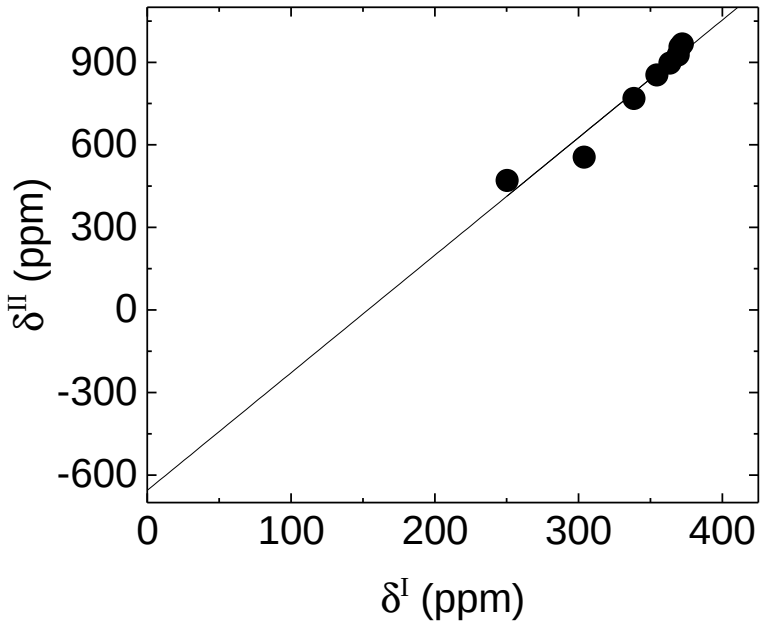

Figure 8.11: δ^{I} vs δ^{II} plot below T_c.

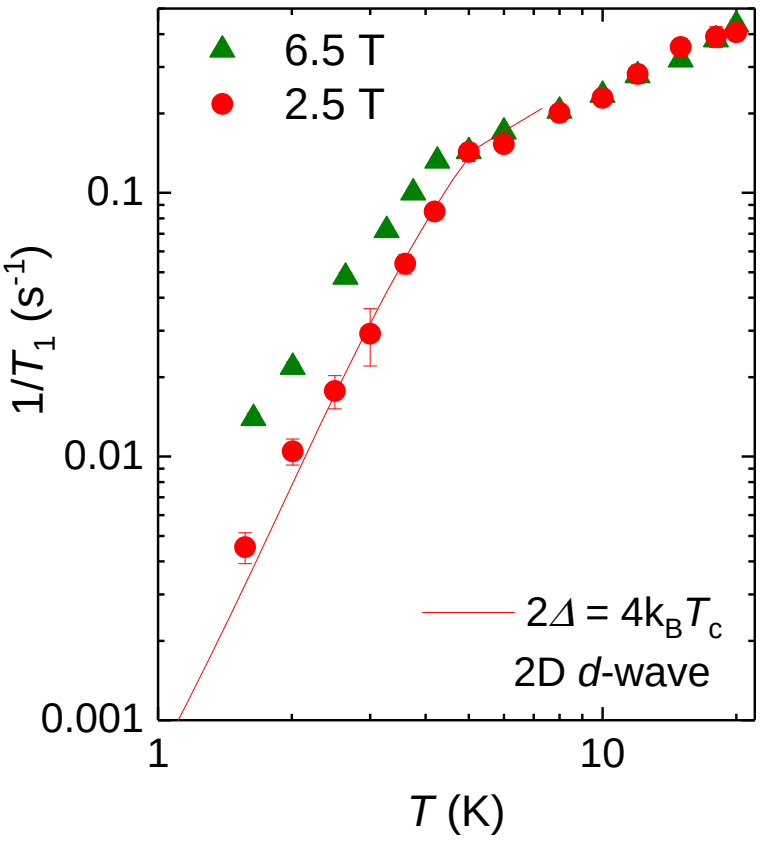

Figure 8.12: Temperature dependence of $1/T_1$ at 6.5 T (green triangles) and 2.5 T (red circles). Solid line shows the calculation result assuming the two-dimensional d-wave superconducting gap with $2\Delta = 4k_BT_c$.

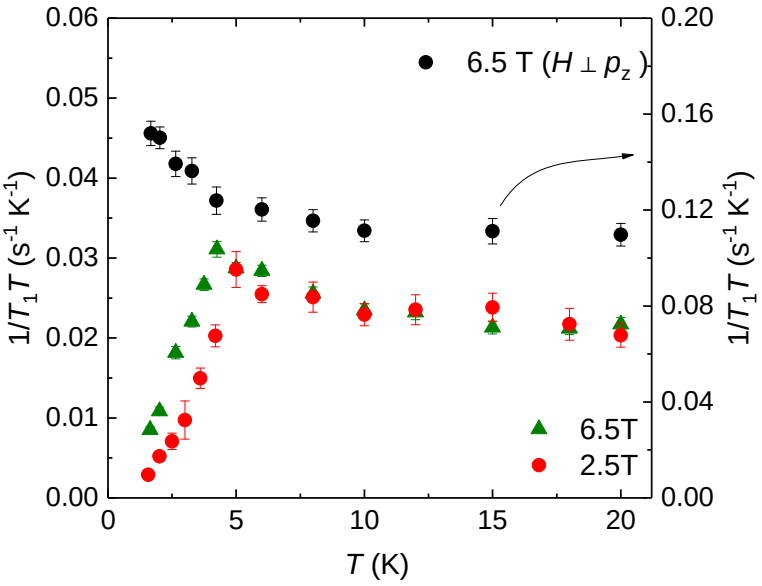

Figure 8.13: Temperature dependence of $1/T_1T$

Finally we discuss the relation between the magnetic fluctuation and the superconductivity. Figure 8.13 shows the temperature dependence of $1/T_1T$ at $\theta = 0°$ ($\mu_0 H \parallel$ conduction plane) with left scale and at $\theta = 56°$ with right scale. Although $1/T_1T$ increases down to 1.5 K when the superconductivity is suppressed, in the superconducting state, enhancement of $1/T_1T$ remains above T_c. This result suggests that superconductivity is realized with the magnetic fluctuation.

8.3 Summary

We prepared the ^{13}C enriched BETS molecules and performed the ^{13}C NMR measurement in λ-(BETS)$_2$GaCl$_4$ salt to examine the electronic properties in the paramagnetic state. The superconducting λ-(BETS)$_2$GaCl$_4$ salt possesses the different types of the magnetic fluctuations. Above 55 K, $1/T_1T$ shows Curie-like behavior, indicating the existence of an antiferromagnetic fluctuation originates from the dimer–Mott insulator. The peak behavior of $1/T_1T$ was observed at 55 K, where the semiconductor–metal crossover was observed in the electric conductivity, and shows the Fermi liquid like behavior at around 30 K. In addition, we also observed the increase in $1/T_1T$ below 10 K, and decrease in Knight shift and line broadening below 20 K, which can be related with the superconducting state. The anomaly at low temperatures can be understood by the development of the magnetic fluctuation due to the Fermi-surface nesting.

In the superconducting state, we revealed that Knight shift decreases towards zero as $T \to 0$, suggesting the spin-singlet state. $1/T_1$ shows no coherence peak and T^3 dependence far below T_c,

which indicates the existence of line nodes in the gap parameter on the Fermi surface. Moreover, temperature dependence of $1/T_1$ is reproduced well by the two-dimensional d-wave superconducting gap with $2\Delta = 4k_BT_c$. These results suggest that the symmetry of superconducting gap is d-wave. We also revealed that superconductivity is realized under the remaining of magnetic fluctuation just above T_c.

Chapter 9

Acknowledgments

I would like to express my gratitude to Professor Atushi Kawamoto and Professor Yoshihiko Ihara for their guidances and many advices. I would like to acknowledge Professor Kazushige Nomura, Professor Koji Nemoto, Professor Hiroshi Amitsuka, and Professor Koichi Ichimura in the review process of my doctoral thesis. I would like to appreciate Professor Ryusuke Ikeda from Kyoto University, Professor Takafumi Kita, Professor Carlos J. Gómez-García from the University of Valencia for fruitful discussions on the study of superconductivity in κ-(BEDT-TTF)$_2$Cu[N(CN)$_2$]Br salt. I would like to express my gratitude to Dr. Shuhei Fukuoka for many discussions on the study of λ-(BETS)$_2$GaCl$_4$ salt. I also would like to thank Dr. Yuki Oka for preparing BETS molecules.

I would like to thank Ms. Miko Matsumoto, Mr. Yohei Saito, Mr. Akihiro Ohnuma, and Mr. Hiroya Kumagai for supporting my experiments. I also want to thank Mr. Akio Suzuta, Mr. Kohei Tsuji, and Ms. Takako Ishikawa for conducting the constructive research of my doctoral thesis. I am deeply grateful for the assistance given by Mr. Yosuke Futami. Without his help, this thesis would not have materialized. I acknowledge other members of the Low Temperature Physics Group. Senior members of Dr. Hirose Shinji, Mr. Sanato Nagata, Ms. Harumi Seki, Mr. Kazuki Noda, and Mr. Tomoyuki Isome give me constructive comments and warm encouragement. Junior members of Mr. Takumi Waragai, Mr. Miharu Uchiyama, Mr. Motohiro Ozutsumi, Mr. Kazuto Moribe, Mr. Masashi Sawada, Mr. Koki Arashima, Mr. Daisuke Saegusa support my research activities.

I would like to thank the Ushio Foundation for financial support. These studies were partially supported by Japan Society for the Promotion of Science KAKENHI Grants No. 25610082, No. 16J06398, and No. 16K05427.

Finally, I would like to thank my family for their supports and encouragement.

Bibliography

[1] J. Bardeen, L. N. Cooper, and J. R. Schrieffer, Physical Review **108**, 1175 (1957).

[2] M. B. Maple, E. D. Bauer, V. S. Zapf, and J. Wosnitza, Unconventional superconductivity in novel materials, in *Superconductivity*, edited by K. H. Bennemann and J. B. Ketterson, pp. 639–762, Springer Berlin Heidelberg, 2008.

[3] D. Jérome, A. Mazaud, M. Ribault, and K. Bechgaard, Journal de Physique Lettres **41**, 95 (1980).

[4] D. Jérome, Science **252**, 1509 (1991).

[5] H. Urayama *et al.*, Chemistry Letters **17**, 55 (1988).

[6] J. M. Williams *et al.*, Inorganic Chemistry **29**, 3272 (1990).

[7] A. M. Kini *et al.*, Inorganic Chemistry **29**, 2555 (1990).

[8] H. Taniguchi *et al.*, Journal of the Physical Society of Japan **72**, 468 (2003).

[9] H. Mori, Journal of the Physical Society of Japan **75**, 051003 (2006).

[10] T. Moriya, Journal of the Physical Society of Japan **18**, 516 (1963).

[11] M. Itaya, Y. Eto, A. Kawamoto, and H. Taniguchi, Physical Review Letters **102**, 227003 (2009).

[12] A. Kawamoto, K. Miyagawa, Y. Nakazawa, and K. Kanoda, Physical Review B **52**, 15522 (1995).

[13] H. Mayaffre, P. Wzietek, D. Jérome, C. Lenoir, and P. Batail, Physical Review Letters **75**, 4122 (1995).

[14] G. Saito *et al.*, Synthetic Metals **42**, 1993 (1991).

[15] A. Narlikar, *Studies of high temperature superconductors : advances in research and applications* (Nova Science Publishers, 1989).

[16] Y. Masuda and A. G. Redfield, Physical Review **125**, 159 (1962).

[17] U. Geiser *et al.*, Physica C: Superconductivity **174**, 475 (1991).

[18] K. Kanoda, Physica C: Superconductivity **282-287**, 299 (1997).

[19] K. Kanoda, Hyperfine Interactions **104**, 235 (1997).

[20] S. Lefebvre *et al.*, Physical Review Letters **85**, 5420 (2000).

[21] F. Kagawa, T. Itou, K. Miyagawa, and K. Kanoda, Physical Review B **69**, 064511 (2004).

[22] M. Matsumoto, Y. Saito, and A. Kawamoto, Physical Review B **90**, 115126 (2014).

[23] T. Sasaki, N. Yoneyama, A. Matsuyama, and N. Kobayashi, Physical Review B **65**, 060505 (2002).

[24] W. Kwok *et al.*, Physical Review B **42**, 8686 (1990).

[25] M. Dressel *et al.*, Physical Review B **50**, 13603 (1994).

[26] T. Arai *et al.*, Physical Review B **63**, 1045186 (2001).

[27] S. Belin, K. Behnia, and A. Deluzet, Physical Review Letters **81**, 4728 (1998).

[28] H. Elsinger *et al.*, Physical Review Letters **84**, 6098 (2000).

[29] A. Balatsky, I. Vekhter, and J.-X. Zhu, Reviews of Modern Physics **78**, 373 (2006).

[30] T. Masui, N. Suemitsu, Y. Mikasa, S. Lee, and S. Tajima, Journal of the Physical Society of Japan **77**, 074720 (2008).

[31] Y. Kitaoka, K. Ishida, and K. Asayama, Journal of the Physical Society of Japan **63**, 2052 (1994).

[32] T. Sasaki, H. Oizumi, Y. Honda, N. Yoneyama, and N. Kobayashi, Journal of the Physical Society of Japan **80**, 104703 (2011).

[33] J. G. Analytis *et al.*, Physical Review Letters **96**, 177002 (2006).

[34] T. Naito, A. Miyamoto, H. Kobayashi, R. Kato, and A. Kobayashi, Chemistry Letters **21**, 119 (1992).

[35] T. Naito, K. Bun, A. Miyamoto, and H. Kobayashi, Synthetic metals **56**, 2234 (1993).

[36] H. Mayaffre, P. Wzietek, C. Lenoir, D. Jérome, and P. Batail, Europhysics Letters (EPL) **28**, 205 (1994).

[37] M. Matsumoto *et al.*, Journal of the Physical Society of Japan **81**, 114709 (2012).

[38] H. Kotegawa *et al.*, Physical Review B **66**, 064516 (2002).

[39] K. Ishida *et al.*, Physica C: Superconductivity **179**, 29 (1991).

[40] K. Ishida *et al.*, Journal of the Physical Society of Japan **62**, 2803 (1993).

[41] Z. Xu, N. Ong, Y. Wang, T. Kakeshita, and S. Uchida, Nature **406**, 486 (2000).

[42] H.-C. C. Ri *et al.*, Physical Review B **50**, 3312 (1994).

[43] V. F. Mitrović *et al.*, Physical Review Letters **82**, 2784 (1999).

[44] P. Carretta, A. Lascialfari, A. Rigamonti, A. Rosso, and A. Varlamov, Physical Review B **61**, 12420 (2000).

[45] A. I. Larkin and A. A. Varlamov, Fluctuation Phenomena in Superconductors, in *Superconductivity*, edited by K. H. Bennemann and J. B. Ketterson, pp. 369–458, Springer Berlin Heidelberg, 2008, arXiv:0109177.

[46] M.-S. Nam, A. Ardavan, S. J. Blundell, and J. A. Schlueter, Nature **449**, 584 (2007).

[47] A. Kawamoto, K. Miyagawa, Y. Nakazawa, and K. Kanoda, Physical Review Letters **74**, 3455 (1995).

[48] C. Strack *et al.*, Physical Review B **72**, 054511 (2005).

[49] S. Tsuchiya *et al.*, Physical Review B **85**, 220506 (2012).

[50] S. Tsuchiya *et al.*, Journal of the Physical Society of Japan **82**, 064711 (2013).

[51] M. Lang, F. Steglich, N. Toyota, and T. Sasaki, Physical Review B **49**, 15227 (1994).

[52] T. Uehara, M. Ito, H. Taniguchi, and K. Satoh, Journal of the Physical Society of Japan **82**, 073706 (2013).

[53] M. Randeria and A. Varlamov, Physical Review B **50**, 10401 (1994).

[54] K. Kuboki and H. Fukuyama, Journal of the Physical Society of Japan **58**, 376 (1989).

[55] M. Yamashita, A. Kawamoto, and K. Kumagai, Synthetic Metals **133-134**, 125 (2003).

[56] G. E. Pake, The Journal of Chemical Physics **16**, 327 (1948).

[57] A. Kawamoto, H. Taniguchi, and K. Kanoda, Journal of the American Chemical Society **120**, 10984 (1998).

[58] S. De Soto *et al.*, Physical Review B **52**, 10364 (1995).

[59] K. Sano, T. Sasaki, N. Yoneyama, and N. Kobayashi, Physical Review Letters **104**, 217003 (2010).

[60] N. B. Kopnin, , The international series of monographs on physics Vol. 110 (Clarendon Press, Oxford, 2001).

[61] A. Abrikosov and L. Gor'kov, Sov. Phys. JETP **12**, 1243 (1961).

[62] K. Miyagawa, A. Kawamoto, and K. Kanoda, Physical Review Letters **89**, 017003 (2002).

[63] L. Montgomery, T. Burgin, J. Huffman, J. Ren, and M.-H. Whangbo, Physica C: Superconductivity **219**, 490 (1994).

[64] M. A. Tanatar, T. Ishiguro, H. Tanaka, and H. Kobayashi, Physical Review B **66**, 134503 (2002).

[65] H. Tanaka, A. Kobayashi, A. Sato, H. Akutsu, and H. Kobayashi, Journal of the American Chemical Society **121**, 760 (1999).

[66] S. Imajo *et al.*, Journal of the Physical Society of Japan **85**, 043705 (2016).

[67] W. A. Coniglio *et al.*, Physical Review B **83**, 224507 (2011).

[68] S. Uji *et al.*, Journal of the Physical Society of Japan **84**, 104709 (2015).

[69] T. Suzuki, E. Negishi, H. Uozaki, H. Matsui, and N. Toyota, Physica C **440**, 17 (2006).

[70] K. Clark *et al.*, Nature nanotechnology **5**, 261 (2010).

[71] D. P. Sari *et al.*, IOP Conference Series: Materials Science and Engineering **196**, 012047 (2017).

[72] H. Mori *et al.*, Physica C **357-360**, 103 (2001).

[73] T. Minamidate *et al.*, Journal of the Physical Society of Japan **84**, 063704 (2015).

[74] Y. Saito, S. Fukuoka, T. Kobayashi, A. Kawamoto, and H. Mori, Journal of the Physical Society of Japan **87**, 013707 (2018).

[75] Y. Saito *et al.*, To be submitted.

[76] K. Hiraki *et al.*, Journal of the Physical Society of Japan **79**, 074711 (2010).

[77] S. Takagi *et al.*, Journal of the Physical Society of Japan **72**, 483 (2003).

[78] S. Hirose, M. Misawa, and A. Kawamoto, Crystals **2**, 1034 (2012).

[79] T. Courcet, I. Malfant, K. Pokhodnia, and P. Cassoux, New Journal of Chemistry **22**, 585 (1998).

[80] H. Kobayashi *et al.*, Chemistry Letters **22**, 1559 (1993).

[81] T. Kawai and A. Kawamoto, Journal of the Physical Society of Japan **78**, 074711 (2009).

[82] T. Moriya and K. Ueda, Reports on Progress in Physics **66**, 1299 (2003).

[83] T. Mori, H. Mori, and S. Tanaka, Bulletin of the Chemical Society of Japan **72**, 179 (1999).

[84] C. Mielke *et al.*, Journal of Physics: Condensed Matter **13**, 8325 (2001).

[85] Y. Kimura, M. Misawa, and A. Kawamoto, Physical Review B **84**, 045123 (2011).

[86] N. Doiron-Leyraud *et al.*, Physical Review B **80**, 214531 (2009).

[87] H. Kobayashi *et al.*, Journal of the American Chemical Society **118**, 368 (1996).

[88] H. Akiba *et al.*, Journal of the Physical Society of Japan **78**, 033601 (2009).